



# DEPARTMENT OF PHYSICS

UNIVERSITY OF CAPE TOWN

IYUNIVESITHI YASEKAPA • UNIVERSITEIT VAN KAAPSTAD

Search for  $tWZ$  production in the Full Run 2 ATLAS  
dataset using events with four leptons

Jake Reich

Student Number: RCHJAK001

Supervisor: Dr. James Keaveney

Co-Supervisor: Dr. Sahal Yacoob

August 2021

# **Abstract**

# Declaration

*I certify that this assignment/report is my own work, based on my personal study and/or research and that I have acknowledged all material and sources used in its preparation, whether they be books, articles, reports, lecture notes, and any other kind of document, electronic or personal communication. I also certify that this assignment/report has not previously been submitted for assessment in any other unit, except where specific permission has been granted from all unit coordinators involved, or at any other time in this unit, and that I have not copied in part or whole or otherwise plagiarised the work of other students and/or persons.*

# Acknowledgements

# Contents

<b>1</b>	<b>Introduction</b>	<b>7</b>
<b>2</b>	<b>Theory</b>	<b>8</b>
2.1	Standard Model of Particle Physics . . . . .	8
2.1.1	The Top Quark . . . . .	9
2.2	$tWZ$ . . . . .	10
2.2.1	Tetralepton Channel . . . . .	10
2.2.2	Comparison to Trilepton Channel . . . . .	11
2.2.3	Motivation for the search for $tWZ$ production in the tetralepton channel . . . . .	12
<b>3</b>	<b>The ATLAS Experiment and Detector</b>	<b>13</b>
3.1	The ATLAS Experiment . . . . .	13
3.1.1	Large Hadron Collider (LHC) . . . . .	13
3.2	The ATLAS Detector . . . . .	14
3.2.1	Coordinate System and Kinematics . . . . .	14
3.2.2	Inner Detector . . . . .	15
3.2.3	Electromagnetic and Hadronic Calorimeters . . . . .	15
3.2.4	Muon Spectrometer . . . . .	15
3.2.5	Trigger and Data Acquisition System . . . . .	15
<b>4</b>	<b>Analysis Setup and Strategy</b>	<b>16</b>
4.1	Data and Monte Carlo Simulation . . . . .	16
4.1.1	Data Samples . . . . .	16
4.1.2	Monte Carlo Samples . . . . .	16
4.2	Objects . . . . .	17
4.2.1	Leptons . . . . .	18
4.2.2	Jets . . . . .	19
4.2.3	$b$ -tagging . . . . .	19
4.3	Kinematic cuts . . . . .	20
4.4	Regions and Event Selection . . . . .	20
4.4.1	Optimization studies for event selection . . . . .	21
4.5	Signal and Control Regions . . . . .	23
4.5.1	$tWZ$ OF SR . . . . .	24
4.5.2	$tWZ$ SF SR . . . . .	25
4.5.3	$t\bar{t}Z$ CR . . . . .	25
4.5.4	$ZZb$ CR . . . . .	26
4.5.5	$(tWZ)_{\text{fake}}$ CR . . . . .	38
4.6	Fake Lepton Estimation . . . . .	38
4.7	Machine Learning Techniques . . . . .	42
4.7.1	Object-level BDT . . . . .	44
4.7.2	Event-level BDT . . . . .	50
4.8	Two Neutrino Scanning Method ( $2\nu\text{SM}$ ) Algorithm . . . . .	55
4.8.1	The algorithm . . . . .	55
4.8.2	Calculating $w_{2\nu\text{SM}}$ . . . . .	56
4.8.3	Kinematic Veto . . . . .	57

---

4.9	Systematics . . . . .	60
4.9.1	Experimental uncertainties . . . . .	61
4.9.2	Theoretical uncertainties . . . . .	62
4.9.3	Generic shape systematics . . . . .	63
4.10	Analysis Pipeline and TRexFitter . . . . .	63
4.10.1	Fitting Procedure . . . . .	64
4.11	Results . . . . .	65
4.11.1	Tetralepton Channel . . . . .	65
4.11.2	Trilepton and Tetralepton Channels . . . . .	68
<b>5</b>	<b>Conclusion and Outlook</b>	<b>73</b>
<b>A</b>	<b>Appendix</b>	<b>74</b>
A.1	Pre-Fit Plots . . . . .	74
A.1.1	$tWZ$ OF SR . . . . .	74
A.1.2	$tWZ$ SF SR . . . . .	81
A.1.3	$t\bar{t}Z$ CR . . . . .	88
A.1.4	$ZZb$ CR . . . . .	95
A.1.5	$(tWZ)_{\text{fake}}$ CR . . . . .	103

# Chapter 1

## Introduction

The production of a single top quark in association with a  $W^\pm$  and  $Z$  boson ( $tW^\pm Z$ ) at the CERN LHC is sensitive to both the neutral and charged electroweak couplings of the top quark as the process involves the simultaneous production of a  $W$  boson and a  $Z$  boson in association with the top quark. Due to the very large coupling of the top quark to the Higgs boson, the electroweak couplings of the top quark are a theoretically well-motivated area in which to search for the first signs of new physics. The recent lack of signs of new physics from LHC data tells us that new physics is either very heavy, or is very weakly coupled to Standard Model particles, therefore we might only observe signs of new physics in anomalous rates of well-chosen processes. A prime example of such a process is  $tWZ$ . This has an extremely low production cross section (0.7 fb for  $\sqrt{s} = 13$  TeV [19]), meaning that it is an extremely rare process to observe and subsequently, it has never been observed by any particle physics experiment. However, the latest datasets recorded by the ATLAS experiment at the CERN LHC are sufficiently large to allow a potential observation of this rare process. We use the Full Run 2 dataset recorded by the ATLAS to search for the production of a top quark together with a  $W^\pm$  and  $Z$  boson in the channel with four leptons (two originating from the decay of the  $Z$  boson, one from the associated  $W$  boson and one from the  $W$  boson which decays from the top quark (together with a  $b$  quark)). In this analysis, we use a kinematic reconstruction technique which aims to discriminate between  $tWZ$  and our most prominent background process,  $t\bar{t}Z$ . In addition to this, we implement Machine Learning techniques (Boosted Decision Trees) to further isolate our  $tWZ$  signal. The dominant source of the fake lepton background is from  $t\bar{t}Z$  events containing at least one fake lepton. The kinematic distributions of this background are taken from simulation and its normalisation is constrained using a dedicated control region. As this work forms the basis of an official ATLAS analysis, only blinded results are shown. A maximum likelihood fit (blinded) is performed over our two  $tWZ$  signal regions and three control regions, measure the cross section of  $tWZ$  in the tetralepton channel. In order to increase the sensitivity of our  $tWZ$  signal, we perform another maximum likelihood fit (blinded) over all regions defined for the tetralepton channel and the trilepton channel<sup>1</sup>.

---

<sup>1</sup>an independent analysis conducted by Benjamin Warren (University of Cape Town) [56]

# Chapter 2

## Theory

### 2.1 Standard Model of Particle Physics

The Standard Model (SM) is a Quantum Field Theory (QFT) which classifies all known elementary particles and describes their interactions. It is a well-tested model and has shown to be hugely successful in describing experimental data to great precision. It incorporates three of the four fundamental forces of nature: the electromagnetic, the weak and the strong forces. In Figure 2.1, all known elementary particles described by the SM, are shown.

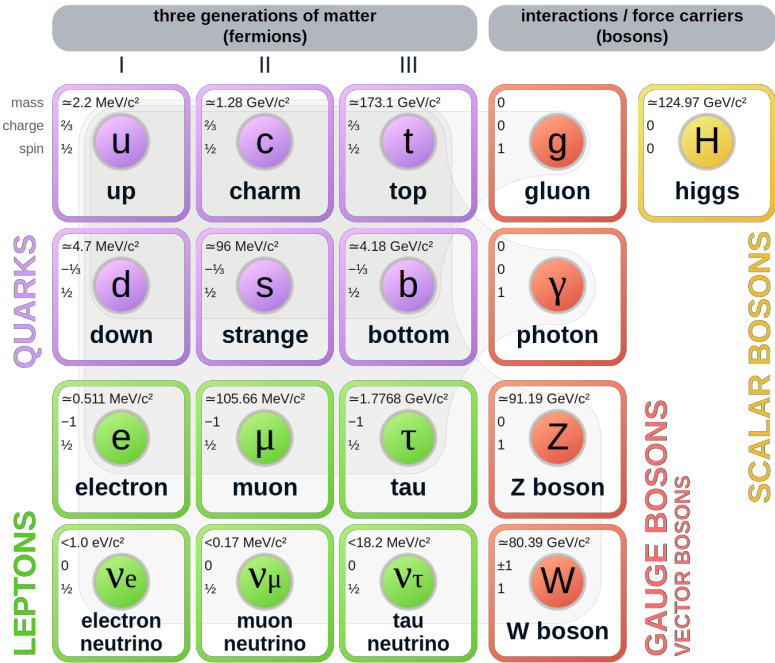


Figure 2.1: A summary of the elementary particles described by the SM [45] is shown. Fermions are shown on the left, with quarks shown in purple and leptons shown in green. Bosons are shown on the right, with gauge bosons shown in red and the Higgs boson shown in yellow. The mass, electric charge and spin of each particle is shown on the top left of each particle's block.

SM particles are uniquely described by their quantum numbers: mass, electric charge and spin. The SM particles are split into main two classes, based off their spin quantum numbers. Particles which have half-integer spin are called fermions, and those which have integer spin are called bosons. Fermions are further divided into three generations, each comprising of two quarks, one charged lepton and one neutrino. The particles of each generation have identical electric charge and spin, but their masses differ. The masses of the particles in a generation increase with increasing generation number, with generation 1 particles being the least massive and generation 3 particles being the most massive. Quarks carry electric and colour charge, and can therefore interact via the electromagnetic, weak

and strong forces. Colour charge can take on three values: red, green and blue. Due to colour confinement [57], quarks cannot be isolated from one another. They exist in colourless bound states, called hadrons, consisting of two or more quarks. Hadrons consisting of an even number of quarks are known as mesons and those consisting of an odd number of quarks are known as baryons. On the other hand, charged leptons (electron ( $e$ ), muon ( $\mu$ ) and tau ( $\tau$ )) only carry electric charge and can therefore interact electromagnetically and weakly, but not through the strong interaction. The electric and colour neutral fermions, neutrinos, can only interact via the weak force.

Particles are able to interact with one-another via the exchange of a gauge boson (boson with spin-1). Photons are massless, spin-1 gauge bosons which mediate electromagnetic interactions between particles which carry electric charge, such as quarks and charged leptons ( $e$ ,  $\mu$  and  $\tau$ ). The weak interaction is mediated by three massive gauge bosons, the electrically charged  $W^+$  and  $W^-$  bosons and the electrically neutral  $Z$  boson. Gluons are massless, spin-1 gauge bosons which mediate strong interactions between particles which carry colour charge, such as quarks. Since gluons carry colour charge, they interact with themselves.

The massive, spin-0, electrically neutral Higgs boson mediates the Higgs field which gives mass to the  $W^\pm$  and  $Z$  bosons via the so-called Brout-Englert-Higgs mechanism [29, 36, 35]. The Brout-Englert-Higgs mechanism induces spontaneous electroweak symmetry breaking to provide mass terms for the  $W^\pm$  and  $Z$  bosons in the electroweak Lagrangian of the SM.

All particles described in the SM have their own antiparticle, with the same mass, but opposite charges. Some particles, such as the photon, are their own antiparticle.

Although the SM has shown to be hugely successful, it is incomplete and fails to describe certain observed phenomena. The most notable example being the absence of gravity from the SM. The gravitational force is  $\approx 10^{24}$  weaker than the weak force, therefore quantum gravitational effects are expected to only become significant at energies much larger than that currently accessible by the LHC (known as the Planck scale  $\approx 10^9$  GeV) [39]. This large difference in strength between the weak force and gravity is known as the Hierarchy Problem. Cosmological observations infer that around 84% of the matter in the universe consists of gravitationally interacting matter known as dark matter. None of the particles described in the SM are good dark matter candidates, therefore the SM only accounts for a small fraction of the total matter of the universe. The large discrepancy between the observed amount of matter and antimatter in the universe, sometimes referred to as the matter-antimatter asymmetry, is unable to be fully explained by the SM. Neutrinos in the SM are assumed to be massless, however observations of neutrino oscillations (neutrinos undergoing flavour change as they travel through space) imply that neutrinos do have mass [31]. Beyond the Standard Model (BSM) theories attempt to explain the phenomena which the SM cannot. For example, a popular extension to the SM, Supersymmetry (SUSY) introduces new particles to the SM which are counterparts to the existing SM particles with the same quantum numbers, except for their spins. SUSY provides elegant explanations to many shortcomings of the SM, however none of the supersymmetric particles described by SUSY have been observed experimentally.

### 2.1.1 The Top Quark

The top quark is the heaviest particle in the SM, with a mass of  $172.76 \pm 0.30$  GeV [34]. Since the coupling to the Higgs boson is proportional to the mass of the interacting particle, the top quark is strongly coupled to the Higgs boson. Physics involving top quarks is therefore a theoretically well-motivated area to search for new physics, since it is the most likely particle to couple to new physics theories at the TeV scale. Its large mass also makes it highly unstable, with a mean lifetime of  $\approx 0.5 \times 10^{-24}$  s [34]. The top quark's lifetime is shorter than that of the hadronisation process, and it therefore decays before hadronising. We therefore cannot measure the top quark directly, but indirectly via its decay products. Top quarks almost always decay to a  $W$  boson and a  $b$ -quark ( $\frac{\Gamma(Wb)}{\Gamma(Wq(q=b,s,d))} = 0.957 \pm 0.034$  [34]).  $b$ -quarks are the second heaviest quark in the SM, however their lifetimes are still longer than the hadronisation time scale. In hadron collider experiments,  $b$ -quarks travel a short distance in the detector before hadronising to form jets. In Table 2.1, the dominant final state branching fractions of the top quark, are shown.

Hadronic final states are more than twice as likely than leptonic final states. Final state decays to different lepton flavours are roughly equally probable.

Top quark production can be placed into two main categories: pair production ( $t\bar{t}$ ) and single-top production ( $t$ ). In

Decay Mode	Branching Fraction ( $\frac{\Gamma_i}{\Gamma}$ )
$t \rightarrow Wb \rightarrow e\nu_e b$	$(11.10 \pm 0.30)\%$
$t \rightarrow Wb \rightarrow \mu\nu_\mu b$	$(11.40 \pm 0.20)\%$
$t \rightarrow Wb \rightarrow \tau\nu_\tau b$	$(10.70 \pm 0.50)\%$
$t \rightarrow Wb \rightarrow q\bar{q}b$	$(66.50 \pm 1.40)\%$

Table 2.1: The dominant final state branching fractions of the top quark [34] are shown.

the LHC, top quarks are mainly produced in pairs via strong interactions in gluon-gluon fusion ( $gg \rightarrow t\bar{t}$ ) or quark annihilation ( $q\bar{q} \rightarrow t\bar{t}$ ). Top quark production via gluon-gluon fusion is the dominating process, since gluons are the most dominant particles produced in  $pp$  collisions in the LHC. The production cross section for  $t\bar{t}$  (leptonic final state) in  $pp$  collisions with  $\sqrt{s} = 13$  TeV was measured by ATLAS with a value of  $830 \pm 0.4(\text{stat}) \pm 36(\text{syst}) \pm 14(\text{lumi})$  pb [4], with good agreement between measurement and theoretical prediction.

The most abundant mechanisms leading to single top production include, those involving the exchange of a  $W$  boson and those involving the production of a top quark in association with a  $W$  boson. In Table 2.2, single top production cross sections in  $pp$  collisions at  $\sqrt{s} = 13$  TeV for various channels, are shown.

Process	Total Cross Section [pb]
$bq' \rightarrow W \rightarrow tq$	$216.99^{+9.04}_{-7.71}$
$q\bar{q}' \rightarrow W \rightarrow \bar{b}t$	$10.32^{+0.40}_{-0.36}$
$bg \rightarrow b/t \rightarrow Wt$	$71.7 \pm 3.85$

Table 2.2: Single top production cross sections in  $pp$  collisions at  $\sqrt{s} = 13$  TeV for various channels [22] are shown. The prime superscript on  $q'$  indicates that it has a different flavour to  $q$ .

Single top production is suppressed compared to pair produced top production, with  $t\bar{t}$  production (leptonic final state) being around three times as likely to occur than single top production across all decay channels.

## 2.2 $tWZ$

### 2.2.1 Tetralepton Channel

In Figure 2.2, the Leading Order (LO) Feynman diagram for  $tWZ$  in the tetra-lepton channel, is shown.

#### 2.2.1.1 Backgrounds

The main backgrounds for  $tWZ$  (tetra-lepton channel) are the production of a two tops, both in the  $\ell\nu b$  final state channel, together with a  $Z$  boson ( $t\bar{t}Z$ ) and diboson production with fully leptonic final states ( $ZZ$ ). In Figure 2.2.1.1, LO Feynman diagrams for  $t\bar{t}Z$  and  $ZZ$  in the tetralepton channel, are shown.

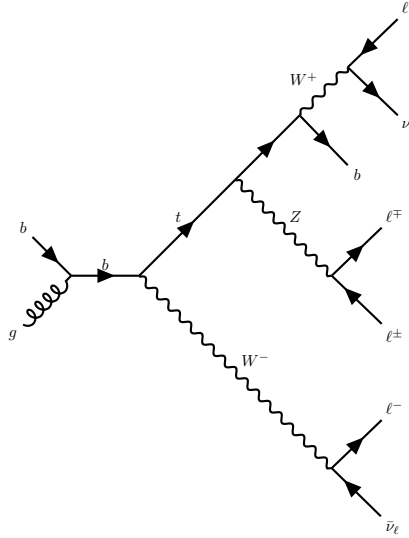


Figure 2.2: The LO Feynman diagram of  $tWZ$  production in the tetra-lepton channel is shown.

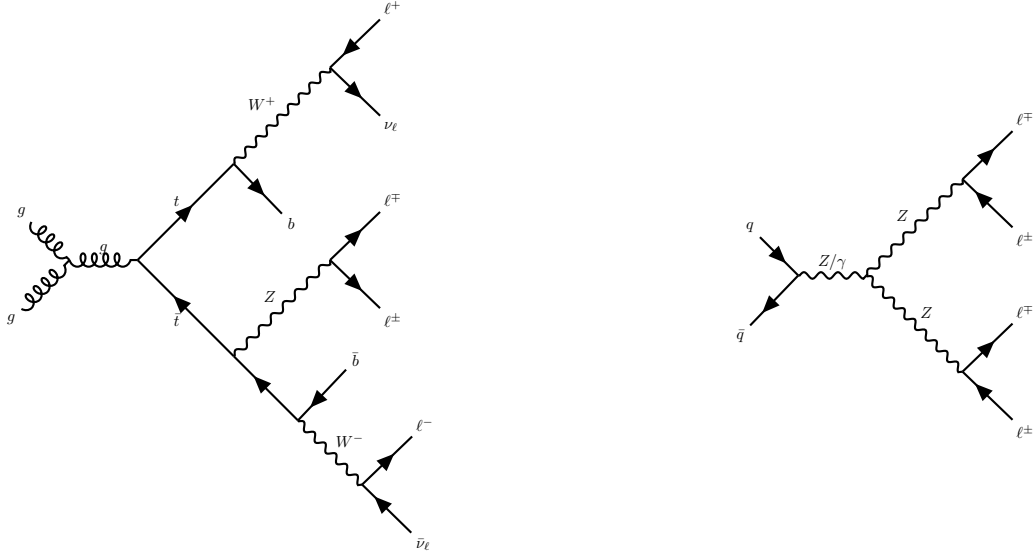


Figure 2.3: LO Feynman diagrams for  $t\bar{t}Z$  (left) and  $ZZ$  (right) in the tetralepton channel are shown.

$t\bar{t}Z$  contains four leptons and two  $b$ -quarks in its final state (inclusive  $\sigma(t\bar{t}Z) = 0.95 \pm 0.08_{\text{stat}} \pm 0.10_{\text{syst}} \text{ pb}$  at  $\sqrt{s} = 13 \text{ TeV}$  [2]) and can easily mimic the  $tWZ$  signal process, for instance, by one of its  $b$ -jets getting missed during detection.  $ZZ$  contains four leptons and zero  $b$ -quarks in its final state (inclusive  $\sigma(ZZ) = 14.6^{+1.9}_{-1.8}(\text{stat})^{+0.5}_{-0.3}(\text{syst}) \pm 0.2(\text{theo}) \pm 0.4(\text{lumi}) \text{ pb}$  at  $\sqrt{s} = 13 \text{ TeV}$  [40]). One way in which  $ZZ$  can mimic the  $tWZ$  signal process is by reconstruction of a non-prompt  $b$ -jet.

## 2.2.2 Comparison to Trilepton Channel

The most apparent difference between the tri and tetra-lepton channels is the amount of statistics present, with the tetra-lepton channel having far less events in its phase space than that of the tri-lepton channel. The lack of statistics in the tetra-lepton channel can be attributed to its low production cross section,  $\sigma_{(tW^\pm Z), Br(4\ell)}^{\text{NLO}} = 0.7 \text{ fb}$ [19]. The tri-lepton channel has a production cross section ( $\sigma_{(tW^\pm Z), Br(3\ell)}^{\text{NLO}} = 3.9 \text{ fb}$ [19]) around a factor of 4 larger than that of the tetra-lepton channel. This difference between the production cross section of the two decay channels can be largely attributed to the difference in branching ratios ( $\frac{\Gamma_i}{\Gamma}$ ) between a hadronically decaying  $W$  boson,  $\frac{\Gamma_{W \rightarrow \text{had}}}{\Gamma_W} = (67.41 \pm 0.27)\%$ [34], present in the tri-lepton channel and a leptonically decaying  $W$  boson,  $\frac{\Gamma_{W \rightarrow \ell\nu}}{\Gamma_W} = (10.86 \pm 0.09)\%$ [34], present in the tetra-lepton channel.

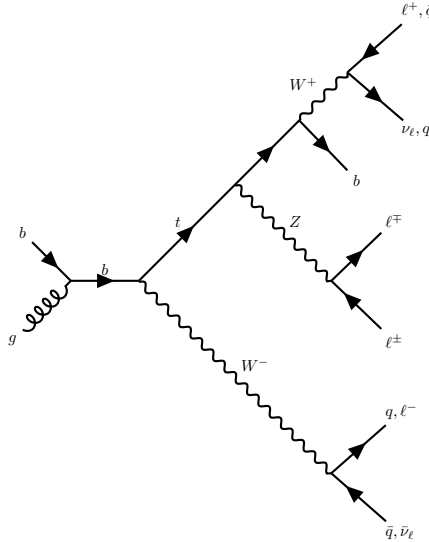


Figure 2.4: Example Feynman diagram of  $tWZ$  production in the tri-lepton channel.

Despite the tetralepton channel's low statistics, it is not subject to the large  $WZ$  background present in the trilepton channel. The tetralepton channel has a relatively large  $ZZ$  background (not present in the trilepton channel), fortunately this can be easily suppressed due to the full reconstructability of the two leptonically decaying  $Z$ -bosons.

### 2.2.3 Motivation for the search for $tWZ$ production in the tetralepton channel

The recent lack of signs of new physics from LHC data tells us that new physics is either very heavy, or is very weakly coupled to SM particles. We therefore might only observe signs of new physics in anomalous rates of well-chosen processes.  $tWZ$  is a prime example of such a process. It has an extremely low production cross section (0.7 fb for  $\sqrt{s} = 13$  TeV [19]), and has subsequently never been observed by any particle physics experiment. Since  $tWZ$  involves a charged  $W$  boson and neutral  $Z$  boson, its cross section is sensitive to the charged and neutral couplings to the top quark. In turn, the top quark is strongly coupled to the Higgs boson, due to its large mass. In the SM Lagrangian, the top quark causes the Higgs boson mass to diverge to the Planck scale. Many BSM theories aim to get rid of this Higgs mass divergence to the Planck scale.  $tWZ$  is therefore an important process in the search for signs of new physics and BSM physics.

Standard Model Effective Field Theory (SMEFT) is such a BSM theory which is sensitive to  $tWZ$  production. SMEFT attempts to describe physics at large energy scales which we have not yet been able to probe experimentally. SMEFT inherits the same QFT framework as the SM, and adds Lagrangian terms to the SM Lagrangian which describe the interactions of SM particles at higher energy scales. Analogous to the coupling constants found in the SM Lagrangian, which indicate the interaction strengths between different particles, SMEFT contains scalars which operate in the same way. These scalar coefficients are known as Wilson coefficients. It has been shown that the cross section of  $tWZ$  is sensitive to many Wilson coefficients. An experimental constraint on the cross section of  $tWZ$  is therefore expected to be impactful on a global fit on all the Wilson coefficients in SMEFT.

Prior to this analysis, only two experimental studies of  $tWZ$  in ATLAS have been done. Both take advantage of trilepton channel to search for  $tWZ$  production. The first search utilised,  $36\text{ fb}^{-1}$  of ATLAS data and an upper limit on the cross section of  $tWZ$  was set at a value of  $\approx 6$  times the SM cross section [48]. The second search utilised  $139\text{ fb}^{-1}$  (Full Run 2) of ATLAS data and an expected upper limit on the cross section of  $tWZ$  was set at a value of  $\approx 2.6$  times the SM cross section [56]. In Section 4.11.2, the latter analysis will be used in combination with this analysis, in order to further increase the sensitivity of  $tWZ$ .

## Chapter 3

# The ATLAS Experiment and Detector

### 3.1 The ATLAS Experiment

ATLAS (A Toroidal LHC ApparatuS) is one of two general purpose detectors at CERN (the European Organization for Nuclear Research) near Geneva in Switzerland. These detectors collect data from the collisions provided by the worlds highest energy particle accelerator [20], the Large Hadron Collider (LHC) situated at CERN.

In this section, information about the LHC and the ATLAS detector are given. This includes technical aspects of the ATLAS detector and the processing of data into meaningful physics objects to be used in analyses.

#### 3.1.1 Large Hadron Collider (LHC)

The LHC is a circular 27km particle accelerator located in an underground tunnel on the border between France and Switzerland. The accelerator consists of supercooled, superconducting magnets which accelerate and collide beams of protons at centre-of-mass energies up to  $\sqrt{s} = 13\text{TeV}$  at instantaneous luminosities of  $\mathcal{L} \sim 10^{34}\text{cm}^{-2}\text{s}^{-1}$ . The LHC mainly produces these proton-proton collisions, however heavy-ion collisions can be produced (typically lasting a month, annually) which reach centre-of-mass energies of  $\sqrt{s} = 5.02\text{TeV}/\text{nucleon}$  at instantaneous luminosities of  $\mathcal{L} \sim 10^{27}\text{cm}^{-2}\text{s}^{-1}$ . Proton-proton beams consist of bunches of protons which collide every 25ns, corresponding to a frequency of 40MHz.

Several accelerator systems are used to accelerate protons and heavy ions to such high energies. Protons are extracted from a tank of ionised hydrogen gas and are injected into the Linear Accelerator 2 (LINAC), where they are linearly accelerated to momenta of 50MeV. The proton bunches are then sequentially accelerated by a chain of circular accelerators. The chain starts with the Booster which accelerates the protons to momenta of up to 1.4GeV. The proton bunches are then fed through to the Proton Synchrotron (PS) and the Super Proton Synchrotron (SPS) which accelerate the protons to momenta of up to 25GeV and 450GeV respectively. The protons are then transferred to two beam pipes of the LHC where they travel in opposite directions. Both proton beams are accelerated to their final momenta of 6.5TeV, resulting in a centre-of-mass energy of 13TeV. These proton beams then collide at one of the four main interaction points situated along the LHC.

The four main experiments located at the interaction points are ATLAS, the Compact Muon Solenoid (CMS), Large Hadron Collider Beauty (LHCb) Experiment and A Large Ion Collider Experiment (ALICE). ATLAS and CMS are general-purpose detectors which investigate a wide range of physics processes. Since both ATLAS and CMS can measure the same processes, they are able to cross-check and validate measurements taken by one another. LHCb is specifically designed to study decays of particles containing  $b$ -quarks. ALICE is designed to study the strongly interacting quark-gluon plasma which is formed at extremely high energy densities.

At the interaction points, the two proton beams which consist of protons in closely packed bunches, travel in opposite directions to one another and collide. We are only able to study one  $p - p$  collision (event) at a time, however many hard  $p - p$  collisions can occur per bunch crossing. These additional collisions are referred to as *pile-up*. Pileup complicates the reconstruction of the particles originating from the hard collision of interest.

## 3.2 The ATLAS Detector

The ATLAS detector is a general purpose particle detector, located at one of the four interaction points along the LHC beam pipe (100 m below ground). In Figure 3.1, the schematic of the ATLAS detector, is shown.

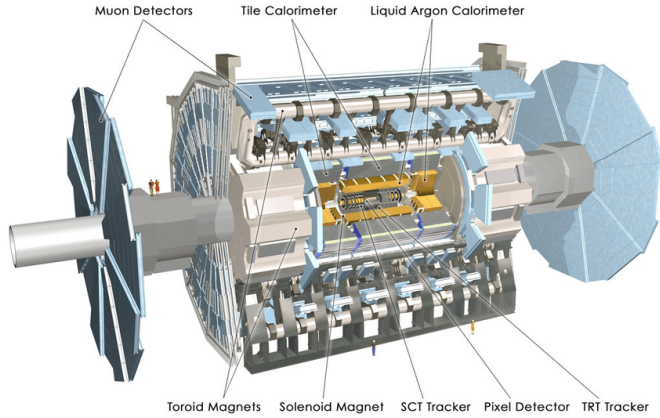


Figure 3.1: Schematic of the ATLAS detector [26]

The detector is cylindrically shaped which covers close to  $4\pi$  in solid angle. It has a length of 44 m, a diameter of 25 m and a mass of 7000 tons. ATLAS consists of four main sub-detectors arranged in concentric cylindrical layers around the beam pipe. These include the inner detector, the electromagnetic calorimeter, the hadronic calorimeters and the muon spectrometer. The sub-detectors record the momenta, energies and trajectories of different particles produced in the collider, allowing for the reconstruction and identification of these particles to be used in physics analyses.

### 3.2.1 Coordinate System and Kinematics

The ATLAS detector adopts a right-handed coordinate system. The origin is at the nominal interaction point with the beam direction defining the  $z$ -axis. The  $x - y$  plane (or transverse plane) is perpendicular to the beam line, with the  $x$ -axis pointing towards the centre of the LHC ring and the  $y$ -axis pointing upwards towards the Earth's surface. The azimuthal angle,  $\phi \in [-\pi, \pi]$ , is measured in the transverse plane with respect to the positive  $x$ -axis. The polar angle,  $\theta \in [0, \pi]$ , is measured in the  $z - y$  plane with respect to the positive  $y$ -axis. A quantity called the pseudorapidity,  $\eta \in [0, \infty]$  is defined as,

$$\eta = -\ln \tan\left(\frac{\theta}{2}\right) \quad (3.1)$$

$\eta$  is often used as a measure of the polar angle, instead of  $\theta$ , since the difference in  $\eta$  between two particles,  $\Delta\eta$ , is invariant under a Lorentz boost in the  $z$ -direction. The angular distance between two physics objects,  $\Delta R$ , can be written as,

$$\Delta R = \sqrt{(\Delta\phi)^2 + (\Delta\eta)^2} \quad (3.2)$$

where  $\Delta\phi$  is the difference in  $\phi$  between the two physics objects of interest. Quantities defined in the transverse plane are often used to describe the kinematics of physics objects in hadron collider experiments. The transverse momentum,  $p_T$ , is defined as,

$$p_T = \sqrt{(p_x)^2 + (p_y)^2} \quad (3.3)$$

where  $p_x$  and  $p_y$  are the  $x$  and  $y$  components of the physics object's momenta, respectively. The transverse energy,  $E_T$ , is defined as,

$$E_T = \sqrt{m^2 + p_T^2} \quad (3.4)$$

where  $m$  is the invariant mass of the physics object.

### 3.2.2 Inner Detector

The inner detector is the first layer of concentric cylindrical sub-detector layers in the ATLAS detector. It is used to identify charged particles and reconstruct the trajectories of charged particles produced in the collisions via energy deposition in semiconductor material (hits) and the ionisation of gas. It consists of three complementary sub-detectors (in order from nearest to farthest from the beam pipe): the Pixel Detector, the Semiconductor Tracker (SCT) and the Transition Radiation Detector (TRT). The Pixel Detector and SCT are based on semiconductor technology and have the highest granularity of any sub-detector in ATLAS, in order to cope with the high frequency of collisions near the interaction point. The TRT consists of drift tubes (straws) containing a mixture of gas (70% Xe, 27% CO<sub>2</sub> and 3% O<sub>2</sub>), which allows measurement of the energy deposited by charged particles through the ionisation of the gas. Solenoid magnets surround the inner detector and bend the trajectories of charged particles. The charges and momenta of particles can be inferred from their bent trajectories, which are reconstructed by the hits produced via energy deposition in the Inner Detector.

### 3.2.3 Electromagnetic and Hadronic Calorimeters

The Electromagnetic Calorimeter (ECAL) and Hadronic Calorimeter (HCAL) surround the Inner Detector, with the ECAL nearer to the beam line. The ECAL and HCAL provide accurate measurements of the energy of particles which interact electromagnetically (e.g. photons and electrons) and hadronically (e.g. jets), respectively. Particles entering the calorimeters interact with the detector material and create either a electromagnetic shower (in the ECAL) or a hadronic shower (in the HCAL), depositing all their energy in the calorimeter cells. The calorimeters consist of an active material and a passive absorber material. Active materials are used to measure the energy deposited by the particles and passive absorber materials induce the electromagnetic and hadronic showers. The ECAL uses liquid argon (LAr) as its active material and lead as its absorber material. The HCAL uses alternating steel absorber layers and plastic scintillating tile layers as its active material. The primary mechanism of energy deposition in the ECAL is through bremsstrahlung (for electrons) and pair production (photons). Hadrons usually deposit a small amount of their energy in the ECAL, and interact via inelastic scattering with the nuclei of the detector material. The hadronic showers (jets) produced in these nuclear interactions travel much further than an electromagnetic shower, and for that reason, the volume of the is designed HCAL occupies a much larger space than that of the ECAL.

### 3.2.4 Muon Spectrometer

The Muon Spectrometer (MS) is the outermost sub-detector of ATLAS and surrounds the HCAL. Muons traverse through the inner detector and calorimeters, with minimal energy loss, before reaching the MS. The MS consists of trigger and high-precision tracking systems. Large superconducting toroid shaped magnets deflect the incoming muons to measure their trajectories and subsequently their momenta via the curvature of the trajectories. The MS measures muon trajectories as they ionize gas (filled with Ar and CO<sub>2</sub> gas) in the MS drift chambers.

### 3.2.5 Trigger and Data Acquisition System

The Trigger and Data Acquisition System (TDAQ) manages and handles the large amount of data produced within the ATLAS detector. In Run 2,  $p - p$  bunch crossings occur every 25 ns, corresponding to an event rate of 40 MHz [26]. The TDAQ system performs a fast preliminary reconstruction to select events with signatures which are interesting for physics analyses. The information collected from these events are permanently stored for offline reconstruction and analysis, and the rest (the vast majority of events) are discarded. The trigger system reduces the 40 MHz data rate to around 1 kHz [26].

## Chapter 4

# Analysis Setup and Strategy

### 4.1 Data and Monte Carlo Simulation

#### 4.1.1 Data Samples

The  $pp$  collision data used in this analysis was collected with the ATLAS detector at the LHC from 2015 to 2018. This data period of data taking is referred to as Run 2. During this period,  $pp$  collisions at  $\sqrt{s} = 13$  TeV, corresponding to an integrated luminosity ( $\mathcal{L}$ ) of  $156 \text{ fb}^{-1}$ , were delivered by the LHC. The ATLAS detector managed to record  $147 \text{ fb}^{-1}$  of this total delivered data.  $139 \text{ fb}^{-1}$  of the data recorded by ATLAS is considered to be good enough for physics analyses (the data passes certain quality control criteria) and placed into the *Good Runs List* [33]. We use the Run 2 datasets from the Good Runs List, called `mc16a`, `mc16d` and `mc16e` with integrated luminosity's of  $36.2 \text{ fb}^{-1}$ ,  $44.3 \text{ fb}^{-1}$  and  $58.5 \text{ fb}^{-1}$  respectively.

#### 4.1.2 Monte Carlo Samples

Simulated Monte Carlo (MC) samples were generated and used to model the SM  $tWZ$  signal and its backgrounds.

The following background processes are considered:

- **$t\bar{t}Z$ :**  $t\bar{t}$  with an associated  $Z$ -boson, in the tetralepton final state. Therefore, both top-quarks decay leptonically (e.g.  $t \rightarrow W^+ b \rightarrow \ell^+ \nu b$ ) and of these top-quarks emits a  $Z$ -boson which decays leptonically ( $Z \rightarrow \ell^\pm \ell^\mp$  (OSSF lepton pair) ). This results in a final state with 4 leptons and 2 b-quarks.
- **$ZZ$ :** Diboson production with a tetralepton final state, therefore both  $Z$ -bosons decay leptonically ( $Z \rightarrow \ell^\pm \ell^\mp$  (OSSF lepton pair) ).
- **other:** Processes with a relatively minimal, but non-negligible background contribution
  - $VVV (V = W/Z)$
  - $t\bar{t}$
  - $t\bar{t}W$
  - $t\bar{t}WW$
  - $t\bar{t}H$
  - $WZ$
  - $t\bar{t}t$
  - $t\bar{t}t\bar{t}$
  - $tZq$

The MC simulations are achieved via the use of event generators and parton shower generators. Event generators simulate the  $pp$  collisions (hard events) by sampling the proton's Parton Distribution Functions (PDFs) at the desired energy scale. The parton shower generators simulate any incoming or outgoing particles from the hard

process, which carry QCD color charge and can therefore lead to parton showers.

The production of  $tWZ$  events is simulated with the **MADGRAPH5\_AMC@NLO 2.3.3** generator providing matrix element (ME) calculations at NLO. The events are interfaced with **PYTHIA 8.235** for the parton shower.

The production of  $t\bar{t}Z$  and  $t\bar{t}W$  events are simulated with the **MADGRAPH5\_AMC@NLO 2.3.3** generator providing ME calculations at NLO. The events are interfaced with **PYTHIA 8.210** for the parton shower.

Event generation of  $tWZ$  and  $t\bar{t}Z$  results in diagrams which overlap with one another, that is, these diagrams contain the same initial and final state particles. Several methods exist in order to separate between the two processes, by removing the overlap, therefore avoiding double counting. There are two different diagram removal procedures, diagram removal procedure 1 (DR1) [27] and diagram removal procedure 2. We use the DR1 scheme to remove the overlap (interference) between  $tWZ$  and  $t\bar{t}Z$ .

Diboson processes which feature the three charged leptons and one neutrino or four charged lepton in their final states, such as  $WZ$  and  $ZZ$ , are simulated using **SHERPA 2.2.2** at NLO precision. The events are interfaced with **SHERPA** for the parton shower.

Fully leptonic triboson processes such as  $WWW$ ,  $WWZ$ ,  $WZZ$ , and  $ZZZ$  containing up to six leptons in their final states are simulated using **SHERPA 2.2.2** at NLO precision. The events are interfaced with **SHERPA** for the parton shower.

The production of  $t\bar{t}$  events are simulated with the **POWHEG** generator providing ME calculations at NLO. The events are interfaced with **PYTHIA 8.210** for the parton shower.

The production of  $t\bar{t}t$ ,  $t\bar{t}t\bar{t}$  and  $t\bar{t}WW$  are simulated using the **MADGRAPH5\_AMC@NLO 2.2.2** generator at LO precision. The events are interfaced with **PYTHIA 8.186** for the parton shower.

The production of  $t\bar{t}$  with an associated Higgs boson,  $t\bar{t}H$ , are generated using the **MADGRAPH5\_AMC@NLO 2.6.0** generator at NLO precision. The events are showered using **PYTHIA 8.230**.

The production of  $t\bar{t}$  events is simulated with the **POWHEG** generator providing ME calcualtions at NLO. The events are showered using **PYTHIA 8.230**.

The production of a single top quark in association with a  $Z$ -boson and an extra parton,  $tZq$ , is simulated using **MADGRAPH5\_AMC@NLO 2.3.3** at NLO prescision. The events are interfaced with **PYTHIA 8.230** for the parton shower.

In Table 4.1, the event generator and parton shower used for each process's sample are shown.

## 4.2 Objects

In this section the physics objects (leptons, jets and  $b$ -tagged jets) used in this analysis are outlined.

Process	Event Generator	Cross section calculation	Parton Shower
$tWZ$	MADGRAPH5_AMC@NLO 2.3.3	NLO	PYTHIA 8.235
$t\bar{t}Z$	MADGRAPH5_AMC@NLO 2.3.3	NLO	PYTHIA 8.210
$ZZ, WZ$	SHERPA 2.2.2	NLO	SHERPA
$VVV (V = W/Z)$	SHERPA 2.2.2	NLO	SHERPA
$t\bar{t}$	POWHEG	NLO	PYTHIA 8.230
$t\bar{t}W$	MADGRAPH5_AMC@NLO 2.3.3	NLO	PYTHIA 8.210
$t\bar{t}WW$	MADGRAPH5_AMC@NLO 2.2.2	LO	PYTHIA 8.186
$t\bar{t}H$	MADGRAPH5_AMC@NLO 2.6.0	NLO	PYTHIA 8.230
$t\bar{t}t, t\bar{t}t\bar{t}$	MADGRAPH5_AMC@NLO 2.2.2	LO	PYTHIA 8.186
$tZq$	MADGRAPH5_AMC@NLO 2.3.3	NLO	PYTHIA 8.230

Table 4.1: The event generator and parton shower used for the signal and background process's MC samples is shown.

### 4.2.1 Leptons

In this analysis we only consider  $e$  and  $\mu$  leptons, since  $\tau$  leptons are difficult to detect in the ATLAS detector.  $\tau$  leptons are challenging to detect since they have an extremely short lifetime ( $290.3 \pm 0.5$  fs [34]) which causes them to decay before reaching any detector components and therefore can only be reconstructed via their decay products.

In addition to our selection criteria of exactly four leptons, we require that the Leading (L), Next-to-Leading (NL), Next-to-Next-to-Leading (NNL) and Next-to-Next-to-Next-to-Leading (NNNL) leptons have  $p_T$  greater than 28, 18, 10 and 10 GeV respectively. Here we have chosen to apply relatively loose object-level cuts in an attempt to maximize our signal statistics, since the analysis is heavily statistically limited.

Reconstructed electrons are required to be within  $|\eta| < 2.47$  and excluding the transition region between the barrel and end-cap calorimeters at  $1.37 < |\eta| < 1.52$ . Reconstructed muons are required to be within  $|\eta| < 2.5$ .

The transverse impact parameter,  $d_0$ , is defined as the minimal spacial distance between the object's (here we are referring to leptons) trajectory and the primary vertex (the vertex associated with the  $p$ - $p$  hard scatter). The longitudinal impact parameter,  $z_0$ , is defined as the value of  $z$  of the point on the object's trajectory which determines  $d_0$ . To ensure consistency between the lepton and the primary vertex, we require that  $|\frac{d_0}{\sigma(d_0)}| < 5$ ,  $|z_0 \sin \theta| < 0.5$  mm for electrons and  $|\frac{d_0}{\sigma(d_0)}| < 3$ ,  $|z_0 \sin \theta| < 0.5$  mm for muons, following the current recommendations [53].

To avoid instances where one detector signal can result in multiple different reconstructed objects, an overlap removal is applied which ignores all but one of these objects. We use the current recommended configuration [32].

Electrons are selected using a likelihood based discriminant [1] which takes measurements from the tracking system, calorimeter system and quantities derived from both the tracking and calorimeter system as input. Muons are selected using AnalysisBase's Muon Selection Tool [47].

Loose electrons are defined with the criteria above, using the `LooseAndBLayerLH` ( $\sim 91\%$  selection efficiency for electrons with  $E_T > 30$  GeV [28]) identification working point. Similarly, tight electrons are defined with the criteria above, using the `TightLH` ( $\sim 80\%$  selection efficiency for electrons with  $E_T > 30$  GeV [28]) identification working point. Both loose and tight muons use the `Medium` ( $\sim 95\%$  selection efficiency [5]) identification working point.

Tight leptons additionally require that they are sufficiently isolated from other particles produced in the collision. This is done by defining a cone of radius  $\Delta R = \sqrt{\Delta\eta^2 + \Delta\phi^2}$  around the particle of interest and summing the  $p_T$  of all the reconstructed particles surrounding the particle of interest, situated within the cone. A quantity,  $I_{rel}$ , is then defined as  $I_{rel} = \frac{\sum p_T(\text{surrounding candidate})}{p_T(\text{candidate})}$ , the ratio of this sum to the  $p_T$  of the lepton candidate. If this value is large, it is likely that the particle of interest originated from a jet (together with many other particles), whereas a prompt decay product resulting from the hard scatter will have little to no energy surrounding it ( $I_{rel} \ll 1$ ). We use Analysis Base's `IsolationSelectionTool` with the `PLVTight` ( $\sim 70\%$  efficiency [6]) and `PLVTight` ( $\sim 70\%$  efficiency at  $p_T = 30\text{ GeV}$  [24]) working points for tight electrons and tight muons respectively (following the current recommendations [51]).

In Table 4.2, a summary of the selection criteria for leptons is shown.

	Electrons		Muons	
	Tight	Loose	Tight	Loose
$p_T$ cuts	$p_T(\ell_1, \ell_2, \ell_3, \ell_4) > (28, 18, 10, 10) \text{ GeV}$			
Overlap Removal	"recommended"			
$\eta$ cuts	$ \eta(\ell_e)  < 2.47$ excluding $1.37 <  \eta(\ell_e)  < 1.52$		$ \eta(\ell_\mu)  < 2.5$	
Impact Parameters	$ \frac{d_0}{\sigma(d_0)}  < 5$ , $ z_0 \sin \theta  < 0.5 \text{ mm}$		$ \frac{d_0}{\sigma(d_0)}  < 3$ , $ z_0 \sin \theta  < 0.5 \text{ mm}$	
Identification WP	TightLH	LooseAndBLayerLH	Medium	Medium
Isolation WP	PLVTight	Not Used	PLVTight	Not Used

Table 4.2: A summary of the requirements applied for selecting tight and loose leptons ( $e, \mu$ ) is shown.

### 4.2.2 Jets

Jets are reconstructed from topological clusters using the anti- $k_t$  algorithm. Topological clusters are groups of adjacent calorimeter cells which originate from *seed* cells. Seed cells are defined to contain at least 4 times the average amount of noise expected in the cell<sup>1</sup>. All cells adjacent to the seed cell are grouped together given that the energy deposited within the cell is at least  $2\sigma$ . This process is repeated until there are no adjacent cells which meet the above criteria. All adjacent cells to the cluster are then added, with no requirement on the energy deposited within these cells. We use the `AntiKt4EMFlowjets` ( $\sim 97\%$  average efficiency with JVT (outlined in the subsequent paragraph)  $> 0.2$  [53]) working point (following the current recommendations [53]).

The jet-vertex-tagger (JVT) and the forward jet-vertex-tagger (fJVT) are likelihood discriminant which aim to suppress pile-up jets. We use the `Medium` working point for the JVT and the fJVT (following the current recommendations [50]). We additionally require that jets have a JVT value greater than 0.5.

Jets are required to be within  $p_T(\text{jet}) > 20\text{ GeV}$ . We apply these looser  $p_T$  cuts in an attempt to increase our limited signal statistics. A forward jet is a signature of single top production, we therefore require jets to have  $|\eta| < 4.5$  in order to include these forward jets.

### 4.2.3 $b$ -tagging

The DL1r  $b$ -tagger [46] was used to identify jets as  $b$ -jets. The DL1r algorithm combines outputs from several low-level tagging algorithms using a Deep Neural Network and outputs the probability that a given input jet is identified as a  $b$ ,  $c$  or light flavoured jet. We use different DL1r working points to identify  $b$ -jets in our event selection (See Section 4.4). The working points are defined based off a cut on the DL1r score corresponding to a  $b$ -jet tagging efficiency of 60%, 70%, 77% and 85%.

<sup>1</sup> $\sigma$ : average noise in a given cell

Since we are heavily statistically limited, we aim to increase the amount of statistics in our regions. In an attempt to achieve this goal in the  $t\bar{t}Z$  CR,  $b$ -tagged jets were placed under *tight* and *loose* definitions. A tight  $b$ -tagged jet is defined as a jet which passes the 77%, 70%, 65% or 60% DL1r  $b$ -tagger working point. A loose  $b$ -tagged jet is defined as a jet which passes 85% DL1r  $b$ -tagger working point, but not the 77%, 70%, 65% or 60% DL1r  $b$ -tagger working points. Different numbers (and definitions) of tight and loose  $b$ -tagged jets were tried in each region, with the final selection criteria being chosen which maximised the expected significance of  $\sigma(tWZ)$  (See Section 4.4.1).

### 4.3 Kinematic cuts

The invariant mass of the OSSF lepton pair coming from the  $Z$  boson must equal the invariant mass of the  $Z$  boson, and noting that  $e,\mu$  reconstruction and identification in the ATLAS detector has a high efficiency [41], we can use these OSSF leptons to reconstruct  $Z$  bosons with relatively high confidence. We therefore define a  $Z$  candidate as an OSSF lepton pair with an invariant mass,  $m_{\text{OSSF}}$ , satisfying the condition,  $|m_{\text{OSSF}} - m_Z| < 30 \text{ GeV}$ , where  $m(Z)$  is the nominal  $Z$  boson mass ( $91.1876 \text{ GeV}$  [34]). We use this wider mass window to cover the full range of the  $m(Z)$  distribution, in an attempt to increase the number of events which pass our baseline selections. Multiple  $Z$  candidates can be present in certain decay channels (e.g.  $eeee$ ,  $\mu\mu ee$ ,  $\mu\mu\mu\mu$ ). In these cases, the  $Z$  candidate which has an invariant mass closest to the nominal  $Z$  boson mass is chosen.

In order to suppress potential fakes and quarkonia (low mass resonances such as  $J/\psi$  and upsilon) we require that all OSSF lepton pairs have an invariant mass,  $m_{\text{OSSF}}$ , greater than  $10 \text{ GeV}$ .

The final state lepton charges must sum to zero. We therefore require,  $\sum_{i=1}^4 \text{charge}(\ell_i) = 0$ .

### 4.4 Regions and Event Selection

We define two  $tWZ$  SRs, as opposed to one  $tWZ$  SR, in an attempt to suppress and constrain the  $ZZ$  background. We require that both  $tWZ$  SRs have exactly four tight leptons, exactly one  $Z$ -boson candidate, exactly one tight  $b$ -tagged jet (from the decay of the top quark) and greater than or equal to one jet. The two  $tWZ$  SR's differ by the flavours of their leptons which don't originate from the decay of a  $Z$ -boson (Non- $Z$  leptons). The  $ZZ$  background has two  $Z$ -bosons which decay into a pair of OSSF lepton pairs, in order to mimic the  $tWZ$  signal. We take advantage of this to define a  $tWZ$  region rich in  $ZZ$  background and one with a minimal  $ZZ$  background component. This is done by requiring that one of the  $tWZ$  SRs has its two non- $Z$  leptons to have opposite flavour and the other  $tWZ$  SR is required to have its non- $Z$  leptons to have the same flavour. These two disjoint  $tWZ$  SRs are named  $tWZ$  OF SR and  $tWZ$  SF SR respectively. We therefore expect that the  $tWZ$  SF SR contains the majority of  $tWZ$ 's  $ZZ$  background events.

In order to check the modelling of the most dominant background components in our signal region, we have modified our selection criteria to define  $t\bar{t}Z$  and  $ZZb$  control regions. The  $t\bar{t}Z$  control region has the same requirement on the number of reconstructed  $Z$  boson candidates in the signal region (due to a commonality on the number of  $Z$  bosons present in both processes), however we require at least two jets and that exactly two of these jets are  $b$ -tagged (corresponding to the  $b$ -quark jets originating from the two top-quark decays). We choose to define a  $ZZb$  region, as opposed to a  $ZZ$  region, since the  $ZZ$  background present in the  $tWZ$  signal region contains exactly one  $b$ -tagged jet. Therefore defining a region with  $ZZ$  plus exactly one  $b$ -jet more closely resembles the  $ZZ$  background present in the signal region. In addition to this, mis-modelling of  $ZZ$  has been seen in other analyses [3, 25], further motivating the use of a  $ZZb$  control region over a  $ZZ$  CR. The  $ZZb$  CR requires exactly two  $Z$  boson candidates and exactly one  $b$ -tagged jet, resulting in an implicit requirement on the number of jets ( $N_{\text{jet}} \geq 1$ ).

In order to constrain the fake lepton component contained within the  $t\bar{t}Z$  sample, we define a  $(tWZ)_{\text{fake}}$  CR which is as similar as possible to the  $tWZ$  CR but is enhanced in fakes. This is achieved by defining the  $(tWZ)_{\text{fake}}$  CR to inherit the same selection criteria as the  $tWZ$  SRs however, in this case, we require exactly 3 tight leptons

Baseline selections				
$N_\ell = 4$ $p_T(\ell_1, \ell_2, \ell_3, \ell_4) > (28, 10, 10, 10)$ GeV $p_T(\text{jet}) > 20$ GeV, $ \eta(\text{jet})  < 4.5$ , $\text{jvt} > 0.5$ $ \eta(\ell_e)  < 2.47$ excluding $1.37 <  \eta(\ell_e)  < 1.52$ $ \eta(\ell_\mu)  < 2.5$ $\sum_{i=1}^4 \text{charge}(\ell_i) = 0$ All OSSF lepton pairs require $m_{\text{OSSF}} > 10$ GeV				
Regions				
$tWZ$ OF SR	$tWZ$ SF SR	$t\bar{Z}$ CR	$ZZb$ CR	$(tWZ)_{\text{fake}}$ CR
$N_\ell(\text{tight}) = 4$	$N_\ell(\text{tight}) = 4$	$N_\ell(\text{tight}) = 4$	$N_\ell(\text{tight}) = 4$	$N_\ell(\text{tight}) = 3$ $N_\ell(\text{loose and NOT tight}) = 1$
$N_Z$ candidate = 1	$N_Z$ candidate = 1	$N_Z$ candidate = 1	$N_Z$ candidate = 2	$N_Z$ candidate = 1
$N_{\text{jet}} \geq 1$	$N_{\text{jet}} \geq 1$	$N_{\text{jet}} \geq 2$	$N_{\text{jet}} \geq 1$	$N_{\text{jet}} \geq 1$
$N_{\text{b-jet}}(\text{tight}) = 1$	$N_{\text{b-jet}}(\text{tight}) = 1$	$N_{\text{b-jet}}(\text{tight}) \geq 1$ $N_{\text{b-jet}}(\text{loose}) \geq 0$ $N_{\text{b-jet}}(\text{tight}) + N_{\text{b-jet}}(\text{loose}) = 2$	$N_{\text{b-jet}}(\text{tight}) = 1$	$N_{\text{b-jet}}(\text{tight}) = 1$
Opp. Flavour Non-Z leptons	Same Flavour Non-Z leptons	-	-	-

Table 4.3: A summary of the requirements applied for selecting events in the signal and control regions is shown.

and exactly 1 loose (and NOT tight) lepton (since looser leptons are more likely to be fakes, compared to tighter leptons). A  $(t\bar{Z})_{\text{fake}}$  CR (requiring exactly 3 tight leptons and exactly 1 loose (and NOT tight) lepton) was tried as an alternative to the  $(tWZ)_{\text{fake}}$  CR, however a much larger suppression of fakes were observed in this region (compared to the  $(tWZ)_{\text{fake}}$  CR). This suppression of fakes can be explained by the extra  $b$ -tagged jet requirement (exactly two  $b$ -tagged jets are required in the  $t\bar{Z}$  region, compared to exactly one in the  $tWZ$  SRs (See Table 4.3)) which causes suppression of fakes via the overlap removal procedure [32].

In Table 4.3, a summary of the final selection criteria and region definitions is shown.

#### 4.4.1 Optimization studies for event selection

In order to find the selection criteria for jets and leptons which maximized sensitivity to the  $tWZ$  signal, studies were performed by plotting the expected significance ( $Z_\mu^{\text{exp}}$ ) and expected upper limit ( $\mu_{\text{up}}^{\text{exp}}$ ) for different selection criteria. The fitting procedure as described in Section 4.10.1 was used to calculate the expected upper limits and expected significances in this study. The same selection criteria and regions defined in Table 4.3 was used (unless otherwise specified), except for the selection(s) which were being optimised in each case.

In Figure 4.1 the expected significance ( $Z_\mu^{\text{exp}}$ ) and expected upper limits ( $\mu_{\text{up}}^{\text{exp}}$ ) for different  $\eta(\text{jet})$  cuts are shown.

From Figure 4.1, we can see that the  $\eta(\text{jet})$  cut which maximises the sensitivity of  $tWZ$  in the tetralepton channel is requiring that  $\eta(\text{jet}) < 4.5$ . This selection criteria was set for the  $\eta(\text{jet})$  across all regions.

In Figure 4.2 the expected significance ( $Z_\mu^{\text{exp}}$ ) and expected upper limits ( $\mu_{\text{up}}^{\text{exp}}$ ) for different  $p_T(\text{jet})$  cuts are shown.

From Figure 4.2, we can see that the  $p_T(\text{jet})$  cut which maximises the sensitivity of  $tWZ$  is requiring that  $p_T(\text{jet}) > 20$  GeV. This selection criteria was set for the  $p_T(\text{jet})$  across all regions.

In Figure 4.3 the expected significance ( $Z_\mu^{\text{exp}}$ ) and expected upper limits ( $\mu_{\text{up}}^{\text{exp}}$ ) for a range of different configurations of DL1r  $b$ -tagged jet working points across different regions.

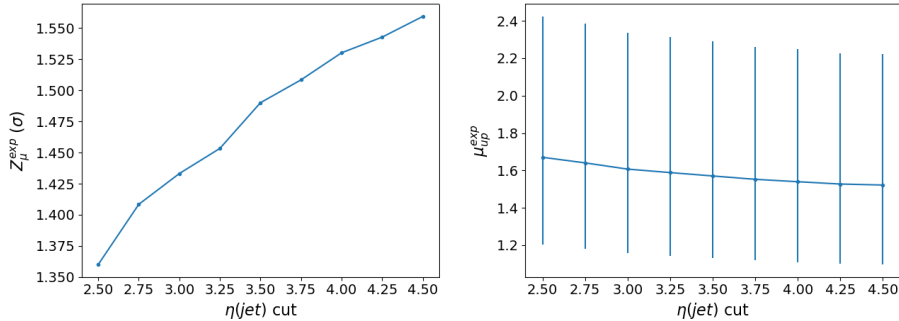


Figure 4.1: **Left:** Expected significance ( $Z_\mu^{\text{exp}}$ ) for different  $\eta(\text{jet})$  cuts is shown. The cuts applied on the  $\eta(\text{jet})$  are shown on the x-axis and corresponding expected significance from the likelihood fit is shown on the y-axis. **Right:** Expected upper limit ( $\mu_{\text{up}}^{\text{exp}}$ ) for different  $\eta(\text{jet})$  cuts is shown. The cuts applied on the  $\eta(\text{jet})$  are shown on the x-axis and corresponding expected upper limits are shown on the y-axis. Error bars representing the total uncertainty on the expected upper limits are shown as vertical lines.

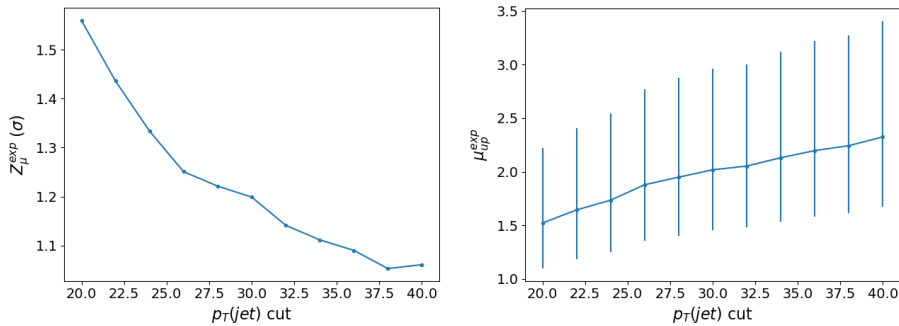


Figure 4.2: **Left:** Expected significance ( $Z_\mu^{\text{exp}}$ ) for different  $p_T(\text{jet})$  cuts is shown. The cuts applied on the  $p_T(\text{jet})$  are shown on the x-axis and corresponding expected significance from the likelihood fit is shown on the y-axis. **Right:** Expected upper limit ( $\mu_{\text{up}}^{\text{exp}}$ ) for different  $p_T(\text{jet})$  cuts is shown. The cuts applied on the  $p_T(\text{jet})$  are shown on the x-axis and corresponding expected upper limits are shown on the y-axis. Error bars representing the total uncertainty on the expected upper limits are shown as vertical lines.

From Figure 4.3, we can see that requiring that  $b$ -tagged jets pass the 77% DL1r WP in the  $tWZ$  SR,  $(tWZ)_{\text{fake}}$  CR and the  $ZZb$  CR and that at least one  $b$ -tagged jet in the  $t\bar{t}Z$  SR passes the 77% DL1r WP (the other jet is just required to pass the 85% DL1r WP) maximises the sensitivity overall (compared to the other investigated configurations). This configuration was chosen  $b$ -tagged jets.

The  $p_T(\text{L Lepton})$  is constrained by the single lepton triggers (Table ??). We choose to apply a cut on the  $p_T(\text{NL Lepton})$  slightly tighter than the tightest single lepton  $p_T$  cut in the trigger. We can however, try optimising the  $p_T(\text{NL Lepton})$  cut by comparing the expected significance and limit for a range of  $p_T(\text{NL Lepton})$  cuts to determine the cut which maximizes sensitivity.

In Figure 4.4 the expected significance ( $Z_\mu^{\text{exp}}$ ) and expected upper limits ( $\mu_{\text{up}}^{\text{exp}}$ ) for different  $p_T(\text{NL Lepton})$  cuts is shown.

Since there is a very small change between the different  $p_T(\text{NL Lepton})$  cuts on the sensitivity of  $tWZ$ , we choose to apply a  $p_T(\text{NL Lepton})$  cut at 18 GeV (avoiding a  $p_T$  cut near the sharp drop in expected significance after 28 GeV), therefore applying a cut above the tightest, looser dilepton trigger  $p_T$  cut (17 GeV) to suppress any systematic from the modelling of the trigger efficiency.

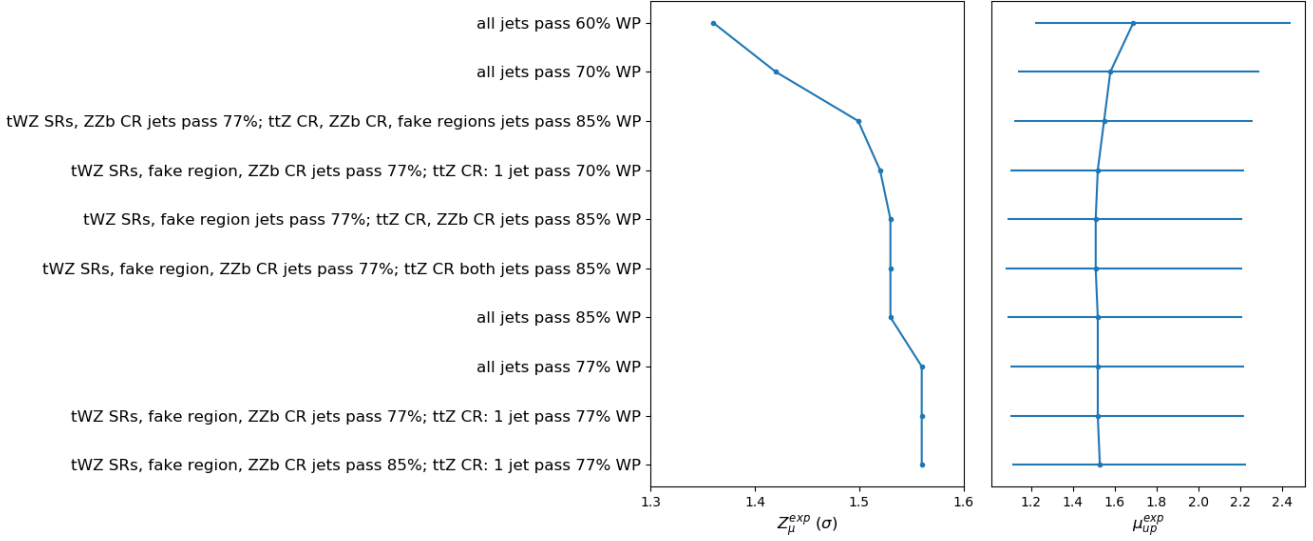


Figure 4.3: Expected significance ( $Z_\mu^{\exp}$ ) and expected upper limit ( $\mu_{up}^{\exp}$ ) for different configurations of DL1r  $b$ -tagged jet working points is shown. The common y-axis shows the different configurations of DL1r  $b$ -tagged jet working points. On the left panel, the expected significance from the likelihood fit is shown on the x-axis. On the right panel, the expected upper limit from the likelihood fit is shown on the x-axis (with the corresponding total uncertainty represented by horizontal lines).

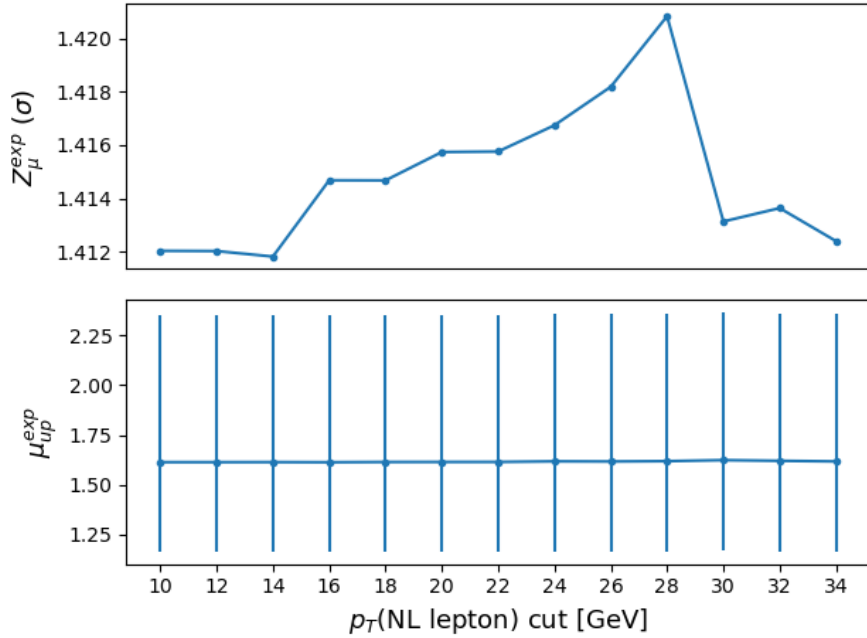


Figure 4.4: Expected significance ( $Z_\mu^{\exp}$ ) and expected upper limit ( $\mu_{up}^{\exp}$ ) for different  $p_T$ (NL Lepton) cuts is shown. The common x-axis shows cut applied to the  $p_T$  of the next-to-leading lepton. On the top panel, the expected significance from the likelihood fit is shown on the y-axis. On the bottom panel, the expected upper limit from the likelihood fit is shown on the y-axis (with the corresponding total uncertainty represented by vertical lines).

## 4.5 Signal and Control Regions

In this section, pre-fit distributions of variables in each region are shown. More pre-fit distributions for each region are shown in the appendix (Section A.1.5). For each figure in this section, the data is given by the black points and

the MC predictions for each process are given by the histograms. The vertical lines on the data points represent the total uncertainty in the data and the diagonal lined bands represent the total MC uncertainty. The lower panel in each plot shows the ratios of the data to the theoretical predictions. Bins with a  $\frac{\text{signal}}{\text{background}}$  yield greater than 0.1 are kept blinded. Blinded bins are shaded with black diagonal lines and their data points are omitted.

In Table 4.4, the pre-fit yields for each sample in each region is shown.

	$tWZ$ OF SR	$tWZ$ SF SR	$t\bar{t}Z$ CR	$ZZb$ CR	$(tWZ)_{\text{fake}}$ CR
$t\bar{t}Z$	$13.9325 \pm 1.84643$	$10.1343 \pm 1.36039$	$31.7149 \pm 4.46776$	$5.26303 \pm 0.696828$	$19.1224 \pm 2.50011$
$t\bar{t}Z$ fakes	$0.0687541 \pm 0.0482172$	$0.032827 \pm 0.026286$	$0.0709734 \pm 0.043509$	$0.0474576 \pm 0.0301512$	$4.94775 \pm 2.48939$
$tWZ$	$3.81359 \pm 0.392241$	$2.57584 \pm 0.326401$	$2.61991 \pm 0.861557$	$1.4023 \pm 0.156686$	$4.93485 \pm 0.692143$
$ZZ$	$0.546045 \pm 0.18975$	$8.76232 \pm 2.66871$	$1.22357 \pm 0.376889$	$46.0616 \pm 13.9203$	$7.76724 \pm 2.36894$
other	$t\bar{t}$	$6e-06 \pm 3.04506e-06$	$0.250783 \pm 0.44226$	$0.269883 \pm 0.223373$	$6e-06 \pm 3.04506e-06$
	$tZq$	$0.0827265 \pm 0.0399222$	$0.0757694 \pm 0.0355101$	$0.0637132 \pm 0.0293762$	$0.0590199 \pm 0.0244576$
	$t\bar{t}W$	$0.00674747 \pm 0.00793546$	$0.00279491 \pm 0.00287747$	$6e-06 \pm 3.04506e-06$	$0.00221727 \pm 0.00562041$
	$WZ$	$0.0439316 \pm 0.0241635$	$0.0397876 \pm 0.0154764$	$0.0134837 \pm 0.0128327$	$0.0474188 \pm 0.0330635$
	$t\bar{t}t$	$0.000987429 \pm 0.000768187$	$0.00249801 \pm 0.00138007$	$0.0141085 \pm 0.00486102$	$6e-06 \pm 3.04506e-06$
	$t\bar{t}\bar{t}$	$0.00934516 \pm 0.0080725$	$0.0107503 \pm 0.00852049$	$0.0570846 \pm 0.0206271$	$6e-06 \pm 3.04506e-06$
	$t\bar{t}WW$	$0.0293456 \pm 0.0263573$	$0.0296011 \pm 0.0196075$	$0.26412 \pm 0.0936908$	$0.013096 \pm 0.0323943$
	$VVV (V = W/Z)$	$0.280384 \pm 0.0866421$	$0.191257 \pm 0.0595588$	$0.0696624 \pm 0.0228108$	$0.171171 \pm 0.0526519$
	$t\bar{t}H$	$0.854064 \pm 0.177974$	$0.674566 \pm 0.141771$	$1.98187 \pm 0.406211$	$0.151447 \pm 0.0357703$
	Total	$19.6684 \pm 1.95158$	$22.7832 \pm 3.10338$	$38.3633 \pm 4.6342$	$53.2187 \pm 13.9618$
	data	-	-	36	49
					57

Table 4.4: The pre-fit yields for each sample in each region is shown.

The statistical uncertainty associated with the number of raw MC events (weighted by MC event weights) can be quantified by the Number of Equivalent Events [30],  $N_{\text{equiv}}$ , which relates the sample of  $N$  weighted events to  $N_{\text{equiv}}$  events with all MC event weights equal to 1, that would have the same relative statistical fluctuation.  $N_{\text{equiv}}$  can be written as,

$$N_{\text{equiv}} = \frac{(\sum_i^N w_i)^2}{\sum_i^N w_i^2} \quad (4.1)$$

where  $w_i$  is the MC event weight for event  $i$ . The standard uncertainty of  $N_{\text{equiv}}$  is given by  $u(N_{\text{equiv}}) = \sqrt{N_{\text{equiv}}}$ .

In Table 4.5, the number of equivalent events,  $N_{\text{equiv}}$  (and its percentage uncertainty), is shown for each sample in each region.

	$tWZ$ OF SR	$tWZ$ SF SR	$t\bar{t}Z$ CR	$ZZb$ CR	$(tWZ)_{\text{fake}}$ CR			
	$N_{\text{equiv}}$	Uncertainty [%]	$N_{\text{equiv}}$	Uncertainty [%]	$N_{\text{equiv}}$	Uncertainty [%]	$N_{\text{equiv}}$	Uncertainty [%]
$tWZ$	$6463.29 \pm 80.39$	1.24	$4153.0 \pm 64.44$	1.55	$4800.67 \pm 69.29$	1.44	$2497.07 \pm 49.97$	2.0
$t\bar{t}Z$	$1363.87 \pm 36.93$	2.71	$1031.04 \pm 32.11$	3.11	$3237.01 \pm 56.89$	1.76	$561.41 \pm 23.69$	4.22
$ZZ$	$50.89 \pm 7.13$	14.02	$97.61 \pm 31.23$	3.2	$267.85 \pm 16.37$	6.11	$7023.35 \pm 83.81$	1.19
other	$748.0 \pm 27.35$	3.66	$2.47 \pm 1.57$	63.58	$4.23 \pm 2.06$	48.6	$255.32 \pm 15.98$	6.26
$t\bar{t}Z$ fakes	$6.72 \pm 2.59$	38.56	$1.31 \pm 1.14$	87.34	$16.05 \pm 4.01$	24.96	$7.15 \pm 2.67$	37.41
Total	$8632.77 \pm 92.91$	1.08	$6163.44 \pm 78.51$	1.27	$8325.81 \pm 91.25$	1.1	$10344.3 \pm 101.71$	0.98
							$12044.27 \pm 109.75$	0.91

Table 4.5: The number of equivalent events,  $N_{\text{equiv}}$  (and its percentage uncertainty), is shown for each sample in each region.

$N_{\text{equiv}}$  is relatively large, compared to the background processes, for the  $tWZ$  signal in all regions. This tells us that we have a large number of raw MC events for the  $tWZ$  sample. An extended  $tWZ$  sample was generated to increase the number of signal events used to train the event-level BDT (See Section 4.7.2).

#### 4.5.1 $tWZ$ OF SR

In this section, pre-fit distributions of variables in the  $tWZ$  OF SR are shown. More pre-fit distributions for the  $tWZ$  OF SR are shown in the appendix (Section A.1.1).

In Figure A.1 MC predictions for  $p_T$ ,  $\eta$  and  $\phi$  for leading (L) leptons and next-to-leading (NL) leptons in the  $tWZ$  OF SR region is shown.

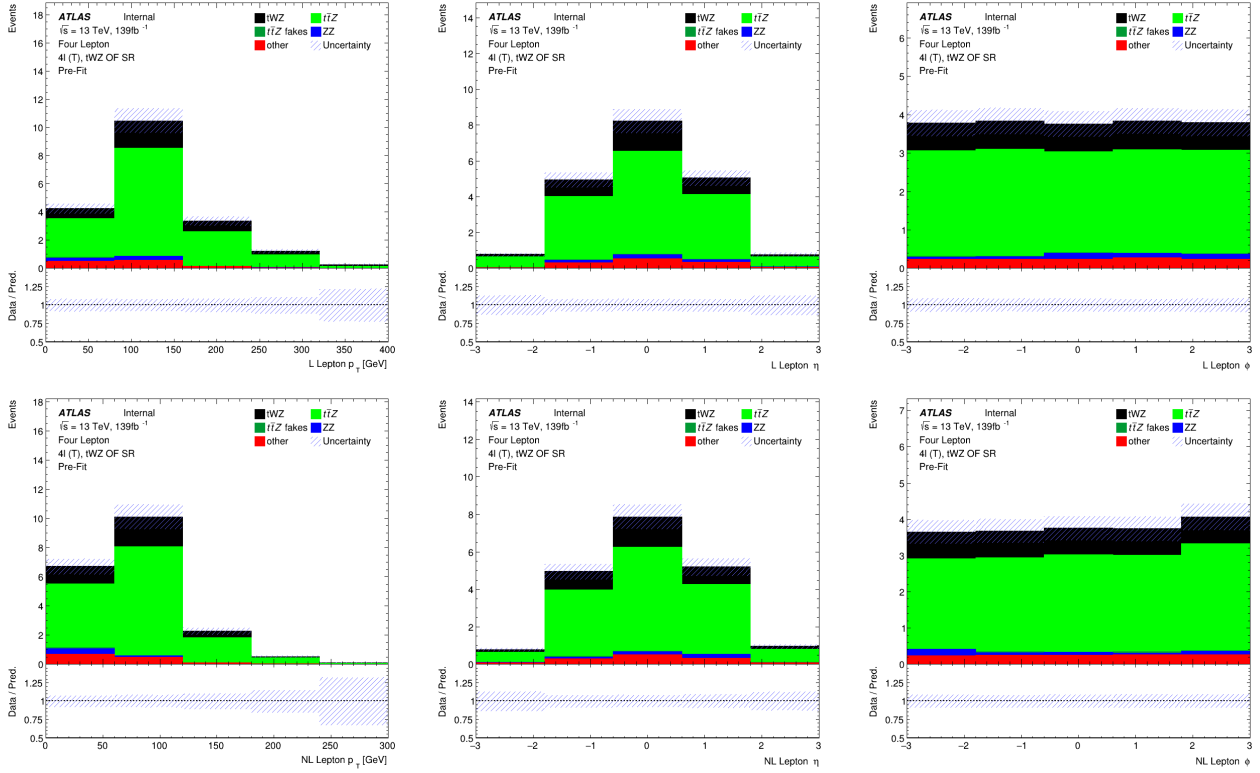


Figure 4.5: MC predictions for  $p_T$ ,  $\eta$  and  $\phi$  for leading (L) leptons (top row) and next-to-leading (NL) leptons (bottom row) in the  $tWZ$  OF SR region is shown.

In Figure 4.6 MC predictions for  $p_T$ ,  $\eta$  and  $\phi$  for leading (L) jets and next-to-leading (NL) jets in the  $tWZ$  OF SR region is shown.

In Figure 4.7 MC predictions for  $p_T$ ,  $\eta$  and  $\phi$  of the next-to-next-to-leading (NNL) jets,  $H_T$  (scalar sum of Jet  $p_T$ ) and the Number of jets in the  $tWZ$  OF SR region is shown.

In Figure 4.8 MC predictions for  $p_T$ ,  $\eta$  and  $\phi$  of the leading b-tagged jets, the scalar sum of b-tagged jet  $p_T$  and the Number of b-tagged jets in the  $tWZ$  OF SR region is shown.

### 4.5.2 $tWZ$ SF SR

In this section, pre-fit distributions of variables in the  $tWZ$  SF SR are shown. More pre-fit distributions for the  $tWZ$  SF SR are shown in the appendix (Section A.1.2).

In Figure A.14 MC predictions for  $p_T$ ,  $\eta$  and  $\phi$  for leading (L) leptons and next-to-leading (NL) leptons in the  $tWZ$  SF SR region is shown.

In Figure 4.10 MC predictions for  $p_T$ ,  $\eta$  and  $\phi$  for leading (L) jets and next-to-leading (NL) jets in the  $tWZ$  SF SR region is shown.

In Figure 4.11 MC predictions for  $p_T$ ,  $\eta$  and  $\phi$  of the next-to-next-to-leading (NNL) jets,  $H_T$  (scalar sum of Jet  $p_T$ ) and the Number of jets in the  $tWZ$  SF SR region is shown.

In Figure 4.12 MC predictions for  $p_T$ ,  $\eta$  and  $\phi$  of the leading b-tagged jets, the scalar sum of b-tagged jet  $p_T$  and the Number of b-tagged jets in the  $tWZ$  SF SR region is shown.

### 4.5.3 $t\bar{Z}$ CR

In this section, pre-fit distributions of variables in the  $t\bar{Z}$  CR are shown. More pre-fit distributions for the  $t\bar{Z}$  CR are shown in the appendix (Section A.1.3).

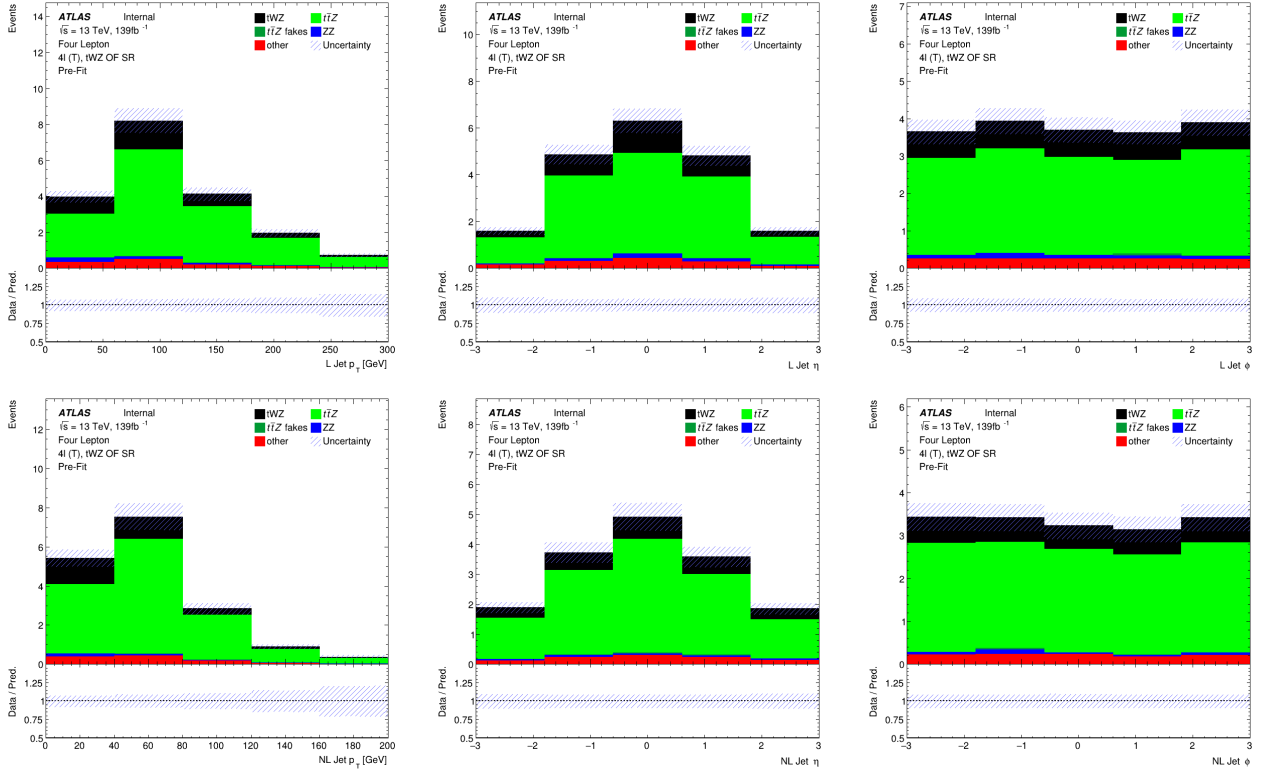


Figure 4.6: MC predictions for  $p_T$ ,  $\eta$  and  $\phi$  for leading (L) jets (top row) and next-to-leading (NL) jets (bottom row) in the  $tWZ$  OF SR region is shown.

In Figure A.27 MC predictions for  $p_T$ ,  $\eta$  and  $\phi$  for leading (L) leptons and next-to-leading (NL) leptons in the  $t\bar{t}Z$  CR region is shown.

In Figure 4.14 MC predictions for  $p_T$ ,  $\eta$  and  $\phi$  for leading (L) jets and next-to-leading (NL) jets in the  $t\bar{t}Z$  CR region is shown.

In Figure 4.15 MC predictions for  $p_T$ ,  $\eta$  and  $\phi$  of the next-to-next-to-leading (NNL) jets,  $H_T$  (scalar sum of Jet  $p_T$ ) and the Number of jets in the  $t\bar{t}Z$  CR region is shown.

In Figure 4.16 MC predictions for  $p_T$ ,  $\eta$  and  $\phi$  of the leading b-tagged jets, the scalar sum of b-tagged jet  $p_T$  and the Number of b-tagged jets in the  $t\bar{t}Z$  CR region is shown.

#### 4.5.4 $ZZb$ CR

In this section, pre-fit distributions of variables in the  $ZZb$  CR are shown. More pre-fit distributions for the  $ZZb$  CR are shown in the appendix (Section A.1.4).

In Figure A.41 MC predictions for  $p_T$ ,  $\eta$  and  $\phi$  for leading (L) leptons and next-to-leading (NL) leptons in the  $ZZb$  CR region is shown.

In Figure 4.18 MC predictions for  $p_T$ ,  $\eta$  and  $\phi$  for leading (L) jets and next-to-leading (NL) jets in the  $ZZb$  CR region is shown.

In Figure 4.19 MC predictions for  $p_T$ ,  $\eta$  and  $\phi$  of the next-to-next-to-leading (NNL) jets,  $H_T$  (scalar sum of Jet  $p_T$ ) and the Number of jets in the  $ZZb$  CR region is shown.

In Figure 4.20 MC predictions for  $p_T$ ,  $\eta$  and  $\phi$  of the leading b-tagged jets, the scalar sum of b-tagged jet  $p_T$  and the Number of b-tagged jets in the  $ZZb$  CR region is shown.

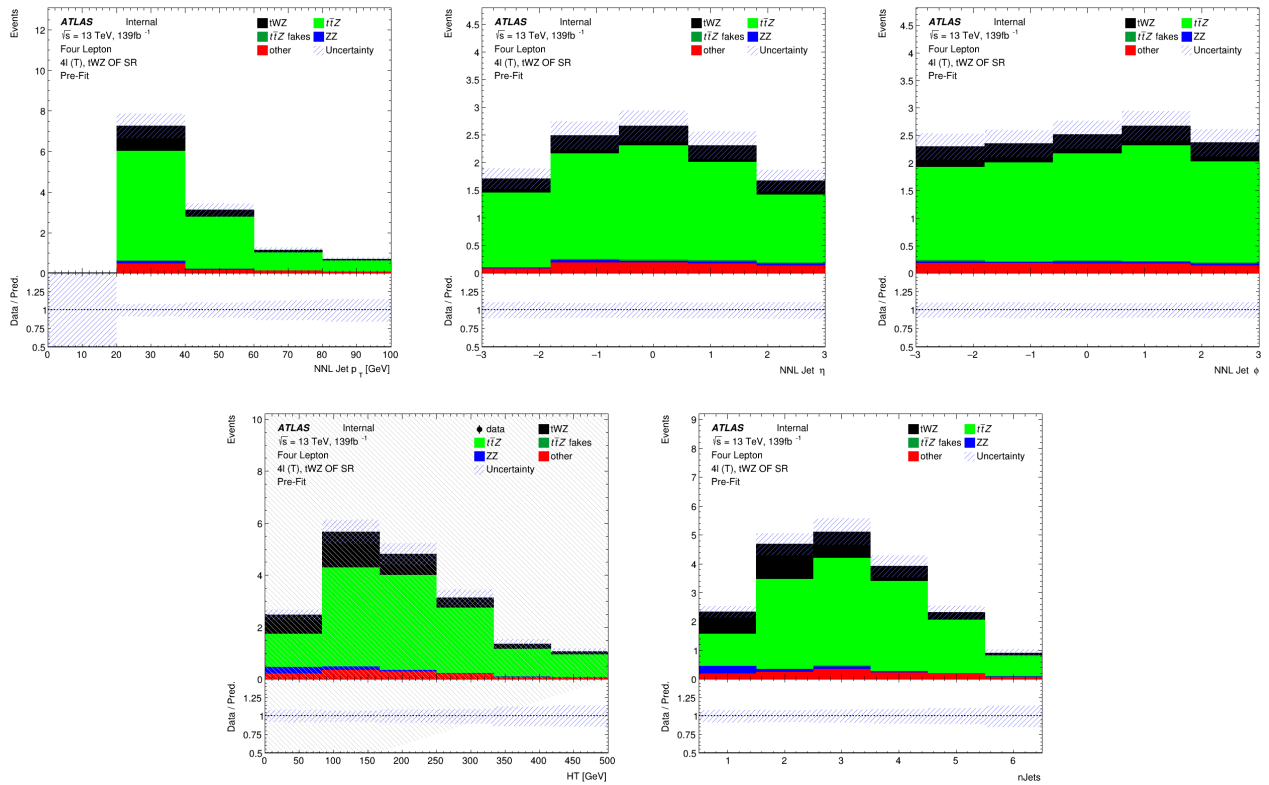


**Figure 4.7: Top row:** MC predictions for  $p_T$ ,  $\eta$  and  $\phi$  for next-to-next-to-leading (NNL) jets in the  $tWZ$  OF SR region is shown. **Bottom row:** MC predictions for  $H_T$  (scalar sum of Jet  $p_T$ ) (left) and the Number of jets (right) in the  $tWZ$  OF SR region is shown.

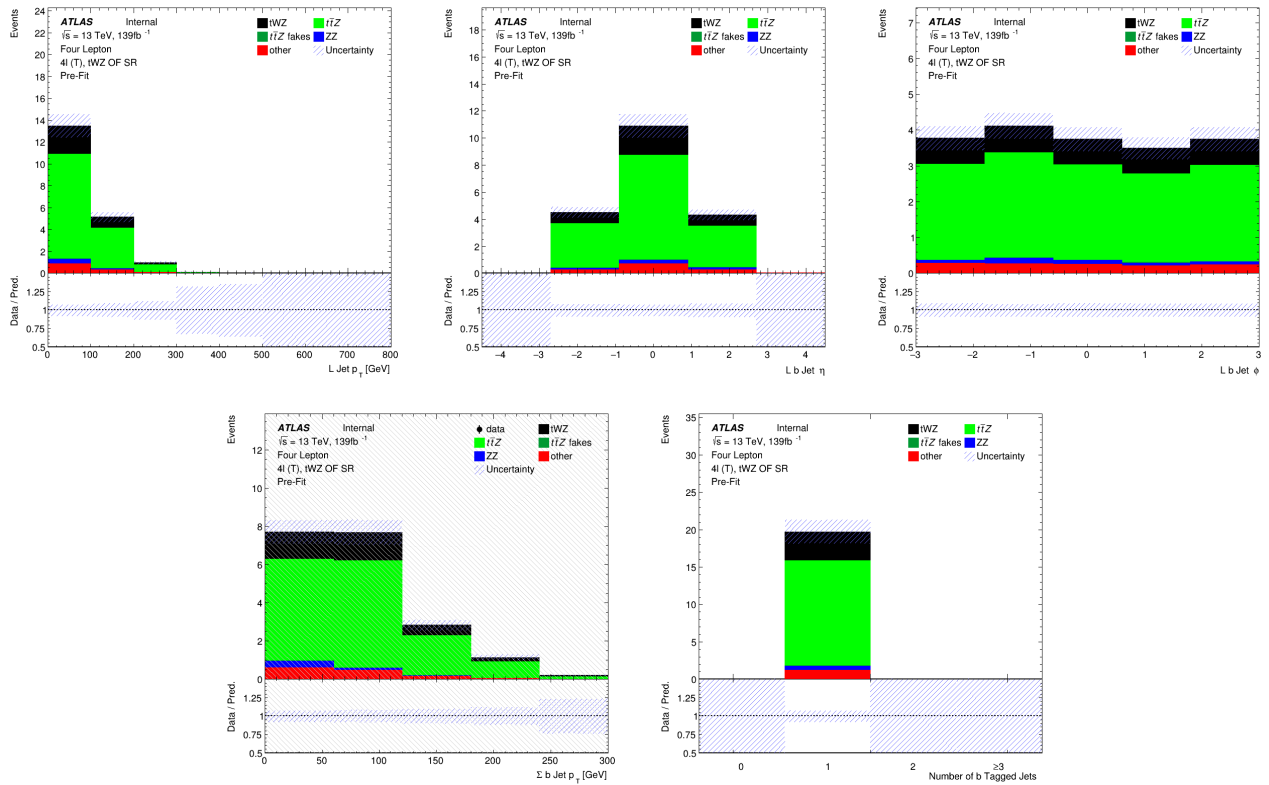


**Figure 4.8: Top row:** MC predictions for  $p_T$ ,  $\eta$  and  $\phi$  for leading b-tagged jets in the  $tWZ$  OF SR region is shown.  
**Bottom row:** MC predictions for the scalar sum of b-tagged jet  $p_T$  (left) and the Number of b-tagged jets (right) in the  $tWZ$  OF SR region is shown.

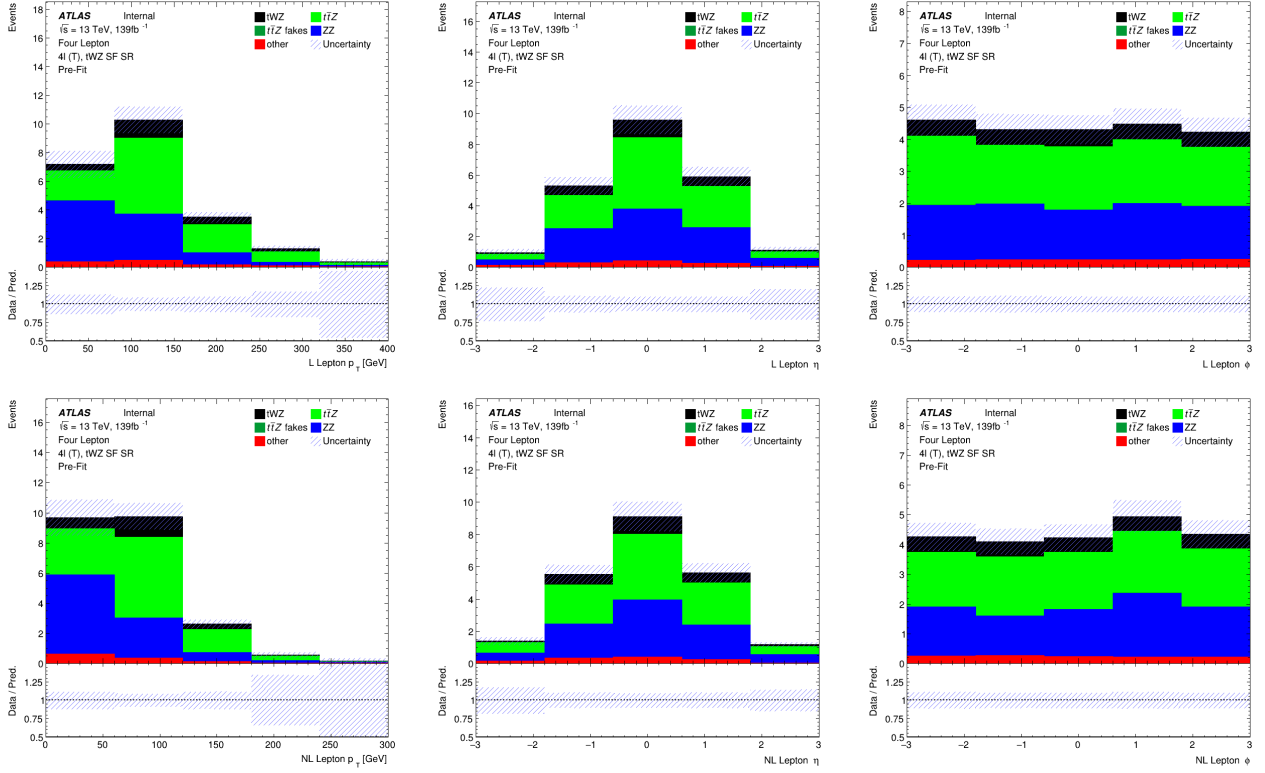


Figure 4.9: MC predictions for  $p_T$ ,  $\eta$  and  $\phi$  for leading (L) leptons (top row) and next-to-leading (NL) leptons (bottom row) in the  $tWZ$  SF SR region is shown.

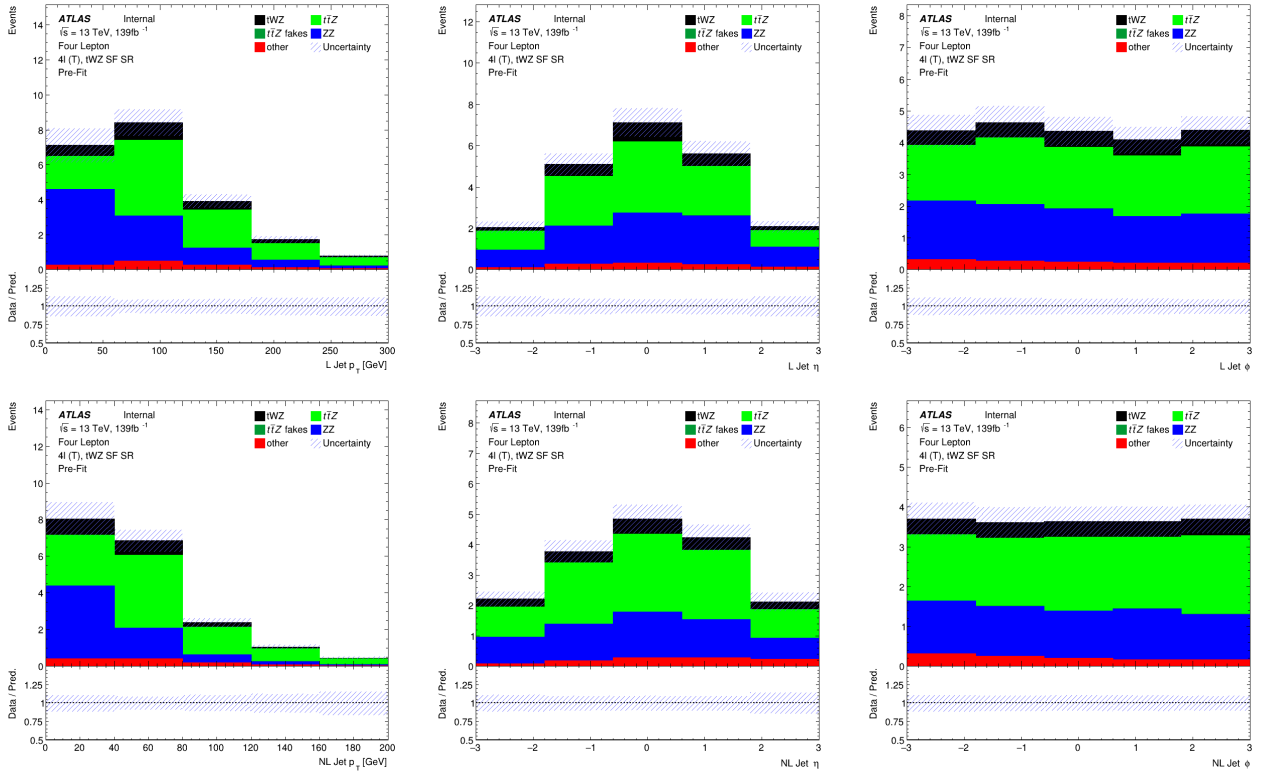
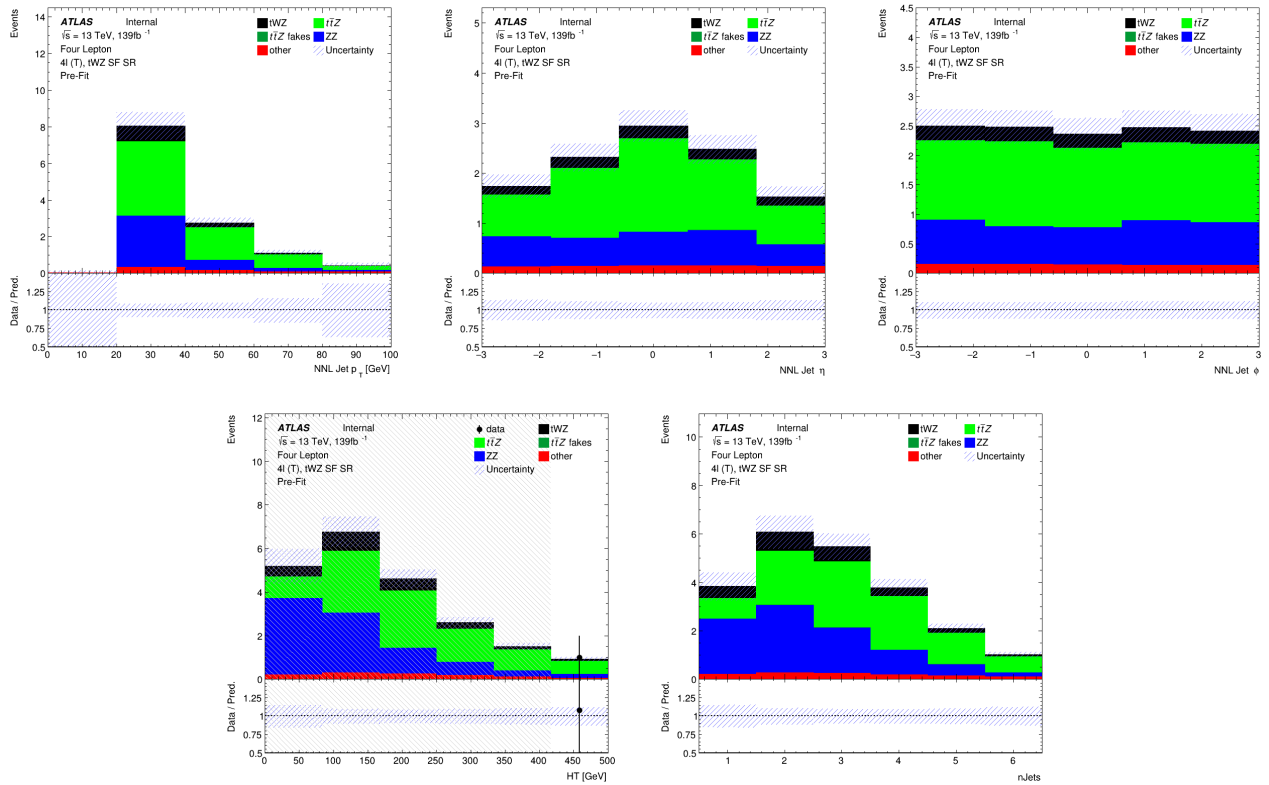


Figure 4.10: MC predictions for  $p_T$ ,  $\eta$  and  $\phi$  for leading (L) jets (top row) and next-to-leading (NL) jets (bottom row) in the  $tWZ$  SF SR region is shown.



**Figure 4.11:** **Top row:** MC predictions for  $p_T$ ,  $\eta$  and  $\phi$  for next-to-next-to-leading (NNL) jets in the  $tWZ$  SF SR region is shown. **Bottom row:** MC predictions for  $H_T$  (scalar sum of Jet  $p_T$ ) (left) and the Number of jets (right) in the  $tWZ$  SF SR region is shown.

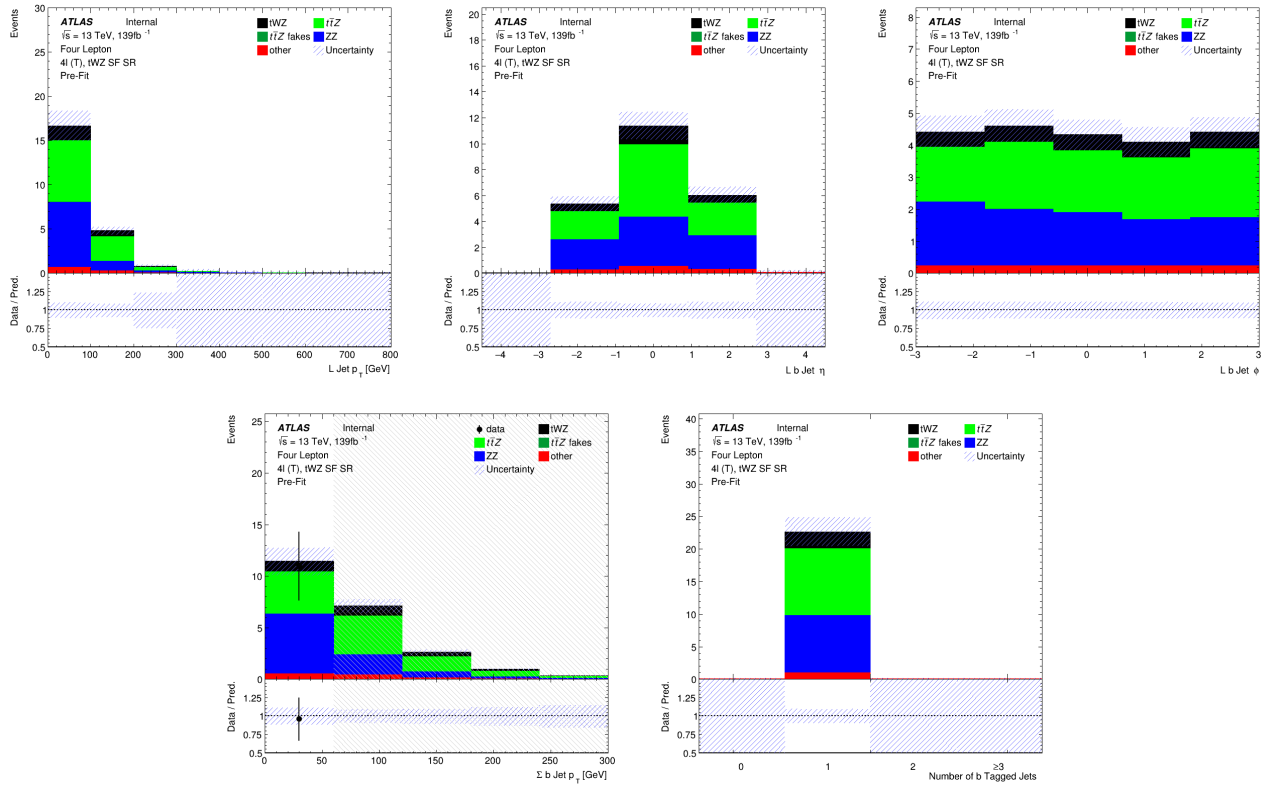


Figure 4.12: **Top row:** MC predictions for  $p_T$ ,  $\eta$  and  $\phi$  for leading b-tagged jets in the  $tWZ$  SF SR region is shown. **Bottom row:** MC predictions for the scalar sum of b-tagged jet  $p_T$  (left) and the Number of b-tagged jets (right) in the  $tWZ$  SF SR region is shown.

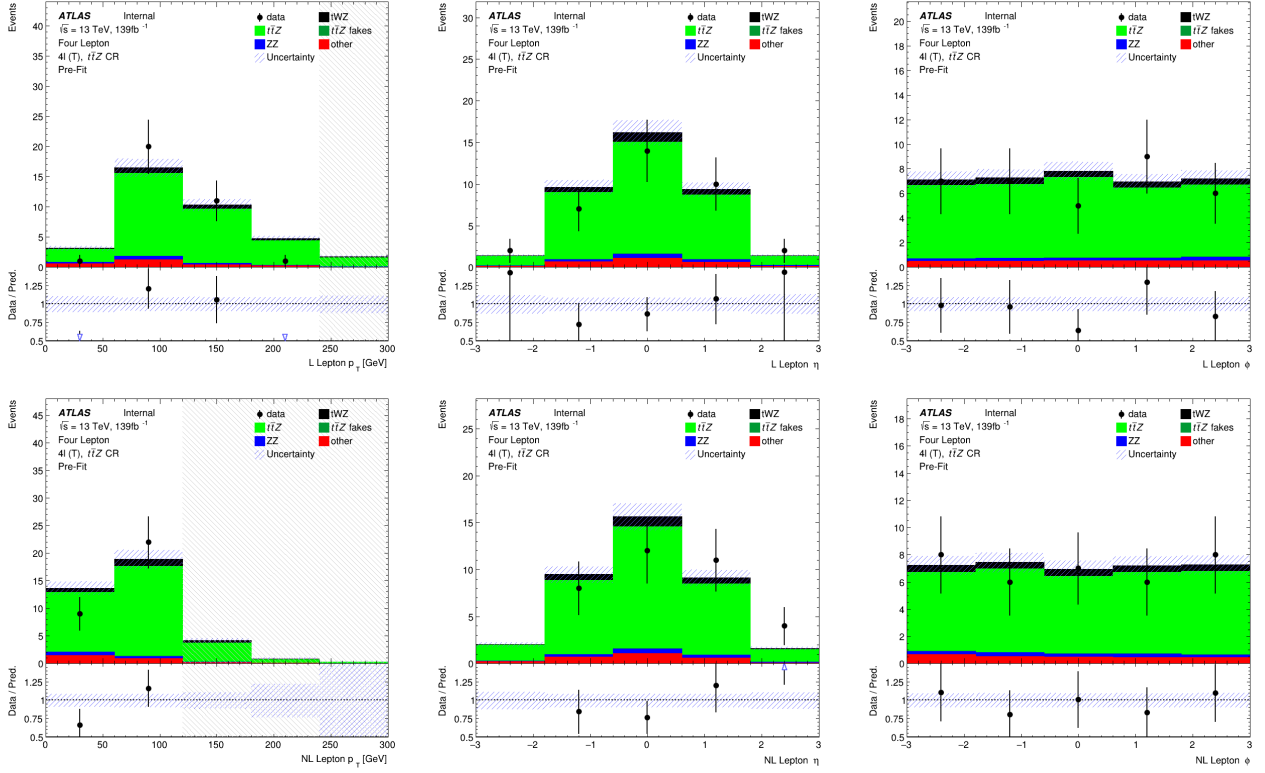


Figure 4.13: MC predictions for  $p_T$ ,  $\eta$  and  $\phi$  for leading (L) leptons (top row) and next-to-leading (NL) leptons (bottom row) in the  $t\bar{t}Z$  CR region is shown.

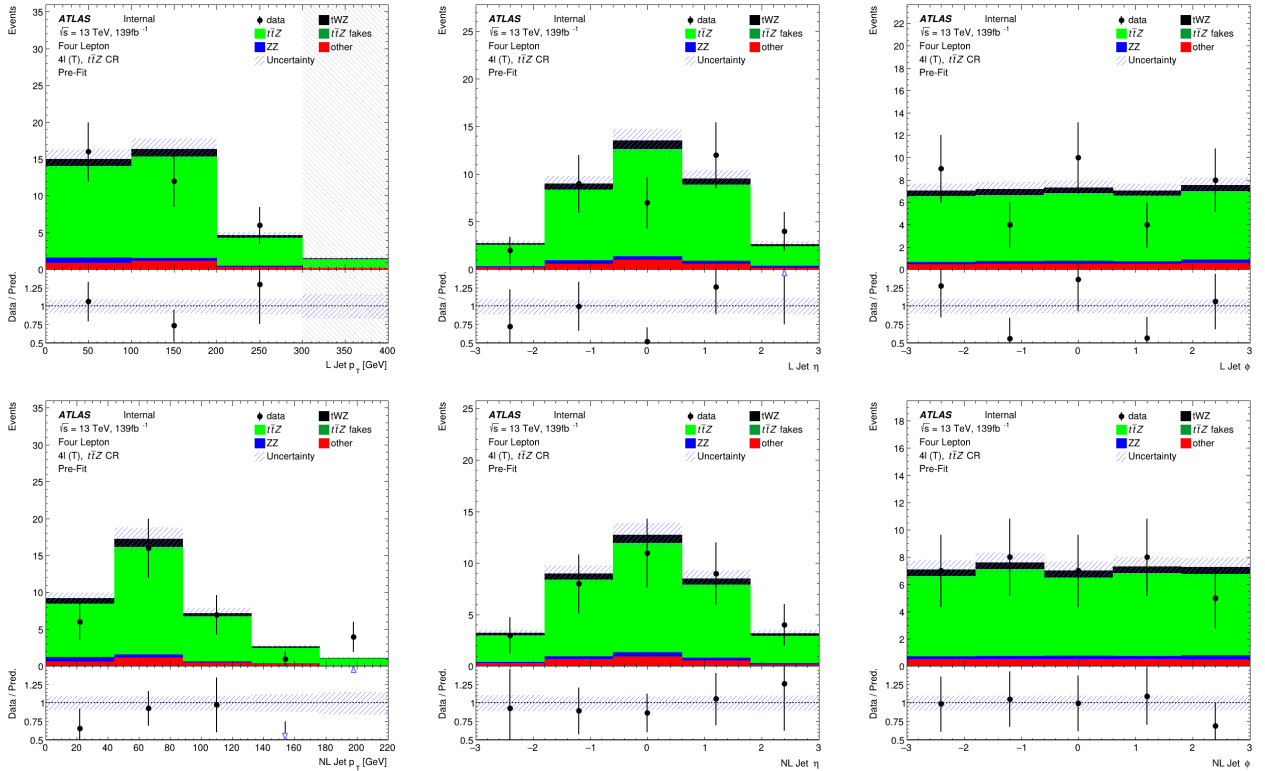


Figure 4.14: MC predictions for  $p_T$ ,  $\eta$  and  $\phi$  for leading (L) jets (top row) and next-to-leading (NL) jets (bottom row) in the  $t\bar{t}Z$  CR region is shown.

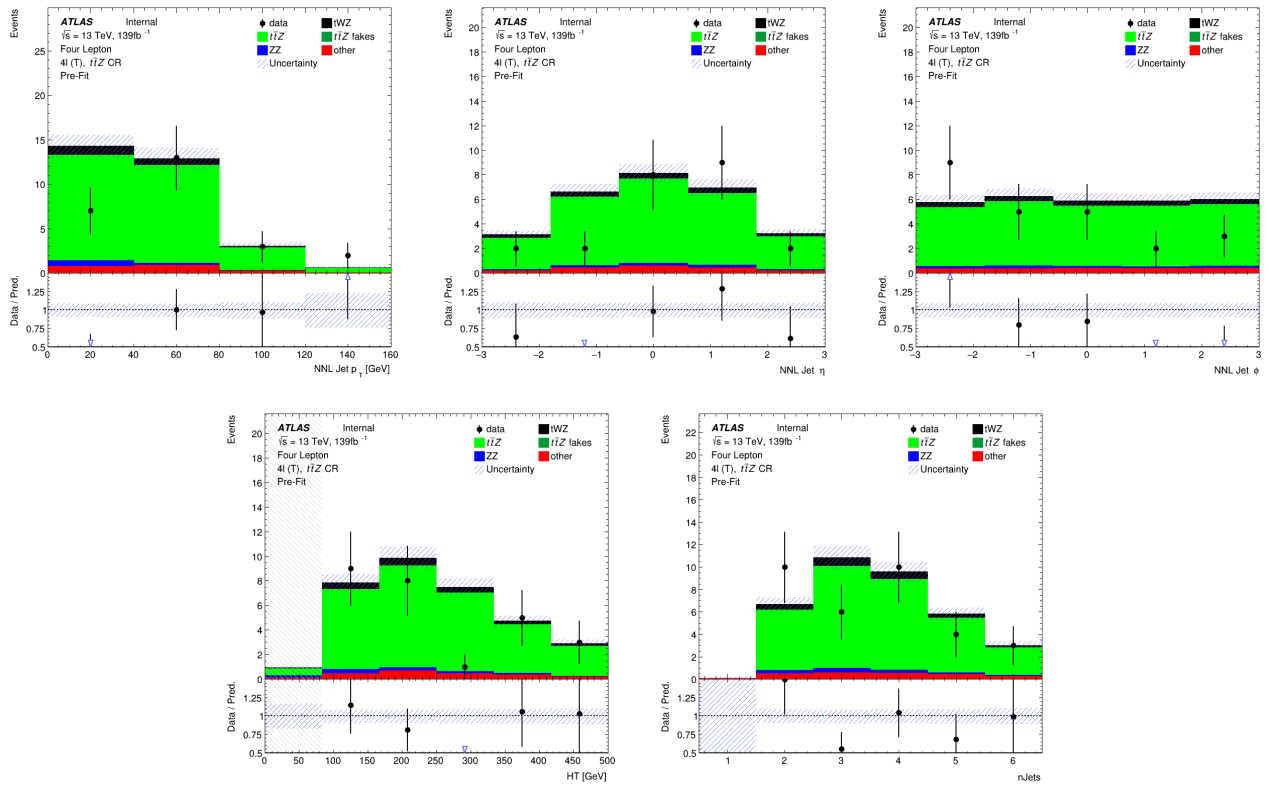


Figure 4.15: **Top row:** MC predictions for  $p_T$ ,  $\eta$  and  $\phi$  for next-to-next-to-leading (NNL) jets in the  $t\bar{t}Z$  CR region is shown. **Bottom row:** MC predictions for  $H_T$  (scalar sum of Jet  $p_T$ ) (left) and the Number of jets (right) in the  $t\bar{t}Z$  CR region is shown.

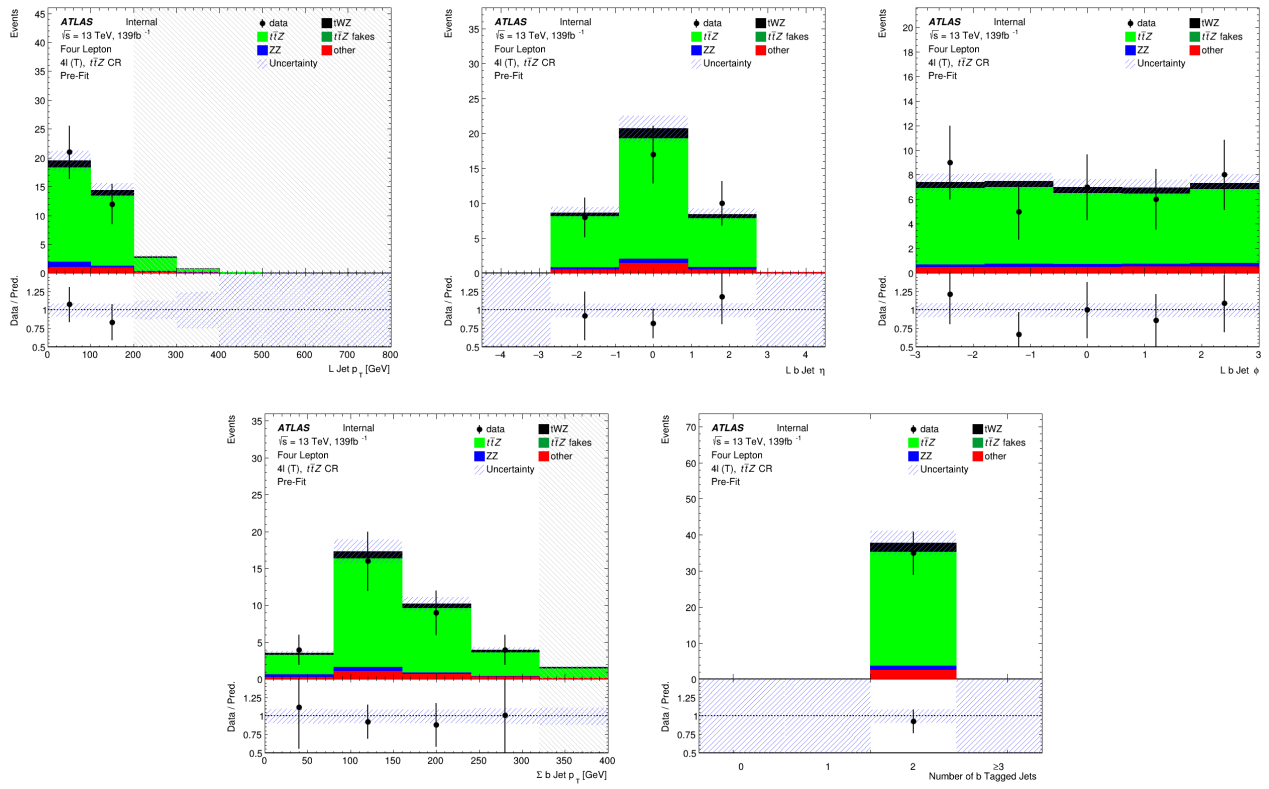


Figure 4.16: **Top row:** MC predictions for  $p_T$ ,  $\eta$  and  $\phi$  for leading b-tagged jets in the  $t\bar{t}Z$  CR region is shown. **Bottom row:** MC predictions for the scalar sum of b-tagged jet  $p_T$  (left) and the Number of b-tagged jets (right) in the  $t\bar{t}Z$  CR region is shown.

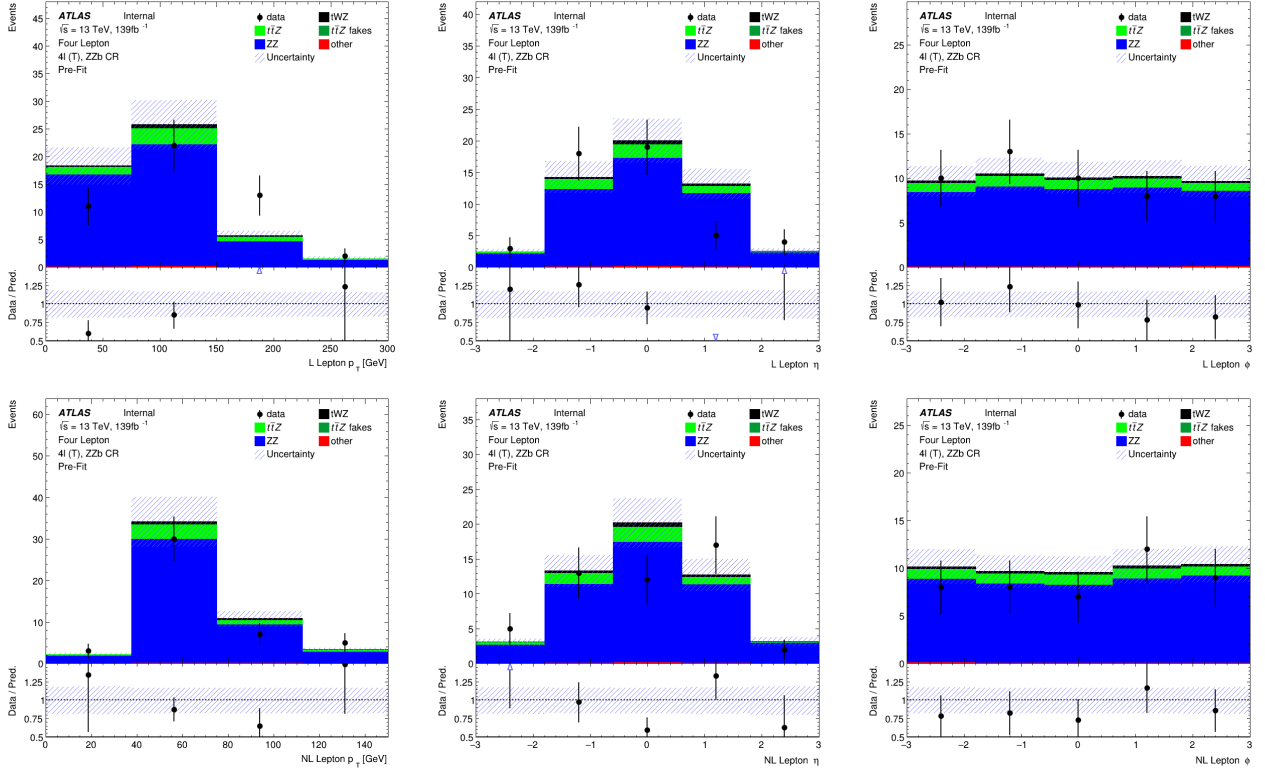


Figure 4.17: MC predictions for  $p_T$ ,  $\eta$  and  $\phi$  for leading (L) leptons (top row) and next-to-leading (NL) leptons (bottom row) in the  $ZZb$  CR region is shown.

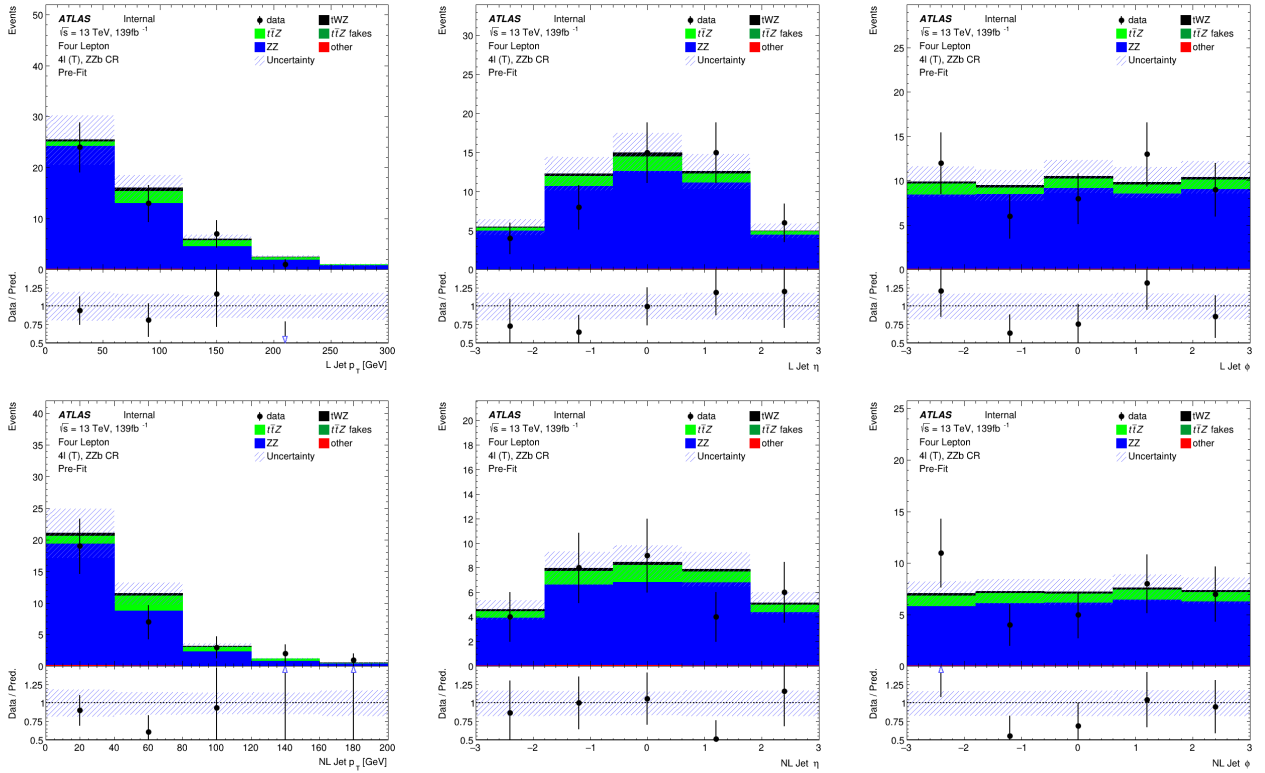


Figure 4.18: MC predictions for  $p_T$ ,  $\eta$  and  $\phi$  for leading (L) jets (top row) and next-to-leading (NL) jets (bottom row) in the  $ZZb$  CR region is shown.

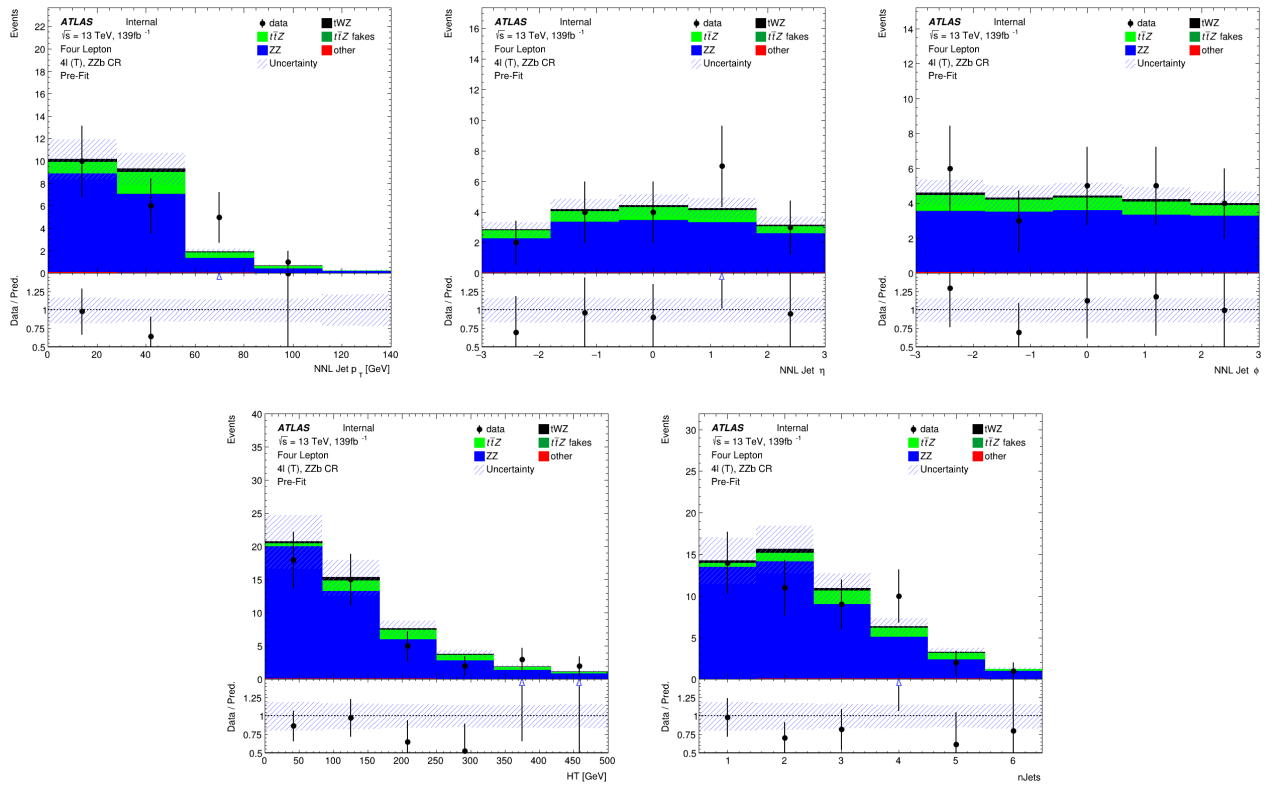


Figure 4.19: **Top row:** MC predictions for  $p_T$ ,  $\eta$  and  $\phi$  for next-to-next-to-leading (NNL) jets in the  $ZZb$  CR region is shown. **Bottom row:** MC predictions for  $H_T$  (scalar sum of Jet  $p_T$ ) (left) and the Number of jets (right) in the  $ZZb$  CR region is shown.

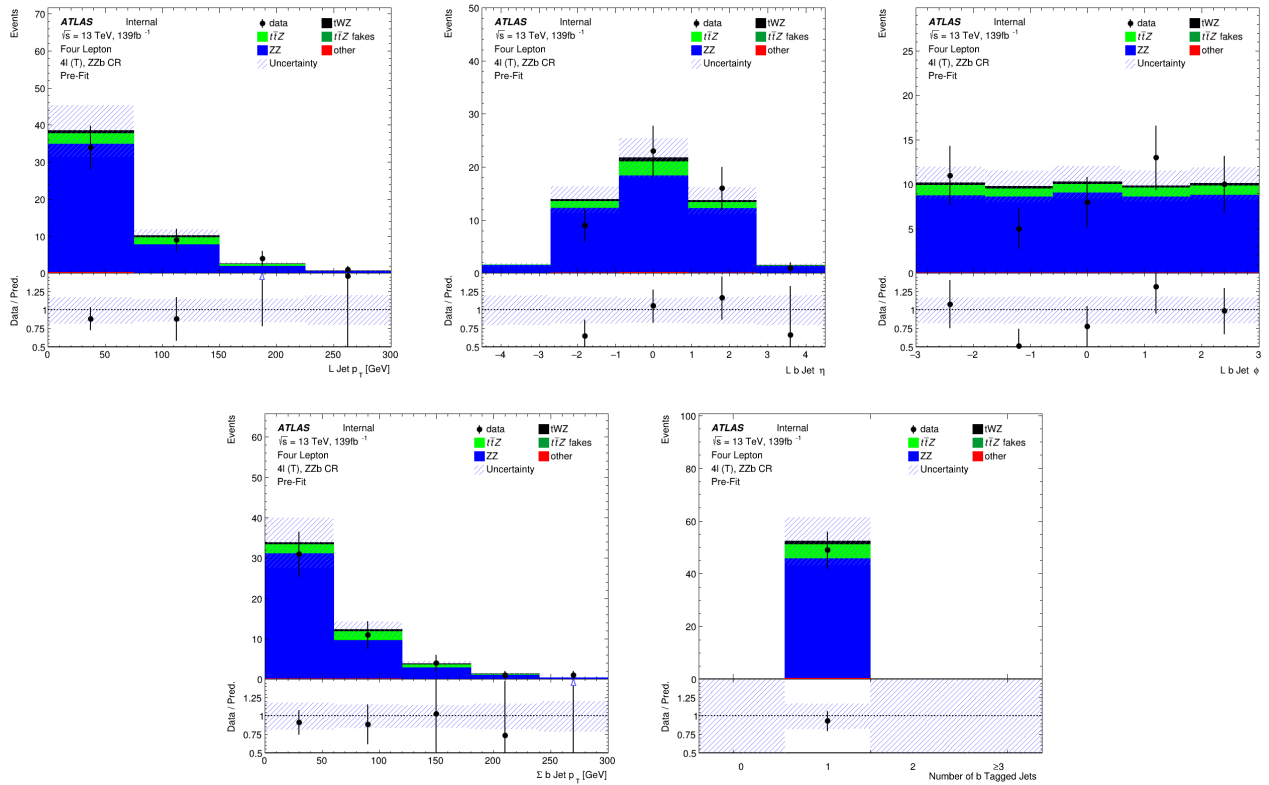


Figure 4.20: **Top row:** MC predictions for  $p_T$ ,  $\eta$  and  $\phi$  for leading b-tagged jets in the  $ZZb$  CR region is shown. **Bottom row:** MC predictions for the scalar sum of b-tagged jet  $p_T$  (left) and the Number of b-tagged jets (right) in the  $ZZb$  CR region is shown.

### 4.5.5 $(tWZ)_{\text{fake}}$ CR

In this section, pre-fit distributions of variables in the  $(tWZ)_{\text{fake}}$  CR are shown. More pre-fit distributions for the  $(tWZ)_{\text{fake}}$  CR are shown in the appendix (Section ??).

In Figure 4.21 MC predictions for  $p_T$ ,  $\eta$  and  $\phi$  for leading (L) leptons and next-to-leading (NL) leptons in the  $(tWZ)_{\text{fake}}$  CR region is shown.

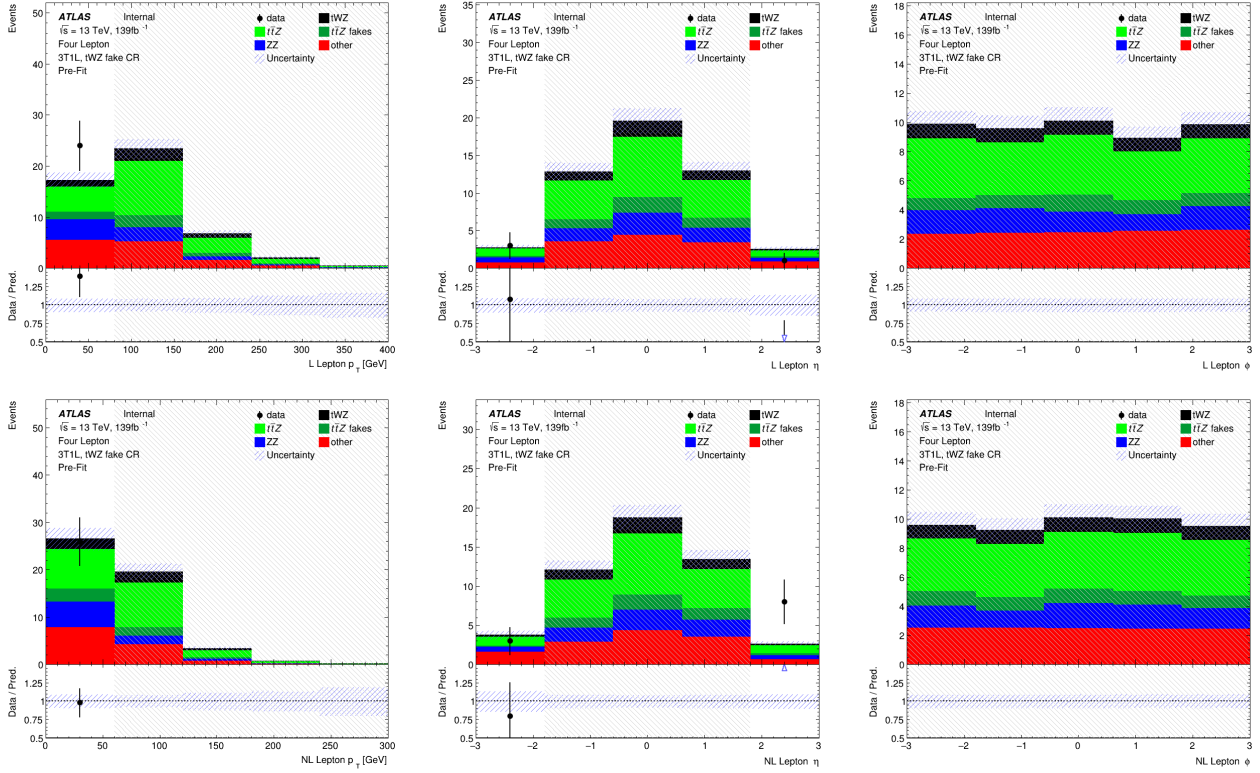


Figure 4.21: MC predictions for  $p_T$ ,  $\eta$  and  $\phi$  for leading (L) leptons (top row) and next-to-leading (NL) leptons (bottom row) in the  $(tWZ)_{\text{fake}}$  CR region is shown.

In Figure 4.22 MC predictions for  $p_T$ ,  $\eta$  and  $\phi$  for leading (L) jets and next-to-leading (NL) jets in the  $(tWZ)_{\text{fake}}$  CR region is shown.

In Figure 4.23 MC predictions for  $p_T$ ,  $\eta$  and  $\phi$  of the next-to-next-to-leading (NNL) jets,  $H_T$  (scalar sum of Jet  $p_T$ ) and the Number of jets in the  $(tWZ)_{\text{fake}}$  CR region is shown.

In Figure 4.24 MC predictions for  $p_T$ ,  $\eta$  and  $\phi$  of the leading b-tagged jets, the scalar sum of b-tagged jet  $p_T$  and the Number of b-tagged jets in the  $(tWZ)_{\text{fake}}$  CR region is shown.

Given the limited statistics which we are presented with in the tetralepton channel, we nevertheless observe relatively good agreement overall between data and MC.

## 4.6 Fake Lepton Estimation

Fake leptons are objects reconstructed as leptons, but do not correspond to the leptons which we are interested in our analysis. Fake leptons can be split up into two main categories, irreducible (prompt) fakes and reducible (non-prompt) fakes. Irreducible fakes are true leptons which do not come from the process of interest. Reducible fakes are objects which are mis-identified or incorrectly reconstructed as leptons. In the ATLAS detector, the probability for a fake to occur is very low.

We aim to estimate the fake lepton contribution in this analysis. We start off by noticing that  $t\bar{t}Z$  is our most

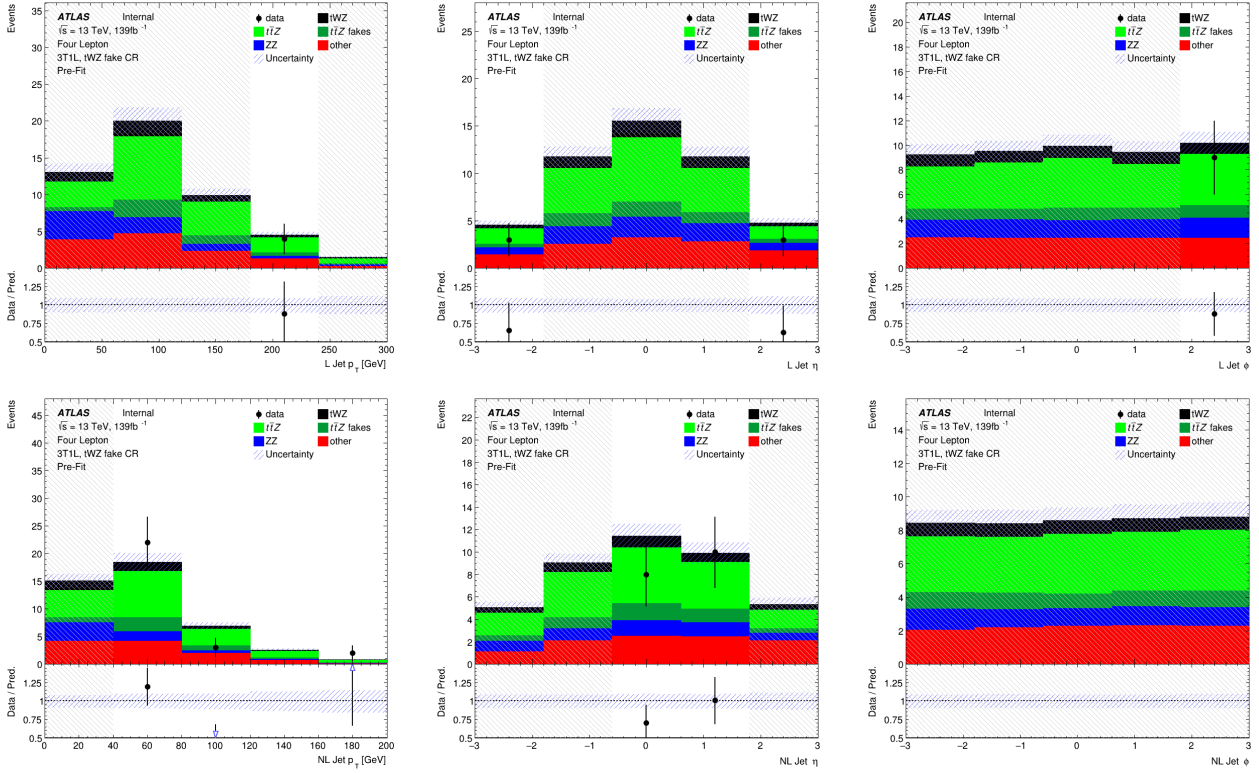


Figure 4.22: MC predictions for  $p_T$ ,  $\eta$  and  $\phi$  for leading (L) jets (top row) and next-to-leading (NL) jets (bottom row) in the ( $tWZ$ )<sub>fake</sub> CR region is shown.

dominant background ( $\sim 75\%$  of the total background contribution) and will therefore have the largest fake component compared to all other samples considered in the analysis. The fake lepton efficiency,  $\epsilon$ , can be written as  $\epsilon = \frac{N_{\text{fake}}^{\text{tight}}}{N_{\text{fake}}^{\text{loose}}}$ , where  $N_{\text{fake}}^{\text{tight}}$  is the number of fake leptons which pass the tight lepton selection (See Section 4.2.1) and  $N_{\text{fake}}^{\text{loose}}$  is the number of fake leptons which pass the loose lepton selection (See Section 4.2.1). The probability of one fake lepton to occur,  $P(\text{one fake } \ell)$ , is proportional to  $\epsilon$  and the probability for two fakes to occur is simply,  $P(\text{two fake } \ell) = (P(\text{one fake } \ell))^2 \propto \epsilon^2$ . Since  $\epsilon < 1$ , we have  $P(\text{one fake } \ell) \ll P(\text{two fake } \ell)$ . For this analysis we shall investigate the fake lepton component to the highest order and therefore we will consider the case where at least one fake lepton occurs in a  $t\bar{t}Z$  event.

Firstly, we split up the dominant  $t\bar{t}Z$  background into  $t\bar{t}Z$  and ( $t\bar{t}Z$ )<sub>fake</sub> components. Secondly, we define a ( $tWZ$ )<sub>fake</sub> CR (See Section 4.4) which is enhanced in fakes and aims to constrain the ( $t\bar{t}Z$ )<sub>fake</sub> background in the SR.

All events which contribute to the ( $t\bar{t}Z$ )<sub>fake</sub> background are determined by the IFF Truth Classifier [37]. The IFF Truth Classifier is a tool which aims to classify leptons based off their truth information. It uses the more general MCTruthClassifier [44] tool's output as input and returns one of the following lepton categories: Unknown, KnownUnknown (leptons which can (in principle) be classified, but the MCTruthClassifier fails to classify the lepton's truth type or origin), IsoElectron, ChargeFlipIsoElectron, PromptMuon, PromptPhotonConversion, ElectronFromMuon, TauDecay, BHadronDecay, CHadronDecay or LightFlavorDecay (More details [38]). Given these categories, we consider leptons classified as PromptPhotonConversion, BHadronDecay, CHadronDecay or LightFlavorDecay (i.e. a lepton originating from the decay of a  $b$ -Hadron,  $c$ -Hadron or light-flavour jet) to be fakes. We require that events which contribute to the ( $t\bar{t}Z$ )<sub>fake</sub> background are those where at least one lepton from the  $t\bar{t}Z$  sample are classified by the IFF Truth Classifier with one of the four aforementioned categories.

The ( $tWZ$ )<sub>fake</sub> CR aims to be as similar as possible to the  $tWZ$  SRs, but enhanced in fakes. This CR can then be used to constrain the normalisation of the ( $t\bar{t}Z$ )<sub>fake</sub> template. To ensure that this region is enhanced in fakes, we require that it contains 3 tight leptons and 1 loose lepton, since loose leptons are more likely to be fakes. By using the  $p_T$  of the loose lepton ( $p_T(\text{Loose Lepton})$ ) in this region as the variable used in the fit, the shape (and

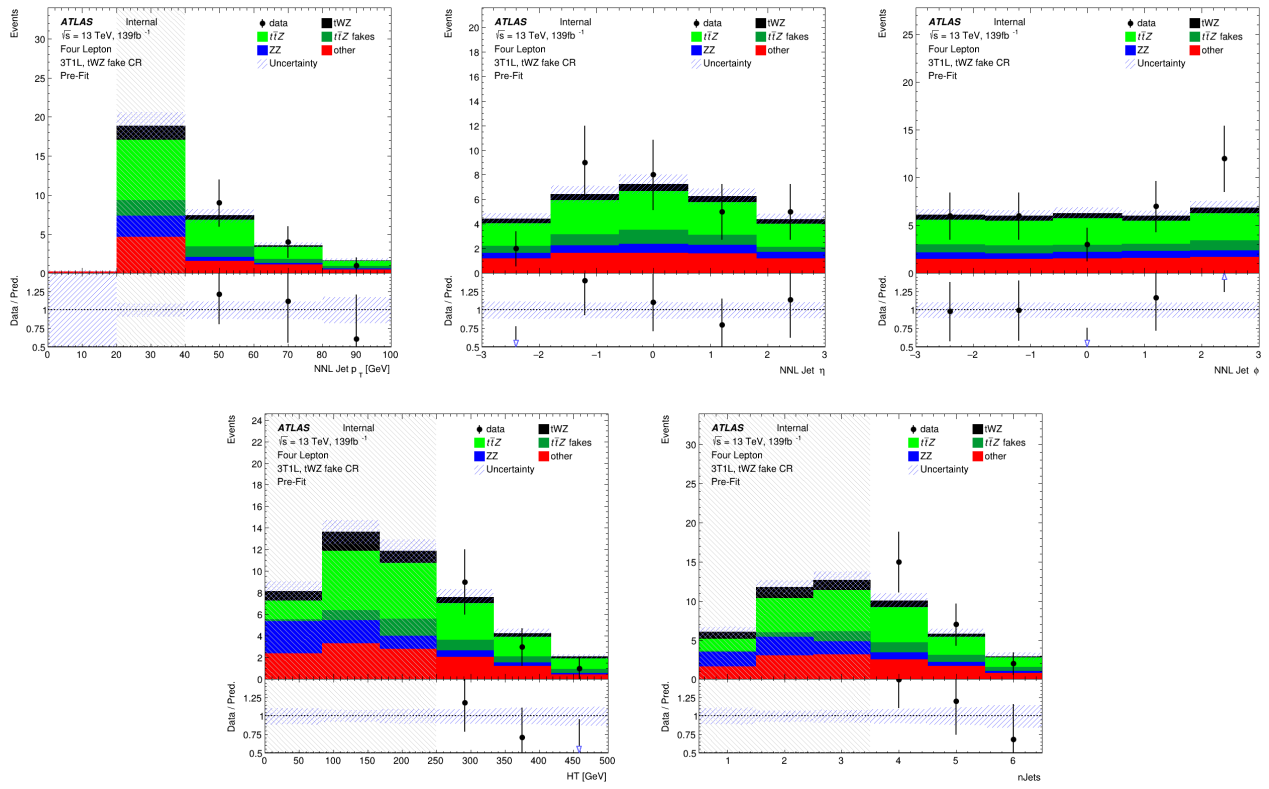


Figure 4.23: **Top row:** MC predictions for  $p_T$ ,  $\eta$  and  $\phi$  for next-to-next-to-leading (NNL) jets in the  $(tWZ)_{\text{fake}}$  CR region is shown. **Bottom row:** MC predictions for  $H_T$  (scalar sum of Jet  $p_T$ ) (left) and the Number of jets (right) in the  $(tWZ)_{\text{fake}}$  CR region is shown.

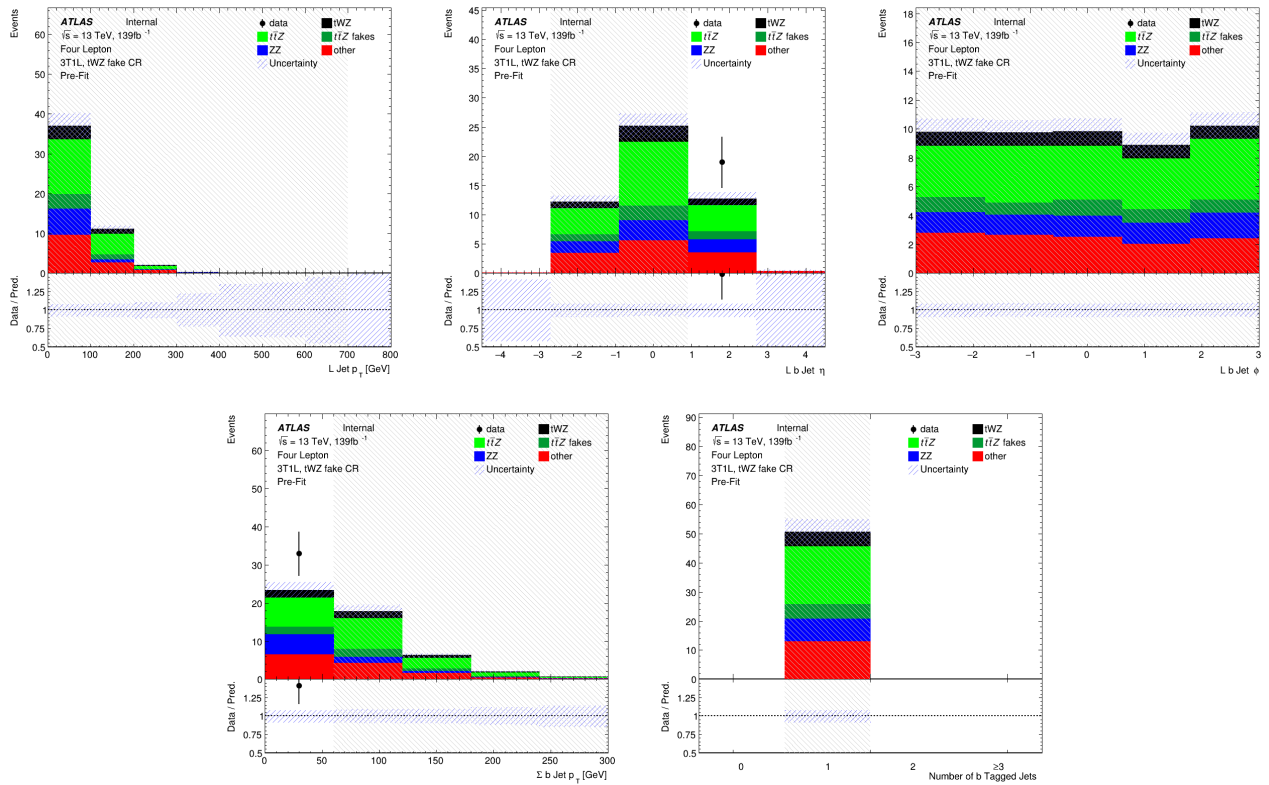


Figure 4.24: **Top row:** MC predictions for  $p_T$ ,  $\eta$  and  $\phi$  for leading b-tagged jets in the  $(tWZ)_{\text{fake}}$  CR region is shown. **Bottom row:** MC predictions for the scalar sum of b-tagged jet  $p_T$  (left) and the Number of b-tagged jets (right) in the  $(tWZ)_{\text{fake}}$  CR region is shown.

normalisation) of the  $(t\bar{t}Z)_{\text{fake}}$  template can be constrained.

In Figure 4.25, the number of leptons classified as fake, split up by their IFF Truth classification, in each region is shown.

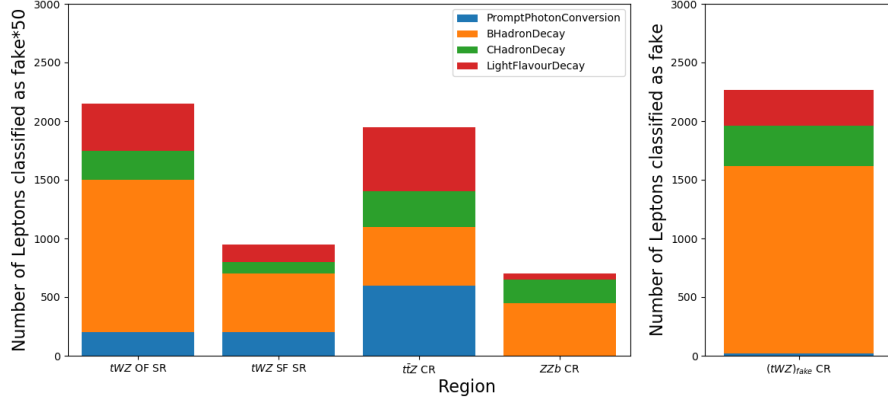


Figure 4.25: The number of leptons classified as fake, split up by their IFF Truth classification, in each region is shown. The left panel shows the number of leptons classified as fakes, scaled by a factor of 50, on the y-axis. The right panel shows the number of leptons classified as fakes (unscaled), on the y-axis. The different signal and control regions are shown on the x-axes of the left and right panels. The IFF truth classification of the leptons are shown in the legend and correspond to the different coloured stacked histograms.

Around 50 times more fake leptons pass our selection criteria for the  $(tWZ)_{\text{fake}}$  CR, compared to remaining four regions. This relative abundance of fake leptons present in the  $(tWZ)_{\text{fake}}$  CR further justifies our use of this region to constrain the fake lepton component.

In Figure 4.26, the relative dominance of the different classifications for fake leptons (classified by the IFF truth classified) in each region, is shown.

The majority of fake leptons which pass our selection criteria originate from the decay of  $b$ -hadrons, in all regions but the  $t\bar{t}Z$  CR. The smaller proportion of fake leptons originating from  $b$ -hadron decays in the  $t\bar{t}Z$  CR could possibly be due to statistical fluctuations resulting from the low number of fake leptons which pass our selection criteria in this region ( $\sim 40$  fake leptons).

In Figure 4.27, the amount of fake and real  $t\bar{t}Z$  events which pass our selection criteria, in each region, is shown. Around 20% of all  $t\bar{t}Z$  events are classified as fake events (having one or more of its leptons being classified as fake) in the  $(tWZ)_{\text{fake}}$  CR. The  $tWZ$  OF SR,  $tWZ$  SF SR,  $t\bar{t}Z$  CR and  $ZZb$  CR have less than 1% of their total  $t\bar{t}Z$  events being fake. The non-negligible amount of fake  $t\bar{t}Z$  events present in the  $(tWZ)_{\text{fake}}$  CR, allows the  $t\bar{t}Z$  fake background to be constrained by the  $(tWZ)_{\text{fake}}$  CR.

## 4.7 Machine Learning Techniques

Now that we have our baseline selections applied and our regions defined, we implement two Boosted Decision Trees (BDT) in order to discriminate between  $tWZ$  and our most prominent background process,  $t\bar{t}Z$  and  $ZZ$ . We chose to use a BDT, as opposed to another ML algorithm, since they are very stable and perform well with minimal/no optimisation or tweaking of the hyper parameters. A multi-layered sequential neural network was tried, however, it was out-performed by a BDT. More specifically, Scikit-Learn's `GradientBoostingClassifier` was used.

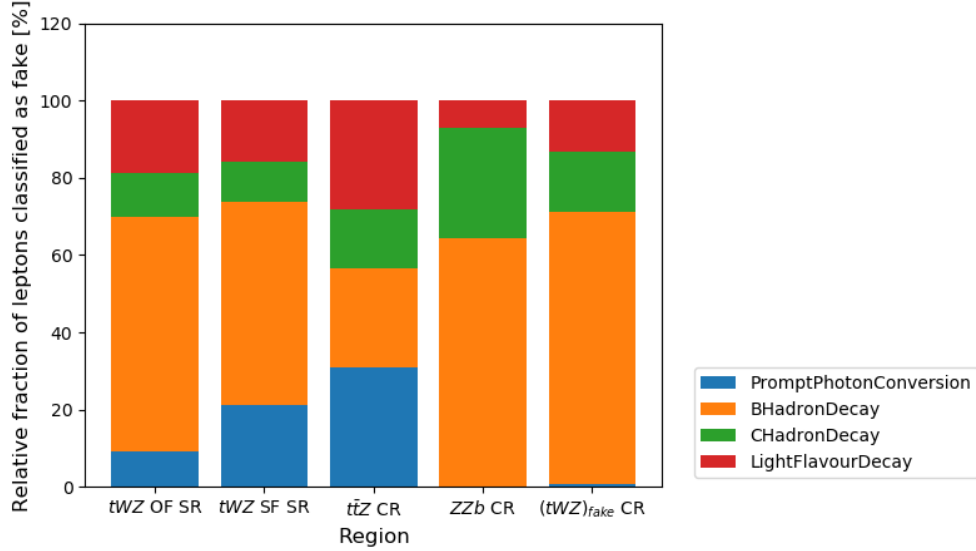


Figure 4.26: The relative dominance of the different classifications for fake leptons (classified by the IFF truth classified) in each region, is shown. The relative dominance of leptons classified as fakes, as a fraction of the total number of fake leptons (in each region), is shown on the y-axis. The different signal and control regions are shown on the x-axis. The IFF truth classification of the leptons are shown in the legend and correspond to the different coloured stacked histograms.

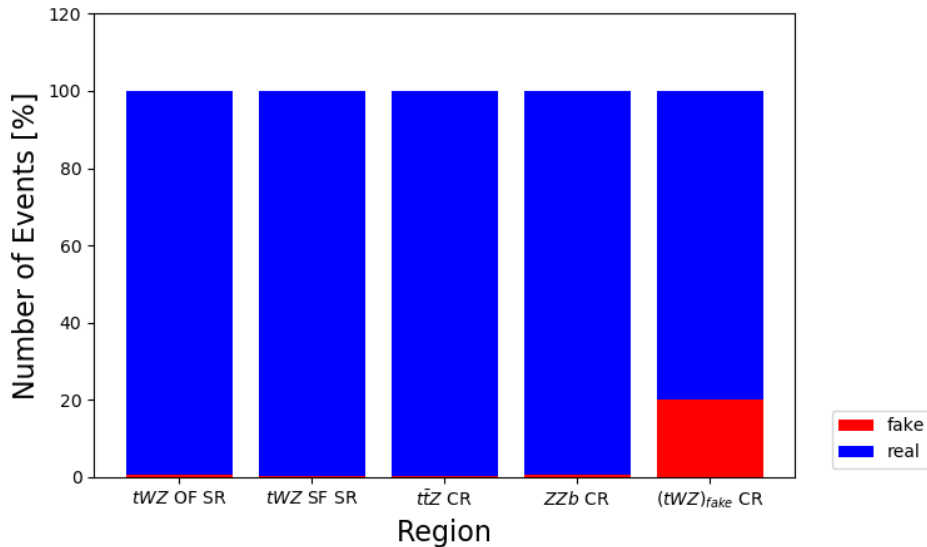


Figure 4.27: The percentage of fake and real  $t\bar{t}Z$  events which pass our selection criteria, in each region, is shown. The relative number of fake and real events (in % of the total number of events in the nominal and fake  $t\bar{t}Z$  background samples) is shown on the y-axis. The different signal and control regions are shown on the x-axis. The blue and red histograms represent the percentage of real and fake events (out of the total number of events in the nominal and fake  $t\bar{t}Z$  background samples), respectively.

Two different BDTs were used, the first aims to discriminate between  $tWZ$  events and its major backgrounds,  $t\bar{t}Z$  and  $ZZ$ . The second aims to discriminate between  $\ell b$  systems which originate from the decay of a top quark ( $t \rightarrow W(\rightarrow \ell\nu)b$ ) and those which do not. We refer to these two BDTs as an **event-level** and an **object-level** classifier respectively. The discriminator output from the object-level BDT can be converted to a variable which can then be used as input to the event-level BDT.

### 4.7.1 Object-level BDT

The object-level BDT was trained on a  $t\bar{t}$  sample with a baseline selection of exactly 1 tight lepton with  $p_T > 28$  GeV. Additionally, jets in this sample are required to have  $p_T > 20$  GeV.  $b$ -tagged jets are identified by the 77% DL1r working point. These baseline selections were chosen to mimic those used in the event selection of the analysis (outlined in Table 4.3). We opted to use this disjoint  $t\bar{t}$  sample as to avoid resorting to use our MC samples used in the rest of the analysis which is heavily limited on statistics, therefore maximizing the amount of MC statistics used in the fitting procedure and the training of the event-level BDT.

The signal class is defined to consist of reconstructed  $\ell b$  systems (defined as the sum of the 4-vectors of the lepton and  $b$ -jet) coming from top quarks which are well matched to their truth counterparts. In particular, we require that  $\Delta R$  between the reconstructed and truth  $\ell b$  system is less than 0.05. We additionally require that the reconstructed lepton and the truth top have charges with the same sign (since  $t \rightarrow b\ell^+\bar{\nu}_\ell$  and  $\bar{t} \rightarrow \bar{b}\ell^-\nu_\ell$ ). The background class is defined to consist of all reconstructed  $\ell b$  systems which fail to pass the criteria for  $\ell b$  systems which are labelled as signal. These definitions for the signal and background classes ensure that the signal class consists of mostly  $\ell b$  systems originating from tops and the background class consists of mostly  $\ell b$  systems which do not originate from a top decay.

Different observables corresponding to an  $\ell b$  system were used as input to training. The optimum values for the hyper-parameters used were determined by training the BDT with a range of different values for the hyper-parameters and choosing the set of values which maximized the mean accuracy (based off 5 fold kfold cross-validation). This method is more commonly referred to as hyper-parameter optimisation or tuning. After hyper-parameter optimisation, the mean accuracy of each fold increased from 0.76 to 0.77 ( $\sim 1\%$  increase). Input features can be assigned a score called *variable importance*, based on their usefulness on predicting a target variable (in this case, a signal or background event). The variable importance for any given variable was obtained by computing the mean accuracy of the model, removing the variable from training, retraining the model and computing the mean accuracy of this new model. The difference between mean accuracies of the unaltered model and the retrained model (after removal of the variable) gives us the variable importance of the variable of interest. This method returns positive values for variables which increase the mean accuracy of the model and negative values for variables which decrease the mean accuracy of the model. Variables with negative variable importances were completely removed from training.

In Table 4.6, the variables used in training the object-level BDT are shown.

Observable	Description
$m(\ell b)$	Invariant mass of the $\ell b$ system
$p_T(\ell b)$	$p_T$ of the $\ell b$ system
$\Delta\eta(\ell, b)$	$\Delta\eta$ between the $\ell$ and $b$ -tagged jet
$\Delta\phi(\ell, b)$	$\Delta\phi$ between the $\ell$ and $b$ -tagged jet
$\Delta R(\ell, b)$	$\Delta R$ between the $\ell$ and $b$ -tagged jet

Table 4.6: A list of the observables used in the object-level BDT, ordered by importance (descending, top to bottom) is shown.

In Figure 4.28, normalised distributions of the signal and background classes for the training set of all variables used in the object-level BDT are show.

Overall the BDT input variables show a large amount of discrimination.

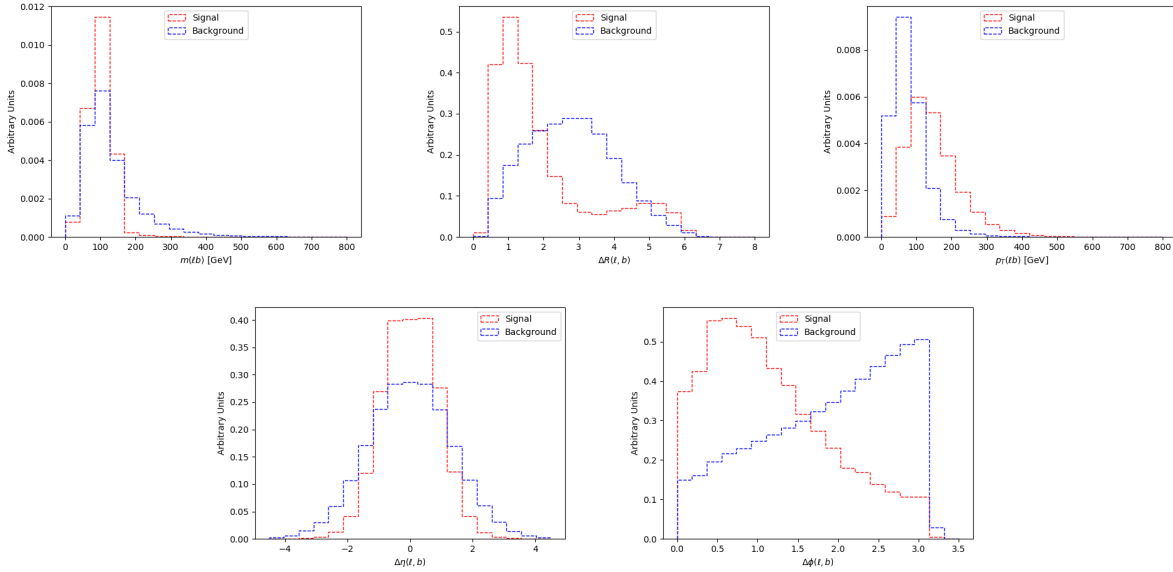


Figure 4.28: Normalised distributions of the signal and background classes for the training set of all variables used in the object-level BDT (ordered from top left to bottom right via decreasing importance) are shown. The red and blue dotted lined histograms represent the signal and background classes events (normalised to an area of 1), respectively. The variable used in training is shown on the x-axis. The y-axis shows the relative number of events for the signal and background classes (in arbitrary units). **From top left to bottom right:** Invariant mass of the  $\ell b$  system.  $\Delta R$  between the  $\ell$  and  $b$ -tagged jet. The  $p_T$  of the  $\ell b$  system.  $\Delta\eta$  between the  $\ell$  and  $b$ -tagged jet.  $\Delta\phi$  between the  $\ell$  and  $b$ -tagged jet.

We can check the modelling of the input variables to the object-level BDT by studying the agreement between data and simulation in the  $t\bar{t}Z$  CR. In Figure 4.29, MC predictions for the input variables to the object-level BDT in the  $t\bar{t}Z$  CR are shown.

Overall, there is good agreement between data and simulation for the input variables to the object-level BDT in the  $t\bar{t}Z$  CR. This suggests that the input variables to the object-level BDT are well-modelled and are reasonable to include as inputs to the object-level BDT.

A final check can be done to study the similarity of the  $\ell b$  systems present in the alternative  $t\bar{t}$  sample which we use for training the object-level BDT, and the  $\ell b$  systems which we aim to identify using the object-level BDT. More specifically, we want to ensure that the  $\ell b$  systems in the alternative  $t\bar{t}$  sample are similar enough to those in the  $tWZ$  and  $t\bar{t}Z$  samples (see Table 4.1). In Figure 4.30, normalised distributions of input variables to the object-level BDT in the alternative  $t\bar{t}$ ,  $tWZ$  and  $t\bar{t}Z$  samples, are shown.

The distributions of the input variables to the object-level classifier, for the three samples, are similar and show no large deviations between one another. This tells us that the  $\ell b$  systems which we use in training are similar enough to those we aim to identify using the classifier. The use of the alternative  $t\bar{t}$  sample for training the object-level classifier is therefore sufficient for this analysis.

In Table 4.7, the hyper-parameters used in the object-level BDT is shown.

The number of events used in training for the signal and background classes were 49871 and 384152 respectively. Imbalanced datasets can cause ML classifiers to ignore small classes while concentrating on classifying large classes more accurately, which may result in the trained classifier performing sub-optimally. In order to correct this dataset imbalance, we ensure that the relative weighting of each event is such that the sum of the signal weights is equal to the sum of the background weights. In Figure 4.31 the normalised histograms of the training and test sets (extracted from fold 5 from a 5 fold kfold cross validation) for signal and background is shown.

We can see that the shapes of the training and test sets for both signal and background are very similar. This is a good indicator that no over-training occurred. Another over-training check is performed using 5 fold kfold

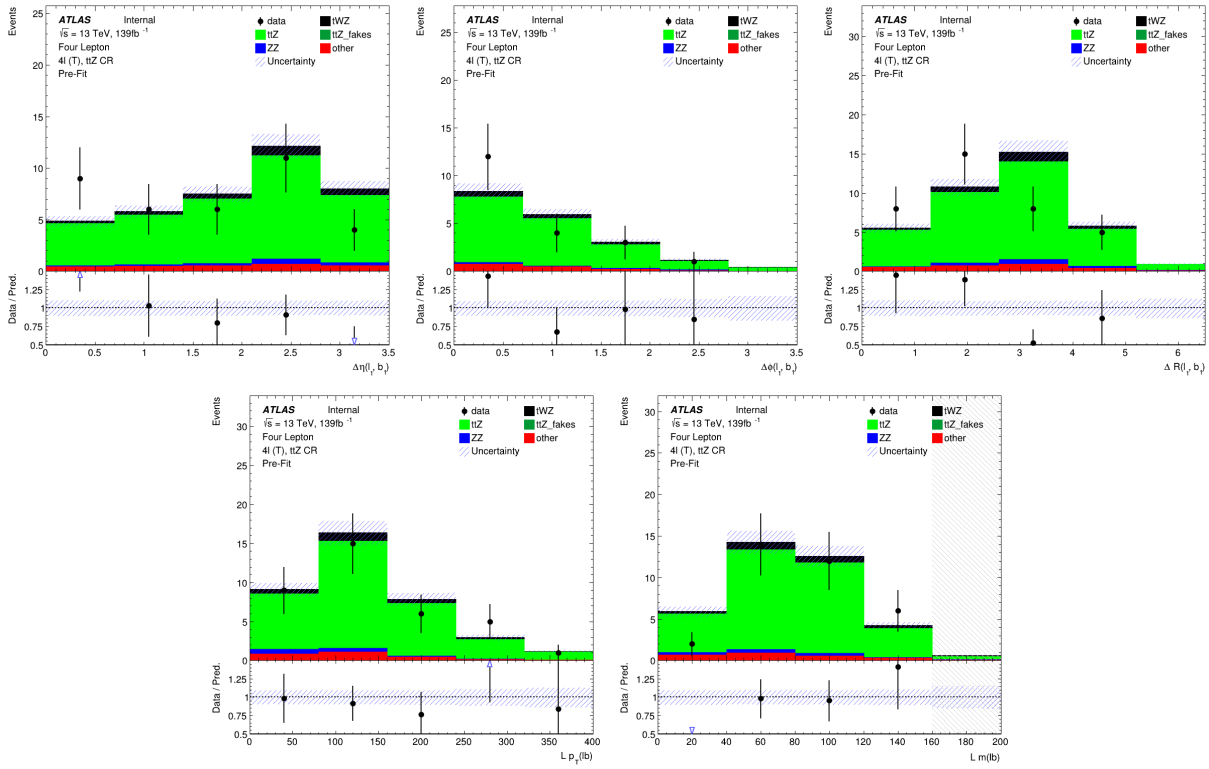


Figure 4.29: Pre-fit distributions of variables used as input to the object-level BDT (ordered from top left to bottom right via decreasing importance), in the  $t\bar{t}Z$  CR, are shown. The data is given by the black points and the MC predictions for each process are given by the histograms. The vertical lines on the data points represent the total uncertainty in the data and the blue diagonal lined bands represent the total MC uncertainty. The lower panel in each plot shows the ratios of the data to the theoretical predictions. Bins with a  $\frac{\text{signal}}{\text{background}}$  yield greater than 0.1 are kept blinded. Blinded bins are shaded with black diagonal lines and their data points are omitted. **From top left to bottom right:**  $\Delta\eta$  between the lepton and  $b$ -jet of the leading  $\ell b$  system.  $\Delta\phi$  between the lepton and  $b$ -jet of the leading  $\ell b$  system.  $\Delta R$  between the lepton and  $b$ -jet of the leading  $\ell b$  system.  $p_T$  of the leading  $\ell b$  system. Mass of the leading  $\ell b$  system.

Hyper-parameter	Value	Description
loss	deviance	The loss function to be optimised
criterion	friedman_mse	The function used to measure the quality of a split
n_estimators	200	The number of boosting stages to perform
learning_rate	0.1	The step size at each iteration during optimisation
max_depth	6	The maximum depth of the individual regression estimators
min_samples_split	2	The minimum number of samples (events) required to split an internal node
min_samples_leaf	1	The minimum number of samples (events) required to be at a leaf node
validation_fraction	0.1	The proportion of training data to set aside as validation set for early stopping
n_iter_no_change	20	Training terminates when the validation score (determined by the validation set) does not improve in all of the previous

Table 4.7: A list of the hyper-parameters used in the object-level BDT is shown. Hyperparameters not listed in this table use the default values as stated in the Scikit-learn Documentation[52].

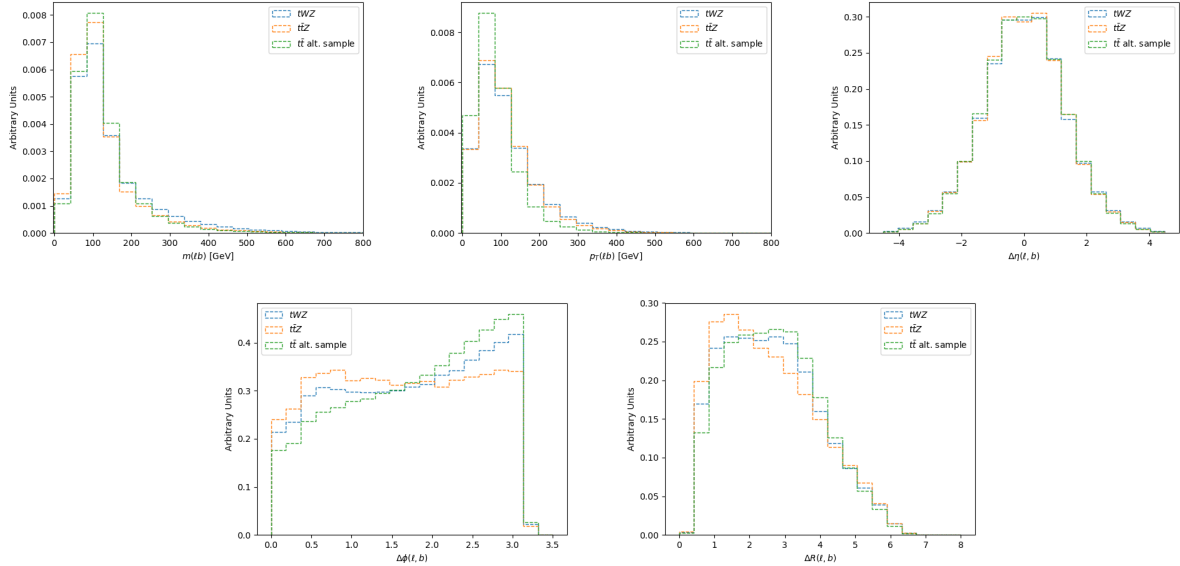


Figure 4.30: Normalised distributions of input variables (ordered from top left to bottom right via decreasing importance) to the object-level BDT in the alternative  $t\bar{t}$ ,  $tWZ$  and  $t\bar{t}Z$  samples, are shown. The green, blue and orange dotted lined histograms represent events from the alternative  $t\bar{t}$ ,  $tWZ$  and  $t\bar{t}Z$  samples (normalised to an area of 1), respectively. The variable used in training is shown on the x-axis. The y-axis shows the relative number of events (in arbitrary units). **From top left to bottom right:** Invariant mass of the  $\ell b$  system.  $\Delta R$  between the  $\ell$  and  $b$ -tagged jet. The  $p_T$  of the  $\ell b$  system.  $\Delta\eta$  between the  $\ell$  and  $b$ -tagged jet.  $\Delta\phi$  between the  $\ell$  and  $b$ -tagged jet.

cross validation. We ensure that the variance of the mean accuracy of each folds' test set in cross validation is substantially small. This indicates that fluctuations in features from different training sets are not learnt by the classifier. For the object-level classifier, a variance of  $3.24 \times 10^{-7}$  was calculated for the mean accuracies of each folds' test set in cross validation, providing further evidence that no over-training occurred.

The output from the object-level BDT was used to construct a variable to be used as input to the event-level BDT. The event-level BDT aims to discriminate between  $tWZ$  and our most prominent background,  $t\bar{t}Z$ . We therefore aim to construct a variable from the output of the object-level BDT which discriminates well between  $tWZ$  and  $t\bar{t}Z$ . Since  $tWZ$  events contain one top quark and  $t\bar{t}Z$  events contain two top quarks, we expect that  $tWZ$  events have one  $\ell b$  combination which scores well and we expect that  $t\bar{t}Z$  events have two  $\ell b$  combinations which score well. We construct a variable,  $\text{BDTScore}\left(\frac{\text{Best}}{\text{2nd Best}}\right)$ , which takes the ratio of the scores of the top scoring  $\ell b$  system to the 2nd best scoring  $\ell b$  system. We expect this variable to be large for  $tWZ$  events and closer to one for  $t\bar{t}Z$  events, therefore providing discrimination between  $tWZ$  and  $t\bar{t}Z$ .

In Figure 4.32, normalised distributions of the signal and total background of the  $\text{BDTScore}\left(\frac{\text{Best}}{\text{2nd Best}}\right)$  variable in the  $tWZ$  OF SR,  $tWZ$  SF SR and  $t\bar{t}Z$  CR are shown.

There doesn't seem to be a large amount of discrimination between signal and background for  $\text{BDTScore}\left(\frac{\text{Best}}{\text{2nd Best}}\right)$  in either of the above regions. We do however see some discrimination in bins near a value of 1, where the number of background events exceed the number of signal events, which is what we expect. This effect is slightly more exaggerated in the  $t\bar{t}Z$  CR than the  $tWZ$  SRs. This can be explained since we expect to have a larger proportion of  $t\bar{t}Z$  events (events with two  $\ell b$  systems) in the  $t\bar{t}Z$  CR. An excess of signal events (compared to background) are observed at larger values. This is to be expected, since these events correspond to a lower score by the  $\ell b$  classifier on the 2nd best scoring  $\ell b$  system in the event. The 2nd best scoring  $\ell b$  system in a  $tWZ$  event is expected to be low, since there is only one  $\ell b$  system originating from a top. Despite the apparent lack of discrimination between signal and background events from this variable, when used as input to training in the event-level BDT (see Section 4.7.2), improves the mean accuracy of the classifier. The tells us that the event-level BDT is taking

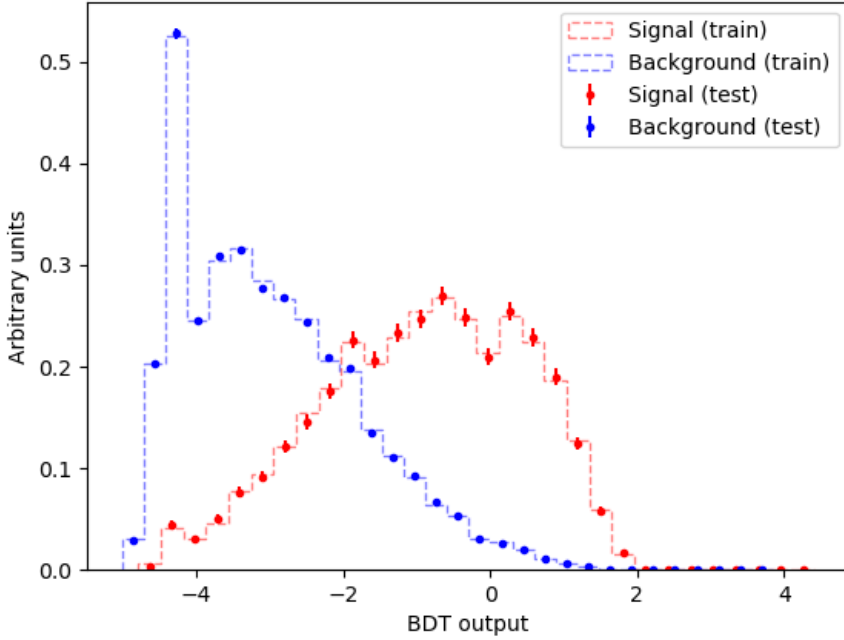


Figure 4.31: Normalised histograms of the object-level BDT discriminator output from the signal and background classes for the training and test sets from the 5th fold in a 5 fold kfold cross validation is shown. The output of the object-level BDT is shown on the x-axis and the relative number of events (in arbitrary units) is shown on the y-axis. The training set for the signal class is shown by the red dotted histogram. The test set for the signal class is shown by the red points, with the total uncertainty represented by the vertical error bars. The training set for the background class is shown by the blue dotted histogram. The test set for the background class is shown by the blue points, with the total uncertainty represented by the vertical error bars.

advantage of the discrimination between signal and background present in the  $\text{BDTScore}(\frac{\text{Best}}{\text{2nd Best}})$  variable.

In an attempt to optimise the performance of the object-level BDT, we aim to train on signal events which are as pure in  $\ell b$  systems originating from top quarks, as possible. Similarly, we aim to train on background events which are as pure in  $\ell b$  systems not originating from top quarks, as possible. This is done by studying the distribution of  $\Delta R$  between the reconstructed  $\ell b$  system and the truth  $\ell b$  system ( $\Delta R((lb)_{reco}, (lb)_{truth})$ ), and excluding  $\ell b$  systems from training which are moderately matched in  $\Delta R$  to their truth counterparts, leaving well matched  $\ell b$  systems being labelled as signal and badly matched  $\ell b$  systems labelled as background. We call the  $\Delta R$  range where  $\ell b$  systems are excluded from training, the exclusion region. In Figure 4.33, the distribution of  $\Delta R$  between the reconstructed  $\ell b$  system and the truth  $\ell b$  system ( $\Delta R((lb)_{reco}, (lb)_{truth})$ ) in the alternative  $t\bar{t}$  sample, along with the exclusion region, is shown.

A large number of reconstructed  $\ell b$  systems have  $\Delta R((lb)_{reco}, (lb)_{truth})$  at values near 0. These are matched (in  $\Delta R$ ) extremely well to truth  $\ell b$  systems originating from top quarks. We therefore define our exclusion region to be between  $0.05 < \Delta R((lb)_{reco}, (lb)_{truth}) < 3.0$ , such that all reconstructed  $\ell b$  systems with  $\Delta R((lb)_{reco}, (lb)_{truth}) \leq 0.05$  are labelled as signal and reconstructed  $\ell b$  systems with  $\Delta R((lb)_{reco}, (lb)_{truth}) \geq 3.0$  are labelled as background. All reconstructed  $\ell b$  systems with  $0.05 < \Delta R((lb)_{reco}, (lb)_{truth}) < 3.0$  are excluded from training.

The performance of the object-level BDT with and without the exclusion region can be compared by studying the discrimination between signal and background events in the  $\text{BDTScore}(\frac{\text{Best}}{\text{2nd Best}})$  variable (object-level output converted to an event-level variable to be used in the event-level BDT) for both object-level BDTs. In Figure 4.34, normalised distributions of  $\text{BDTScore}(\frac{\text{Best}}{\text{2nd Best}})$  using the object-level BDT without the exclusion region (see Figure 4.33) for the  $tWZ$  OF SR,  $tWZ$  SF SR and  $t\bar{t}Z$  CR are shown.

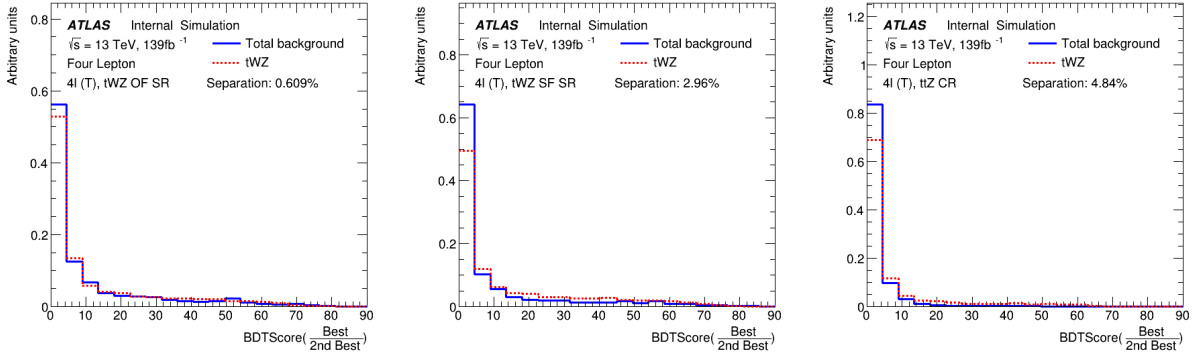


Figure 4.32: Normalised distributions of the signal and total background of the  $\text{BDTScore}(\frac{\text{Best}}{\text{2nd Best}})$  variable in the  $tWZ$  OF SR,  $tWZ$  SF SR and  $t\bar{t}Z$  CR are shown (left to right). The dotted red and solid blue lines represent the distributions (normalised to an area of 1) of the signal and total background events respectively. The x-axis shows the  $\text{BDTScore}(\frac{\text{Best}}{\text{2nd Best}})$  and the y-axis show the relative number of events (in arbitrary units).

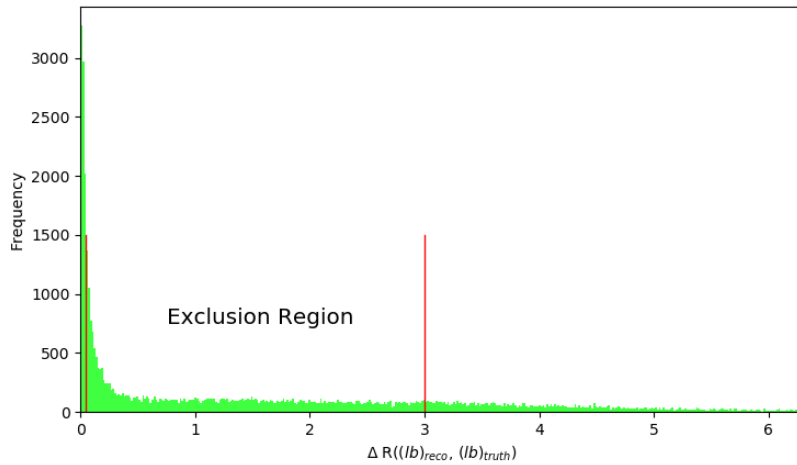


Figure 4.33: The distribution of  $\Delta R$  between the reconstructed  $\ell b$  system and the truth  $\ell b$  system ( $\Delta R((lb)_{reco}, (lb)_{truth})$ ) in the alternative  $t\bar{t}$  sample, along with the exclusion region, is shown. The  $\Delta R$  distribution is shown in green.  $\Delta R$  between the reconstructed  $\ell b$  system and the truth  $\ell b$  system ( $\Delta R((lb)_{reco}, (lb)_{truth})$ ) is shown on the x-axis. The bin frequency is shown on the y-axis. The exclusion region is shown between the vertical red lines situated at  $\Delta R((lb)_{reco}, (lb)_{truth}) = 0.05$  and  $\Delta R((lb)_{reco}, (lb)_{truth}) = 3.0$ . Reconstructed  $\ell b$  systems with  $\Delta R((lb)_{reco}, (lb)_{truth}) \leq 0.05$  are labelled as signal and reconstructed  $\ell b$  systems with  $\Delta R((lb)_{reco}, (lb)_{truth}) \geq 3.0$  are labelled as background.

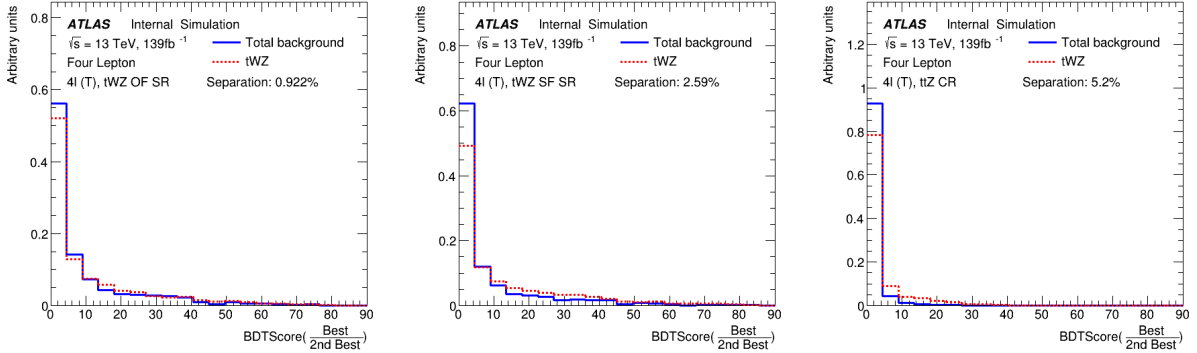


Figure 4.34: Normalised distributions of  $\text{BDTScore}(\frac{\text{Best}}{\text{2nd Best}})$  using the object-level BDT without the exclusion region (see Figure 4.33) for the  $tWZ$  OF SR,  $tWZ$  SF SR and  $t\bar{Z}$  CR are shown (left to right). The dotted red and solid blue lines represent the distributions (normalised to an area of 1) of the signal and total background events respectively. The x-axis shows the  $\text{BDTScore}(\frac{\text{Best}}{\text{2nd Best}})$  and the y-axis show the relative number of events (in arbitrary units).

The amount of discrimination can be quantified by the separation metric, which gives the percentage of the total area of the distributions which do not overlap. A value of 1 indicates that the distributions are fully separated (no overlap) and a value of 0 indicates that the distributions have no separation (fully overlapped). We can compare the separation metrics between the  $\text{BDTScore}(\frac{\text{Best}}{\text{2nd Best}})$  variable in the  $tWZ$  OF SR,  $tWZ$  SF SR and  $t\bar{Z}$  CR for the  $\ell b$  classifier with (Figure 4.32) and without (Figure 4.34) the exclusion region by taking the absolute difference between the two values in each region. The differences are 0.31%, 0.37% and 0.36% for the  $tWZ$  OF SR,  $tWZ$  SF SR and  $t\bar{Z}$  CR, respectively. These differences are minimal and the object-level BDT with the exclusion region outperforms the object-level BDT without the exclusion region in the  $tWZ$  SF SR. Due to the small differences in performance between the two BDTs, for simplicity, we ultimately chose to keep the BDT with the exclusion region.

#### 4.7.2 Event-level BDT

The event-level BDT was trained on 50% of the  $tWZ$  MC sample's events for the signal class and similarly, 50% of the  $t\bar{Z}$  and  $ZZ$  MC sample's events were used for the background class. The samples we train on are individual events, with the features being carefully chosen observables. These observables are chosen on the basis that they are somewhat uncorrelated from one another and show a relatively large amount of separation power between  $tWZ$  and  $t\bar{Z}$ . Similarly to the object-level BDT, the optimum values for the hyper-parameters used were determined via hyper-parameter optimisation. After hyperparameter optimisation, the mean accuracy of each fold (determined from 5 fold kfold cross validation) increased from 0.72 to 0.74 ( $\sim 3\%$  increase). The variable importance of each variable was computed in the same way as described for the object-level BDT (See Section 4.7.1).

In Table 4.8, the variables used in training the event-level BDT are shown.

Observable	Description
$2\nu\text{SM}$	Maximum weight from the $2\nu\text{SM}$ algorithm (See Section 4.8)
$HT$	Scalar sum of jet $p_T$
$LT$	Scalar sum of lepton $p_T$
$\sum p_T(b - \text{jet})$	Scalar sum of $b$ -tagged jet $p_T$
$\text{BDTScore}(\frac{\text{Best}}{\text{2nd Best}})$	Ratio of the top scoring $\ell b$ system to the 2nd best scoring $\ell b$ system from the output of the object-level BDT ( $\ell b$ classifier)
$\Delta\eta(\ell_{1,\text{Non-}Z}, \ell_{2,\text{Non-}Z})$	$\Delta\eta$ between the two leptons, not coming from a $Z$ candidate

Table 4.8: A list of the observables used in the event-level BDT, ordered by importance (descending, top to bottom) is shown.

In Figure 4.35, normalised distributions of the signal and background classes for the training set of all variables used in the event-level BDT are shown.

Overall the BDT input variables show a reasonable amount of discrimination. In particular the output weight from the  $2\nu\text{SM}$  algorithm shows the most discrimination. When determining which variables to use in training the event-level BDT, the output weight from  $2\nu\text{SM}$  was shown to provide the most sizeable boost in performance of the BDT. Surprisingly, the least important variable,  $\Delta\phi$  between the non- $Z$  lepton system (leptons not originating

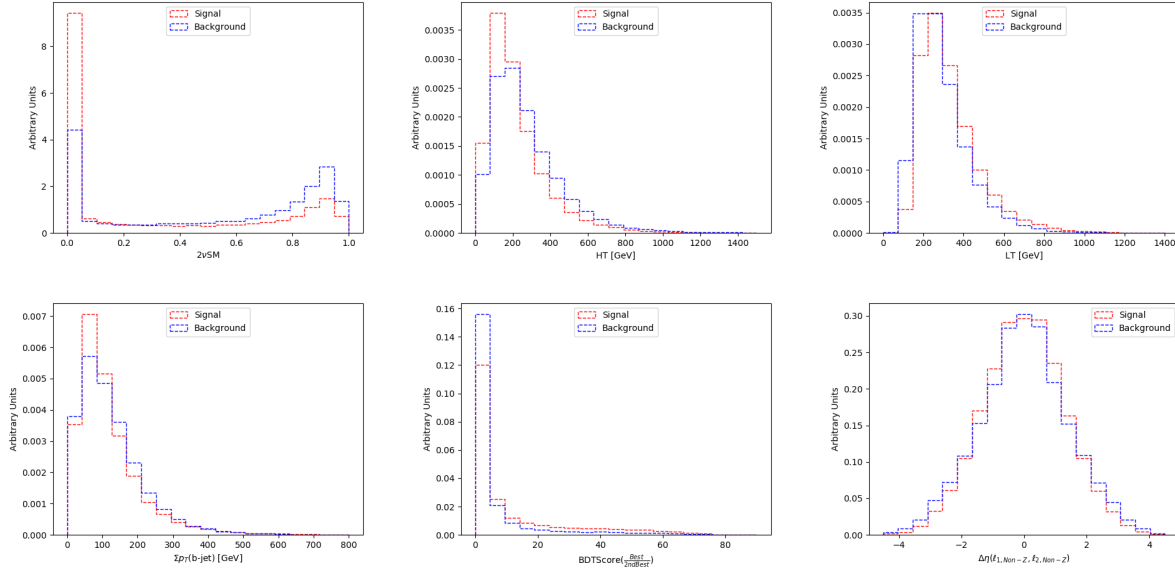


Figure 4.35: Normalised distributions of the signal and background classes for the training set of all variables used in the event-level BDT (ordered from top left to bottom right via decreasing importance) are shown. The red and blue dotted lined histograms represent the signal and background classes events (normalised to an area of 1), respectively. The variable used in training is shown on the x-axis. The y-axis shows the relative number of events for the signal and background classes (in arbitrary units). **From top left to bottom right:** Output weight from the  $2\nu\text{SM}$  algorithm (See Section 4.8). Scalar sum of jet  $p_T$ . Scalar sum of lepton  $p_T$ . Sum of  $b$ -tagged jet  $p_T$ . Ratio of the top scoring  $\ell b$  system to the 2nd best scoring  $\ell b$  system from the output of the object-level BDT (See Section 4.7.1).  $\Delta\eta$  between the two leptons, not coming from a  $Z$  candidate.

from a  $Z$ -candidate) and the leading  $b$ -tagged jet, seem to discriminate well between signal and background. A possible explanation for its low ranking importance is due to it being relatively highly correlated with many of the other input variables.

We can check the modelling of the input variables to the event-level BDT by referring to the pre-fit distributions of data and simulation in the control regions. Note that certain variables which are ill-defined in certain regions (e.g.  $\Delta\eta(\ell_{1,\text{Non-}Z}, \ell_{2,\text{Non-}Z})$  in the  $ZZb$  CR, as all leptons originate from a  $b$ -jet in this region) will not be shown. In Figure 4.36, MC predictions for the input variables to the event-level BDT in the  $t\bar{t}Z$  CR are shown.

In Figure 4.37, MC predictions for the input variables to the event-level BDT in the  $ZZb$  CR are shown.

In Figure 4.38, MC predictions for the input variables to the event-level BDT in the  $(tWZ)_{\text{fake}}$  CR are shown.

Overall, the agreement between data and simulation for the input variables to the event-level BDT is good. Therefore, these variables are well-modelled and reasonable to include as inputs to the event-level BDT.

In Table 4.9, the hyper-parameters used in the event-level BDT are shown.

Hyper-parameter	Value	Description
loss	deviance	The loss function to be optimised
criterion	friedman_mse	The function used to measure the quality of a split
n_estimators	200	The number of boosting stages to perform
learning_rate	0.1	The step size at each iteration during optimisation
max_depth	6	The maximum depth of the individual regression estimators
min_samples_split	2	The minimum number of samples (events) required to split an internal node
min_samples_leaf	1	The minimum number of samples (events) required to be at a leaf node
validation_fraction	0.1	The proportion of training data to set aside as validation set for early stopping
n_iter_no_change	20	Training terminates when the validation score (determined by the validation set) does not improve in all of the previous

Table 4.9: A list of the hyper-parameters used in the event-level BDT is shown. Hyperparameters not listed in this table use the default values as stated in the Scikit-learn Documentation[52].

Since we are training on  $t\bar{t}Z$  and  $ZZ$  events for the background class, we ensure that the relative weighting of these events are such that they mimic the amount of  $t\bar{t}Z$  and  $ZZ$  expected to be present in the regions where we aim to

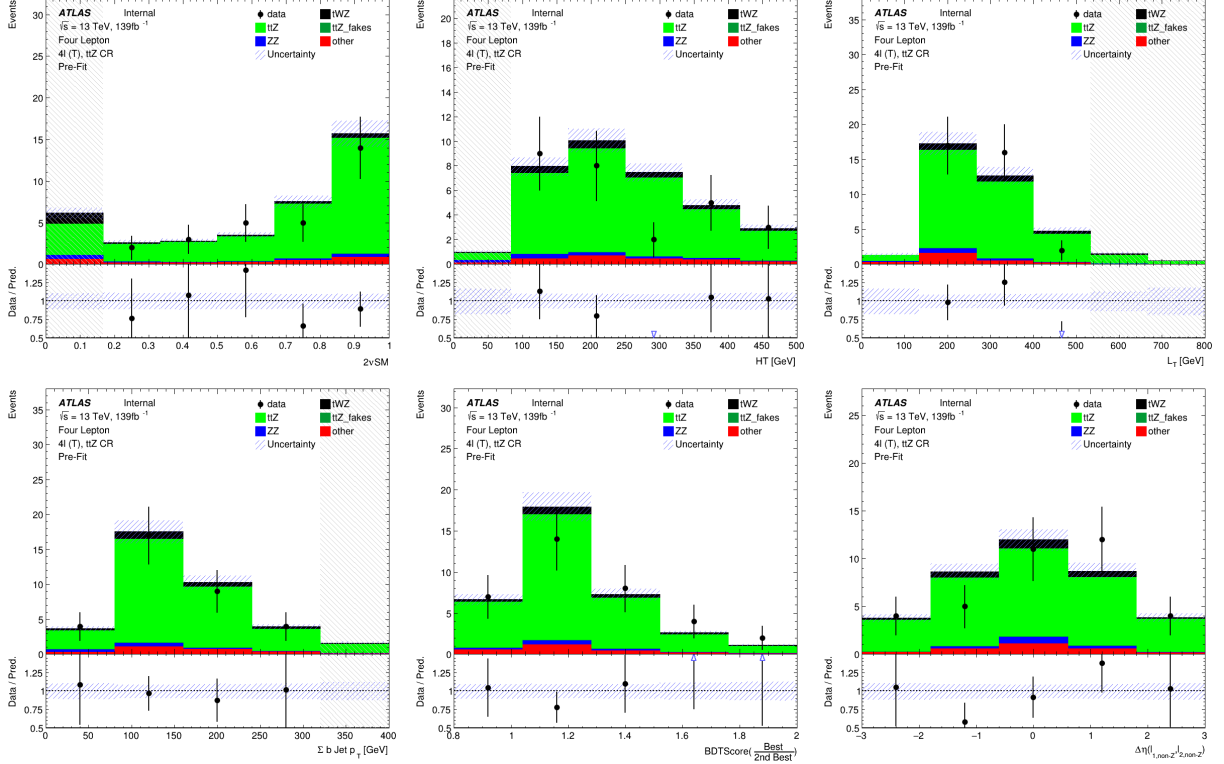


Figure 4.36: Pre-fit distributions of variables used as input to the event-level BDT (ordered from top left to bottom right via decreasing importance), in the  $t\bar{t}Z$  CR, are shown. The data is given by the black points and the MC predictions for each process are given by the histograms. The vertical lines on the data points represent the total uncertainty in the data and the blue diagonal lined bands represent the total MC uncertainty. The lower panel in each plot shows the ratios of the data to the theoretical predictions. Bins with a  $\frac{\text{signal}}{\text{background}}$  yield greater than 0.1 are kept blinded. Blinded bins are shaded with black diagonal lines and their data points are omitted. **From top left to bottom right:** Output weight from the  $2\nu\text{SM}$  algorithm (See Section 4.8). Scalar sum of jet  $p_T$ . Scalar sum of lepton  $p_T$ . Sum of  $b$ -tagged jet  $p_T$ . Ratio of the top scoring  $\ell b$  system to the 2nd best scoring  $\ell b$  system from the output of the object-level BDT (See Section 4.7.1).  $\Delta\eta$  between the two leptons, not coming from a  $Z$  candidate.

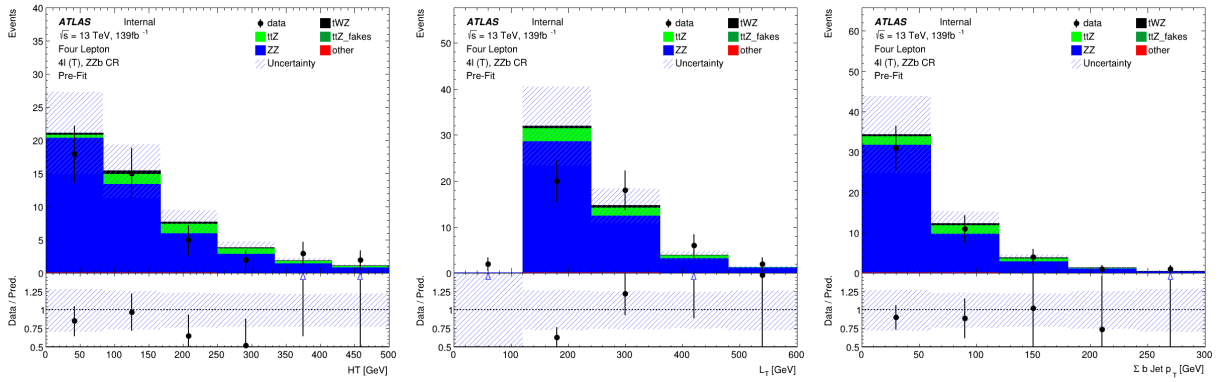


Figure 4.37: Pre-fit distributions of variables used as input to the event-level BDT (ordered from top left to bottom right via decreasing importance), in the  $ZZb$  CR, are shown. The data is given by the black points and the MC predictions for each process are given by the histograms. The vertical lines on the data points represent the total uncertainty in the data and the blue diagonal lined bands represent the total MC uncertainty. The lower panel in each plot shows the ratios of the data to the theoretical predictions. Bins with a  $\frac{\text{signal}}{\text{background}}$  yield greater than 0.1 are kept blinded. Blinded bins are shaded with black diagonal lines and their data points are omitted. **From left to right:** Scalar sum of jet  $p_T$ . Scalar sum of lepton  $p_T$ . Sum of  $b$ -tagged jet  $p_T$ .

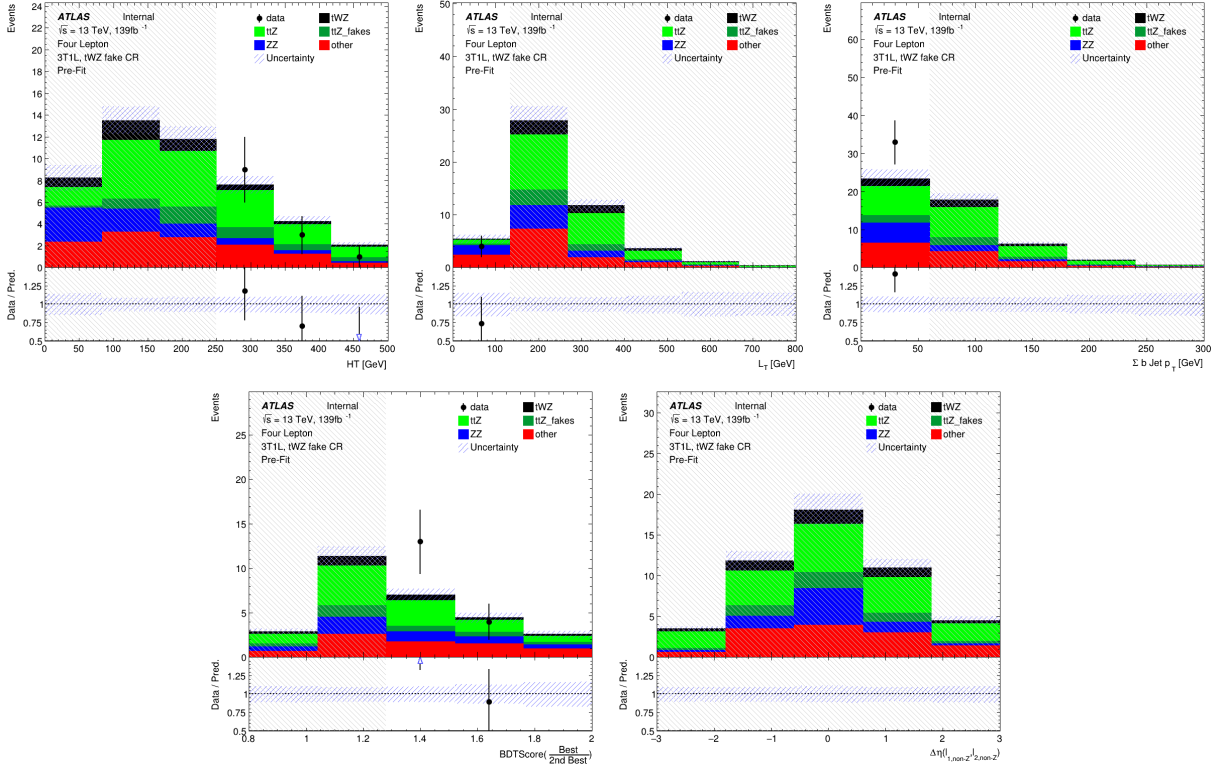


Figure 4.38: Pre-fit distributions of variables used as input to the event-level BDT (ordered from top left to bottom right via decreasing importance), in the  $(tWZ)_{\text{fake}}$  CR, are shown. The data is given by the black points and the MC predictions for each process are given by the histograms. The vertical lines on the data points represent the total uncertainty in the data and the blue diagonal lined bands represent the total MC uncertainty. The lower panel in each plot shows the ratios of the data to the theoretical predictions. Bins with a  $\frac{\text{signal}}{\text{background}}$  yield greater than 0.1 are kept blinded. Blinded bins are shaded with black diagonal lines and their data points are omitted. **From top left to bottom right:** Output weight from the  $2\nu\text{SM}$  algorithm (See Section 4.8). Scalar sum of jet  $p_T$ . Scalar sum of lepton  $p_T$ . Sum of  $b$ -tagged jet  $p_T$ . Ratio of the top scoring  $\ell b$  system to the 2nd best scoring  $\ell b$  system from the output of the object-level BDT (See Section 4.7.1).  $\Delta\eta$  between the two leptons, not coming from a  $Z$  candidate.

use the BDT discriminator ( $tWZ$  SRs and  $t\bar{t}Z$  CR). This is done by applying normalization weights to each event, defined as,

$$W = \frac{\sigma \mathcal{L} \text{weight(MC)}}{\text{totalWeight(MC)}} \quad (4.2)$$

where  $\sigma$  is the cross section of the process,  $\mathcal{L}$  is the integrated luminosity,  $\text{weight(MC)}$  is the weight assigned to the event by the MC generator and  $\text{totalWeight(MC)}$  is the sum of those weights for all the generated events.

The number of events used in training for the signal and background classes were 41066 and 22608 respectively. Similarly to the object-level BDT, there is a dataset imbalance. We correct this imbalance (in the same way as before with the object-level BDT) by ensuring that the relative weighting of each event is such that the sum of the signal weights is equal to the sum of the background weights.

In Figure 4.40 the normalised histograms of the training and test sets (extracted from fold 5 from a 5 fold kfold cross validation) for signal and background is shown.

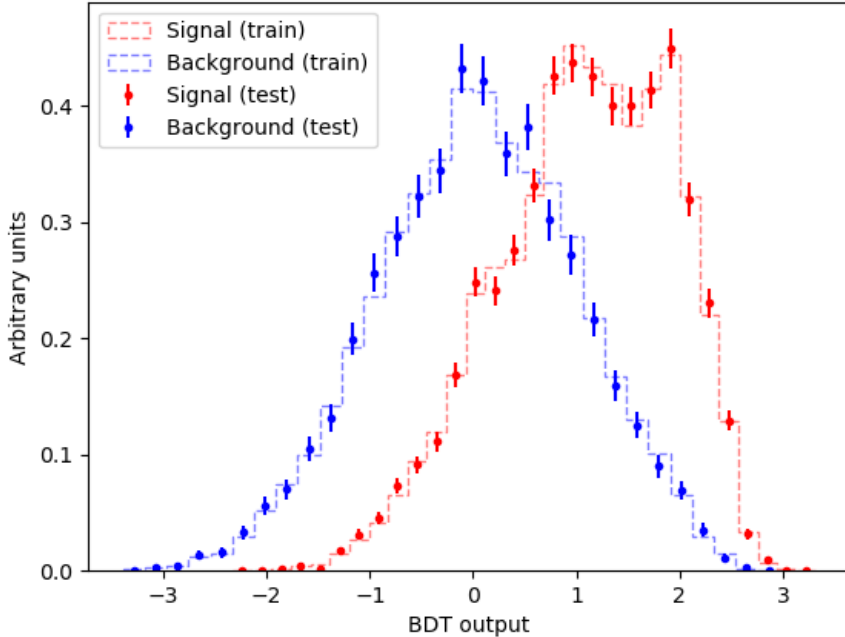


Figure 4.39: Normalised histograms of the event-level BDT discriminator output from the signal and background classes for the training and test sets from the 5th fold in a 5 fold kfold cross validation are shown. The output of the event-level BDT is shown on the x-axis and the relative number of events (normalised to have an area of 1, in arbitrary units) is shown on the y-axis. The training set for the signal class is shown by the red dotted histogram. The test set for the signal class is shown by the red points, with the total uncertainty represented by the vertical error bars. The training set for the background class is shown by the blue dotted histogram. The test set for the background class is shown by the blue points, with the total uncertainty represented by the vertical error bars.

We can see that the shapes of the training and test sets for both signal and background are very similar. This is a good indicator that no over-training occurred. As with the object-level BDT, we perform another over-training check, by ensuring that the variance of the mean accuracy of each folds' test set in a 5 fold kfold cross validation is substantially small. This indicates that fluctuations in features from different training sets are not learnt by the classifier. For the event-level classifier, a variance of 0.00026 was calculated for the mean accuracies of each folds' test set in cross validation, providing further evidence that no over-training occurred.

In Figure ??, normalised distributions of the signal and total background of the event-level BDT discriminator output in the  $tWZ$  OF SR,  $tWZ$  SF SR and  $t\bar{Z}$  CR, are shown.

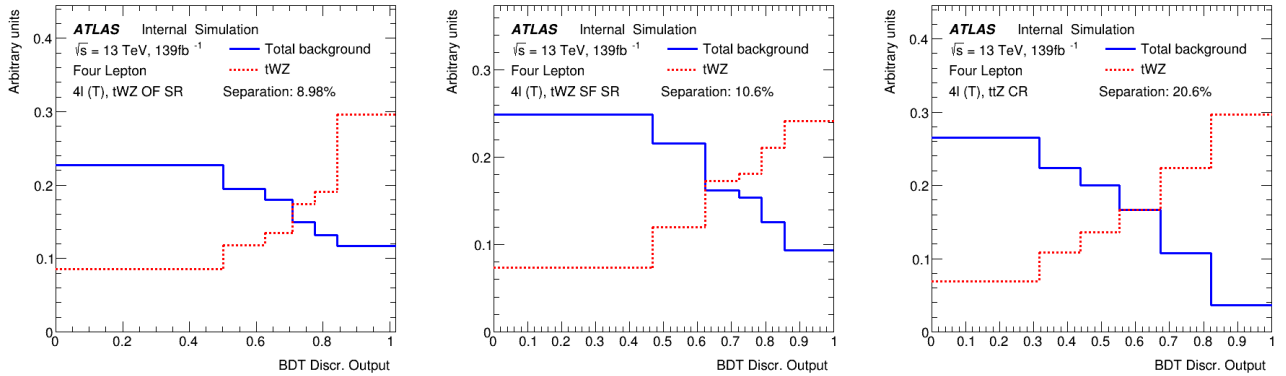


Figure 4.40: Normalised distributions of the signal and total background of the event-level BDT discriminator output in the  $tWZ$  OF SR,  $tWZ$  SF SR and  $t\bar{Z}$  CR are shown (left to right). The dotted red and solid blue lines represent the distributions (normalised to an area of 1) of the signal and total background events respectively. The x-axis shows the event-level BDT discriminator output and the y-axis shows the relative number of events (in arbitrary units).

The event-level BDT discriminates well between signal and background events in the  $tWZ$  OF SR,  $tWZ$  SF SR and  $t\bar{Z}$  CR, with separations of 8.98%, 10.6% and 20.6%, respectively.

## 4.8 Two Neutrino Scanning Method ( $2\nu$ SM) Algorithm

The Two Neutrino Scanning Method ( $2\nu$ SM) algorithm<sup>2</sup> [43, 42] aims to reconstruct  $t\bar{t}$  systems in the  $2\ell$ ,  $3\ell$  and  $4\ell$  final states (e.g.  $2\ell$  case:  $t\bar{t} \rightarrow \ell^+ \nu_\ell b\bar{b} \ell^- \bar{\nu}_\ell \bar{b}$ ). This was initially designed to suppress the  $t\bar{t}$  background in the  $t\bar{t}Z$  analysis. We can re-purpose this algorithm to distinguish between  $tWZ$  and  $t\bar{Z}$  by removing the easily-identifiable  $Z$  boson.

The  $2\nu$ SM algorithm reconstructs a  $t\bar{t}$  system by scanning through the components of two possible neutrino 4-vectors ( $\nu_1$  and  $\nu_2$ ). It then aims to determine which  $\nu_1$  and  $\nu_2$  correspond to the two neutrinos which originate from the decay of a  $t\bar{t}$  system the best (quantified by an output weight,  $w_{2\nu SM}$ ).  $w_{2\nu SM}$  is the likelihood under the  $t\bar{t}$  dilipeton final state hypothesis. We are able to use this algorithm in our analysis to discriminate between  $tWZ$  and  $t\bar{Z}$  since we can easily reconstruct the OSSF leptons which decay from the  $Z$  boson and remove it before inputting the event into the algorithm. We would then expect that the  $2\nu$ SM algorithm returns a higher score from a  $t\bar{Z}$  event ( $\sim 1$ , i.e. it looks like a  $t\bar{t}$  event after removal of the  $Z$  boson) and a lower score from a  $tWZ$  event ( $\sim 0$ , i.e. it does not look like a  $t\bar{t}$  event after removal of the  $Z$  boson).

### 4.8.1 The algorithm

The  $2\nu$ SM algorithm starts off by writing down four equations which correspond to the invariant masses of the top quark ( $m(t)$ ) and  $W$  boson ( $m(W)$ ) for the two top decays (i.e.  $t \rightarrow W^+ b \rightarrow \ell^+ \nu_\ell$ ) in a dileptonic  $t\bar{t}$  event. These can be written as,

$$(\ell_1 + \nu_1)^2 = m(W)^2 = (80.385 \text{ GeV})^2 \quad (4.3)$$

$$(\ell_1 + \nu_1 + b_{1,2})^2 = m(t)^2 = (172.5 \text{ GeV})^2 \quad (4.4)$$

$$(\ell_2 + \nu_2)^2 = m(W)^2 = (80.385 \text{ GeV})^2 \quad (4.5)$$

$$(\ell_2 + \nu_2 + b_{2,1})^2 = m(t)^2 = (172.5 \text{ GeV})^2 \quad (4.6)$$

<sup>2</sup>software tool and weights provided by Thomas McCarthy ( $t\bar{Z}$  analysis group - Max Planck Institute)

where the subscripts indicate that these particles originate from the decay of two different top quarks in a  $t\bar{t}$  system. We assume that the mass of the neutrinos ( $\nu_1$  and  $\nu_2$ ) are close to zero, which leaves us with 6 unknowns,  $p_{T,\nu_1}$ ,  $\phi_{\nu_1}$ ,  $\eta_{\nu_1}$ ,  $p_{T,\nu_2}$ ,  $\phi_{\nu_2}$  and  $\eta_{\nu_2}$  (components of the two neutrino's 4-vectors).

The  $2\nu$ SM algorithm takes the 4-vectors of the two reconstructed leptons (not from the  $Z$  boson) and the two jets with the highest DL1r  $b$ -tagger score as input. For each neutrino ( $\nu_1$  and  $\nu_2$ ), we scan over a range of possible  $\eta$  and  $\phi$  values. These values were chosen to be  $\phi_{\nu_1}, \phi_{\nu_2} \in [-\pi, \pi]$  with a step size of  $\approx 0.25$  and  $\eta_{\nu_1}, \eta_{\nu_2} \in [-5, 5]$  with a step size of  $\approx 0.31$ . These ranges were chosen to maximize accuracy and minimize computation time. For each of these possible  $\eta$  and  $\phi$  values, we calculate the corresponding  $p_T$  for each neutrino. The transverse momentum of a neutrino,  $p_{T,\nu}$ , can be calculated via (\*\*referencne somewhere here\*\*\*\*),

$$p_{T,\nu} = \frac{\frac{1}{2}(m(W)^2 - m(\ell)^2)}{E_\ell \cosh \eta_\nu - p_{\ell,z} \sinh \eta_\nu - p_{\ell,x} \cos \phi_\nu - p_{\ell,y} \sin \phi_\nu} \quad (4.7)$$

where  $E_\ell$  is the energy of the lepton and  $p_{\ell,z}, p_{\ell,x}, p_{\ell,y}$  are the  $z, x$  and  $y$  components of lepton's momentum. At this stage, we have possible 4-vectors for  $\nu_1$  and  $\nu_2$ . Using these possible neutrino 4-vectors, we reconstruct the two possible  $t\bar{t}$  systems,

$$t_1 = \ell_1 + b_1 + \nu_1 \text{ and } t_2 = \ell_2 + b_2 + \nu_2 \quad (4.8)$$

**OR**

$$t_1 = \ell_1 + b_2 + \nu_1 \text{ and } t_2 = \ell_2 + b_1 + \nu_2 \quad (4.9)$$

These reconstructed  $t\bar{t}$  systems are then used to calculate a weight,  $w_{2\nu SM}$ . The  $w_{2\nu SM}$  weight (a value ranging from 0 to 1) is defined as a product of four probabilities (described below) and can be written as,

$$w_{2\nu SM} = P_{m_{t_1}} \times P_{m_{t_2}} \times P_{\Delta E_x} \times P_{\Delta E_y} \quad (4.10)$$

The  $w_{2\nu SM}$  is calculated for each pair of reconstructed neutrinos (or reconstructed  $t\bar{t}$  systems), with the maximum value being chosen as the final value for the event.

## 4.8.2 Calculating $w_{2\nu SM}$

We use distributions of well modelled observables ( $m_{b\ell\nu}$  and  $\Delta E_x$ ) from simulated  $t\bar{t}$  events in order to determine how well our reconstructed neutrinos (and in turn top quarks) resemble neutrinos (and top quarks) present in a  $t\bar{t}$  event.

### 4.8.2.1 $P_{m_{t_1}}$ and $P_{m_{t_2}}$

A normalised distribution of the mass of reconstructed top quarks ( $m_{b\ell\nu}$ ) from a  $t\bar{t}$  sample is generated to determine the probabilities  $P_{m_{t_1}}$  and  $P_{m_{t_2}}$ . The distribution is generated from reco-level leptons, generator-level neutrinos and reoc-level jets matched in  $\Delta R$  to generator-level  $b$ -quarks, therefore only filling the distribution with correct detector-level objects. We then use the distribution to interpolate our two reconstructed top quarks, which returns a weight value from 0 to 1, with higher values corresponding to a reconstructed top quark which has a mass close to that of a top quark from a  $t\bar{t}$  system. This interpolation is done for both reconstructed tops,  $t_1$  and  $t_2$ , corresponding to probabilities  $P_{m_{t_1}}$  and  $P_{m_{t_2}}$ . The distribution used is shown in Figure 4.41.

In Figure 4.41, the  $m_{b\ell\nu}$  distribution (generated from simulated  $t\bar{t}$  events), used to calculate  $P_{m_{t_1}}$  and  $P_{m_{t_2}}$  is shown.

### 4.8.2.2 $P_{\Delta E_x}$ and $P_{\Delta E_y}$

A similar method is used to determine  $P_{\Delta E_x}$  and  $P_{\Delta E_y}$ . In this case we generate a weight distribution of  $\Delta E_x = (p_{T,\nu_1})_x + (p_{T,\nu_2})_x - (E_T^{\text{miss}})_x$  based off simulated  $t\bar{t}$  events. In particular, this distribution is generated using reco-level  $E_T^{\text{miss}}$  and generator-level neutrinos. The use of this distribution lies under the assumption that neutrinos are the dominant source of  $E_T^{\text{miss}}$ , and therefore,  $(E_T^{\text{miss}})_x \approx (p_{T,\nu_1})_x + (p_{T,\nu_2})_x$  and  $(E_T^{\text{miss}})_y \approx (p_{T,\nu_1})_y + (p_{T,\nu_2})_y$ . We then use the distribution to interpolate the value of  $\Delta E_x$  and  $\Delta E_y$  from our reconstructed neutrinos. This returns a weight value from 0 to 1, with higher values corresponding to  $\Delta E_x$  and  $\Delta E_y$  (and in turn our reconstructed neutrino's  $p_T$ ) closer to those observed in a  $t\bar{t}$  event. We expect the  $\Delta E_x$  and  $\Delta E_y$  distributions to have the same shapes, therefore we only need to generate one (we have chosen  $\Delta E_x$ ). In Figure 4.42, the  $m_{b\ell\nu}$  distribution (generated from simulated  $t\bar{t}$  events), used to calculate  $P_{m_{t_1}}$  and  $P_{m_{t_2}}$  is shown.

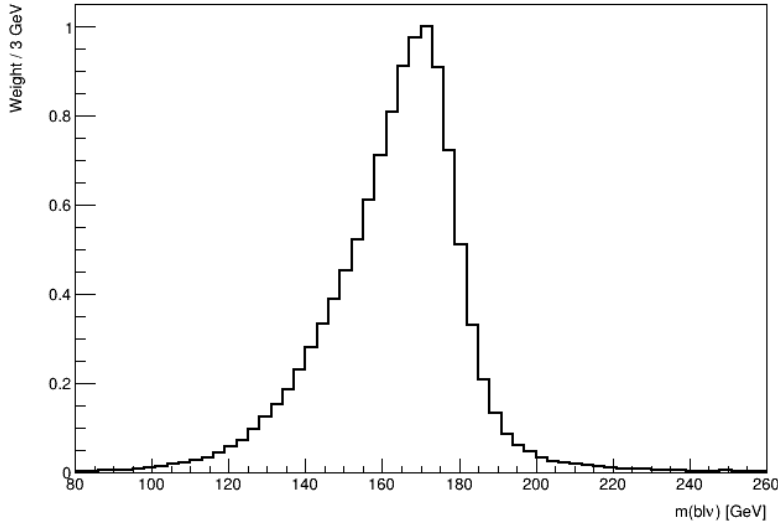


Figure 4.41:  $m_{b\ell\nu}$  distribution generated from simulated  $t\bar{t}$  events, used to calculate  $P_{m_{t_1}}$  and  $P_{m_{t_2}}$  is shown. The  $m_{b\ell\nu}$  distribution is shown by the black lined histogram. The mass of the  $b\ell\nu$  system is shown on the x-axis. The corresponding weight of the  $m_{b\ell\nu}$  distribution is shown on the y-axis.

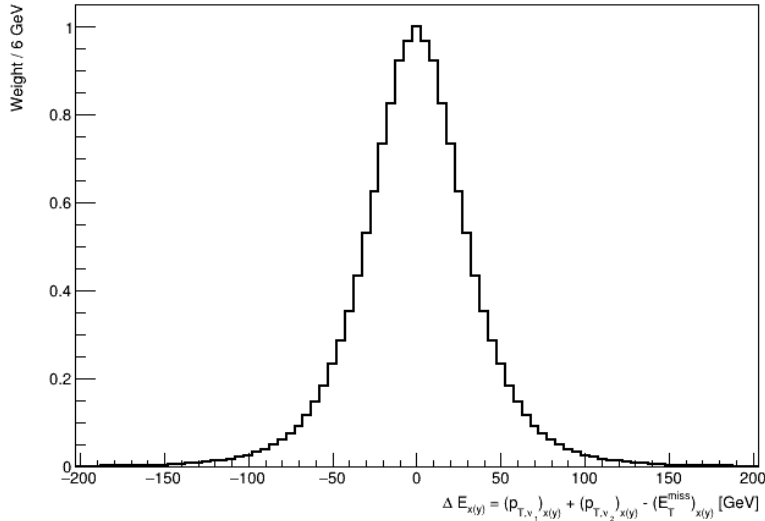


Figure 4.42:  $\Delta E_x$  distribution generated from simulated  $t\bar{t}$  events, used to calculate  $P_{\Delta E_x}$  and  $P_{\Delta E_y}$  is shown. The  $\Delta E_x$  distribution is shown by the black lined histogram.  $\Delta E_x$  is shown on the x-axis. The corresponding weight of  $\Delta E_x$  distribution is shown on the y-axis.

### 4.8.3 Kinematic Veto

The  $2\nu$ SM algorithm is extremely computationally intensive. The computation time depends on the number step size of the  $\phi$  and  $\eta$  ranges which we scan over to reconstruct the neutrinos. For example, consider the step sizes chosen in this analysis,  $\Delta\eta \approx 0.31$  and  $\Delta\phi \approx 0.25$  which corresponds to 32 values for  $\eta$  and 25 values for  $\phi$ . There will be  $(32)(32)(25) = 640\,000$  possible pairs of neutrinos ( $\nu_1$  and  $\nu_2$ ) to consider **per event**. Since we have to consider two possible  $t\bar{t}$  systems (See Equations 4.8 and 4.9), this number effectively increases to  $(2)(640000) = 128\,000$  iterations **per event**. In order to reduce the number of  $t\bar{t}$  systems we need to consider, therefore decreasing computation time, we look at distributions of well modelled observables from  $t\bar{t}$  events and veto (discard) a possible reconstructed  $t\bar{t}$  system if the observable in question is improbable or unlikely to be observed in a  $t\bar{t}$  event. To achieve this, we define a threshold range for these observables (See Figure 4.45 and Figure 4.47), and if the possible reconstructed  $t\bar{t}$  system's corresponding value for this observable lies outside this range, it is vetoed and the algorithm continues with the next iteration.

#### 4.8.3.1 $\Delta\langle m(\ell b) \rangle$

The first observable which we consider is the difference between average mass of the two possible  $\ell b$  system combinations,  $\Delta\langle m(\ell b) \rangle$ . The two possible  $\ell b$  system combinations are,

$$(\ell b)_1 = \ell_1 + b_1 \text{ and } (\ell b)_2 = \ell_2 + b_2 \quad (4.11)$$

**OR**

$$(\ell b)_1 = \ell_1 + b_2 \text{ and } (\ell b)_2 = \ell_2 + b_1 \quad (4.12)$$

$$(4.13)$$

$\Delta\langle m(\ell b) \rangle$  is therefore defined as,

$$\Delta\langle m(\ell b) \rangle = \frac{1}{2} |[(m(\ell_1 b_1) + m(\ell_1 b_1)) - (m(\ell_1 b_2) + m(\ell_2 b_1))]| \quad (4.14)$$

The idea here is that, if  $\Delta\langle m(\ell b) \rangle$  is large, it's more likely that we can simply select the  $\ell b$  combination with the smaller (minimum) average mass. To illustrate this, we look at the distribution (constructed from  $t\bar{t}$  events) of  $P(\text{Correct combination of } \ell b \text{ systems}|\text{minimum}\langle m(\ell b) \rangle)$  vs  $\Delta\langle m(\ell b) \rangle$  for  $b$ -tagged jets in the same ( $\eta(b_1) \times \eta(b_2) \geq 0$ ) and opposite hemispheres ( $\eta(b_1) \times \eta(b_2) < 0$ ).

In Figure 4.43 the  $P(\text{Correct combination of } \ell b \text{ systems}|\text{minimum}\langle m(\ell b) \rangle)$  vs  $\Delta\langle m(\ell b) \rangle$ , for  $b$ -tagged jets in the same and opposite hemispheres, constructed from  $t\bar{t}$  events is shown.

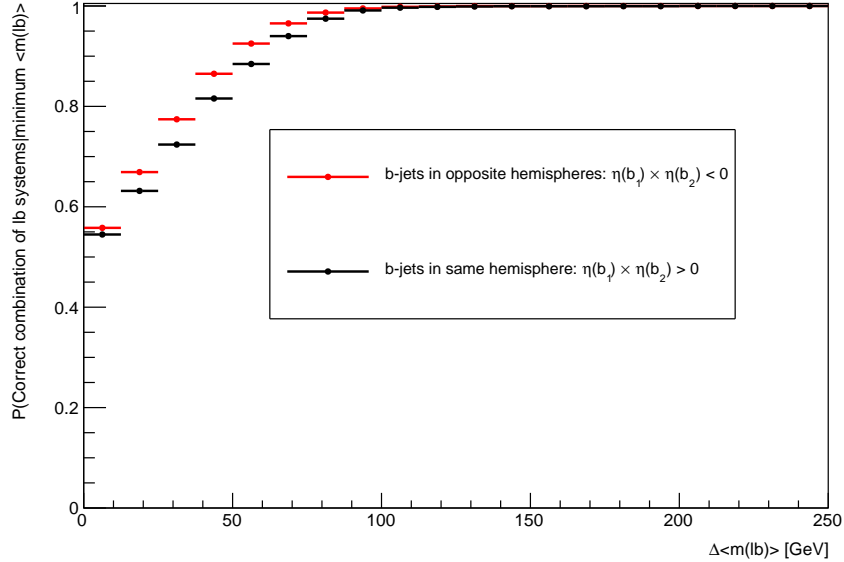


Figure 4.43:  $P(\text{Correct combination of } \ell b \text{ systems}|\text{minimum}\langle m(\ell b) \rangle)$  vs  $\Delta\langle m(\ell b) \rangle$ , for  $b$ -tagged jets in the same and opposite hemispheres, constructed from  $t\bar{t}$  events is shown. The horizontal red lines represent the distribution in the case when the two  $b$ -jets are in opposite hemispheres. The dot in the middle of the line represents the midpoint of the line. The horizontal black lines represent the distribution in the case when the two  $b$ -jets are in the same hemispheres. The dot in the middle of the line represents the midpoint of the line. The average  $m(\ell b)$  is shown on the x-axis. The  $P(\text{Correct combination of } \ell b \text{ systems}|\text{minimum}\langle m(\ell b) \rangle)$  is shown on the y-axis.

From Figure 4.43, for both cases where the  $b$ -tagged jets are in the same and opposite hemispheres, the probability for a correct  $\ell b$  system being chosen given that we are considering the  $\ell b$  system with minimum average mass is an increasing function which plateaus to 1 at  $\sim 90$  GeV. We use these two distributions to interpolate the  $P(\text{Correct combination of } \ell b \text{ systems}|\text{minimum}\langle m(\ell b) \rangle)$  from  $\Delta\langle m(\ell b) \rangle$ . We require that  $P(\text{Correct combination of } \ell b \text{ systems}|\text{minimum}\langle m(\ell b) \rangle) > 0.8$ , before vetoing any  $\ell b$  combination, such that we have at least 80% certainty that we know the correct  $\ell b$  combination. In this case, the  $\ell b$  combination with the

maximum  $\Delta\langle m(\ell b) \rangle$  is vetoed. If  $P(\text{Correct combination of } \ell b \text{ systems} | \text{minimum}\langle m(\ell b) \rangle) < 0.8$  we need to consider both possible  $\ell b$  system combinations.

#### 4.8.3.2 $\eta(b\bar{b}\ell\ell)$

We consider  $\eta$  of the  $b\bar{b}\ell\ell$  system,  $\eta(b\bar{b}\ell\ell)$  to veto improbable  $\eta(\nu_1)$  and  $\eta(\nu_2)$  values.

In the same way as for  $\Delta\langle m(\ell b) \rangle$ , we generate a distribution to determine values  $\eta(\nu)$  which are improbable for a  $t\bar{t}$  event. In this case, we generate a 2D histogram from simulated  $t\bar{t}$  events (dileptonic final state) at generator-level of  $\eta(\nu)$  vs  $\eta(b\bar{b}\ell\ell)$ .

In Figure 4.44, a heatmap of occupancy for  $\eta(\nu)$  vs  $\eta(b\bar{b}\ell\ell)$  (produced from simulated  $t\bar{t}$  events) is shown.

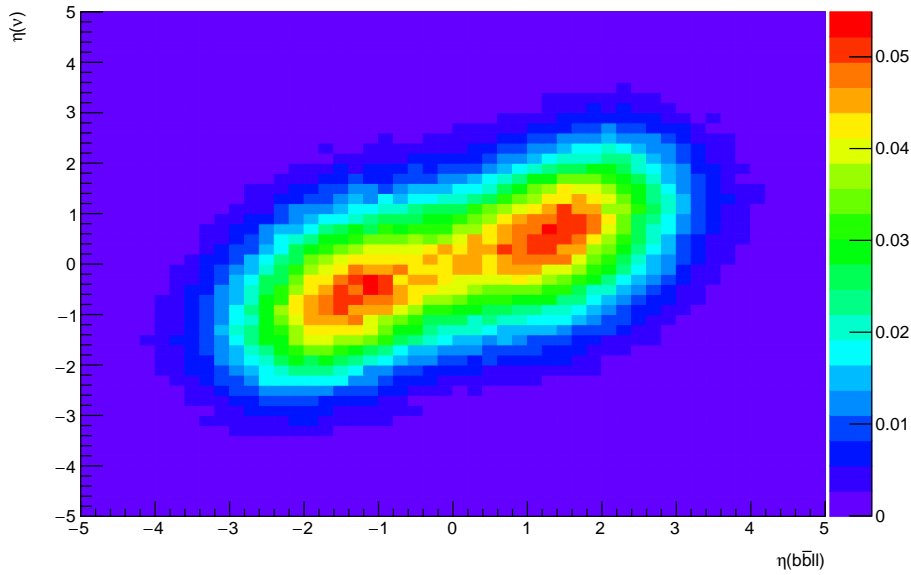


Figure 4.44: Heatmap of occupancy for  $\eta(\nu)$  vs  $\eta(b\bar{b}\ell\ell)$  produced from simulated  $t\bar{t}$  events (dileptonic final state) at generator-level is shown.  $\eta$  of the  $b\bar{b}\ell\ell$  system is shown on the x-axis.  $\eta$  of the neutrino is shown on the y-axis. The colorbar on the right represents the occupancy (normalised) in the phase space.

Using the above heatmap, we define a veto region (where a  $t\bar{t}$  event is extremely unlikely to occur) based off double-sided 95% limits (\*\*something here on confidence limit??\*\*). We apply a veto if either possible neutrino lies within this region. The veto region is shown in Figure 4.45.

In Figure 4.45, the veto region (extracted from Figure 4.44) for vetoing improbable neutrinos is shown.

#### 4.8.3.3 $L_T$

The final kinematic constraint which we consider is the scalar sum of lepton  $p_T$ ,  $L_T = p_T(\ell_1) + p_T(\ell_2)$  which we use to veto certain possible neutrinos,  $\nu_1$  and  $\nu_2$ .

Again, we generate a distribution to determine (and veto) improbable possible neutrinos in simulated  $t\bar{t}$  events (dilepton final state).

In Figure 4.46, a heatmap of occupancy for  $\Delta R(\ell, \nu)$  vs  $L_T$  (produced from simulated  $t\bar{t}$  events) is shown.

Using the same method as described in Section 4.8.3.2, we define a veto region where a veto is applied if either possible neutrino lies within this region. In Figure 4.45, the veto region (extracted from Figure 4.46) for vetoing improbable neutrinos values is shown.

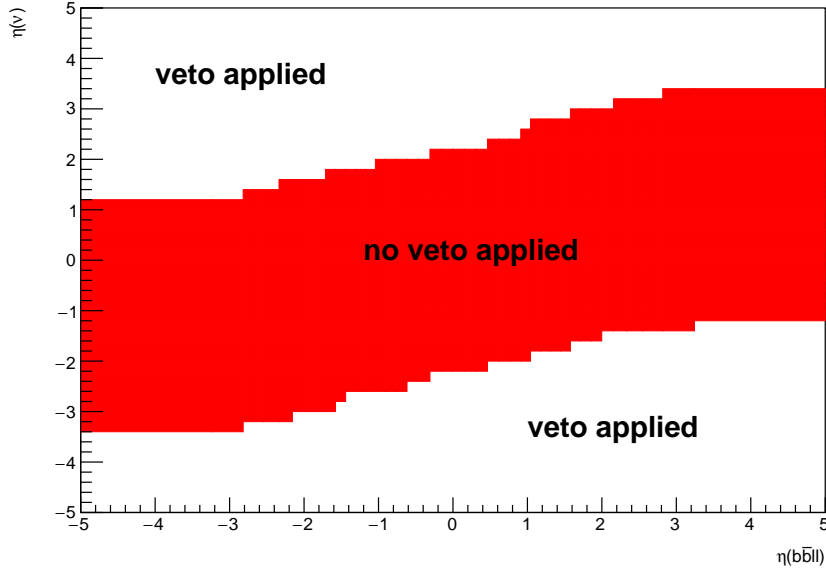


Figure 4.45: The regions where vetoes are applied for the  $\eta(b_1 b_2 \ell_1 \ell_2)$  constraint is shown.  $\eta$  of the  $b\bar{b}\ell\ell$  system is shown on the x-axis.  $\eta$  of the neutrino is shown on the y-axis. The red band shows the region where the neutrino would not be vetoed. The white areas (above and below the red band) are regions where the neutrino is vetoed.

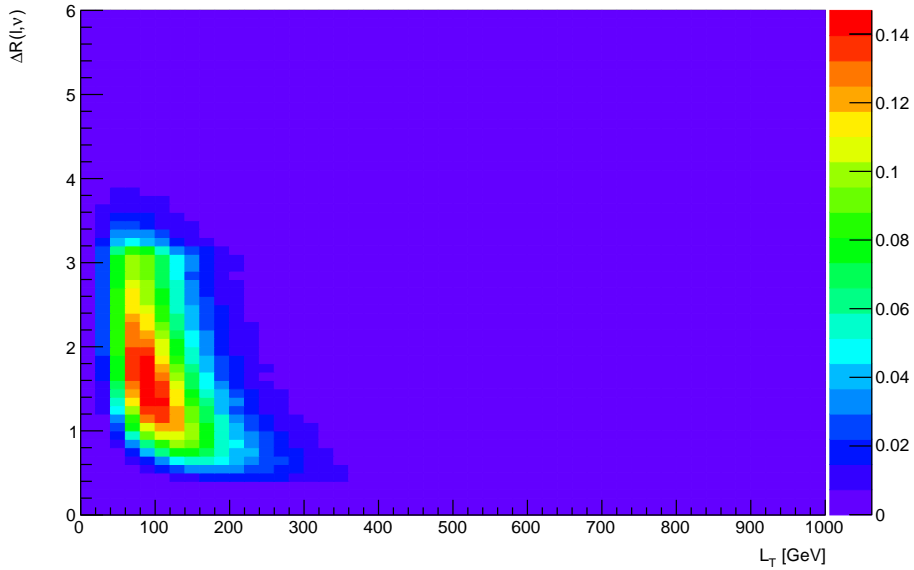


Figure 4.46: A heatmap of occupancy for  $\Delta R(\ell, \nu)$  vs  $L_T$  produced from simulated  $t\bar{t}$  events (dileptonic final state) at generator-level is shown.  $\Delta R$  between leptons and neutrinos is shown on the x-axis.  $L_T$  (scalar sum of lepton  $p_T$ ) is shown on the y-axis. The colorbar on the right represents the occupancy (normalised) in the phase space.

## 4.9 Systematics

The systematic uncertainties can be separated into experimental (detector) systematics, which are related to the reconstruction of physics objects in the detector and theoretical uncertainties related to the modelling of the different processes background.

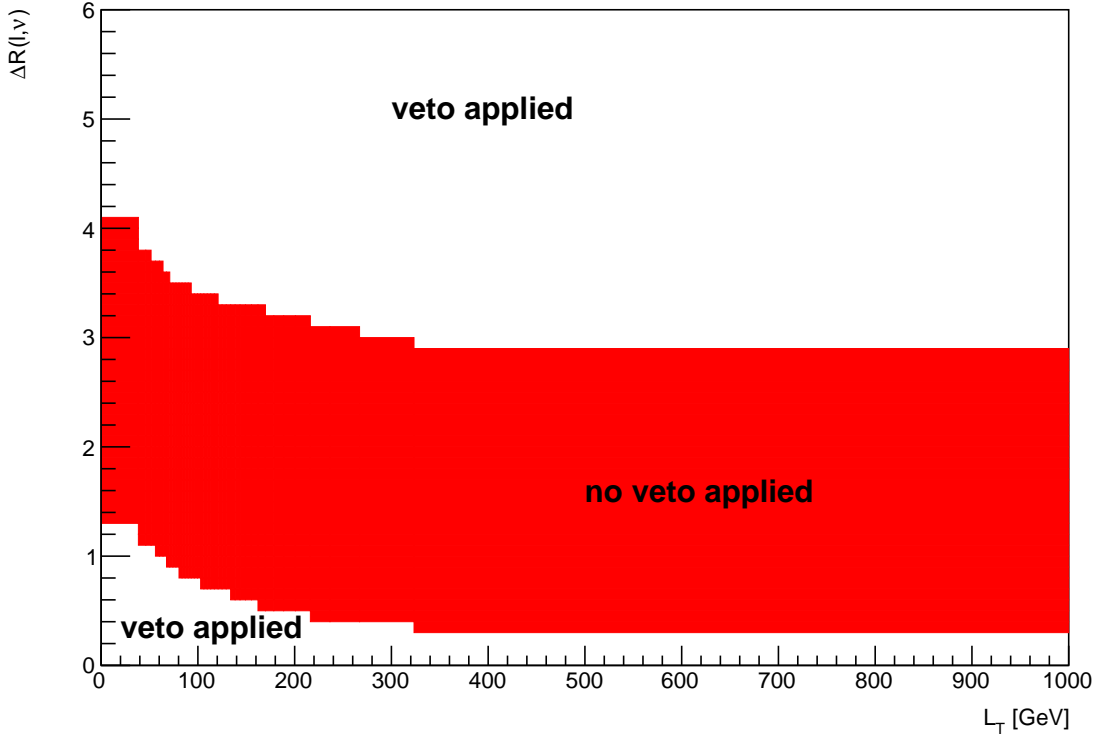


Figure 4.47: The regions where vetoes are applied for the  $L_T$  constraint is shown.  $\Delta R$  between leptons and neutrinos is shown on the x-axis.  $L_T$  (scalar sum of lepton  $p_T$ ) is shown on the y-axis. The red band shows the region where the neutrino would not be vetoed. The white areas (above and below the red band) are regions where the neutrino is vetoed.

#### 4.9.1 Experimental uncertainties

In this section, the experimental systematics are outlined.

- **Luminosity:**

The 2015–2018 luminosity estimate of  $139\text{fb}^{-1}$  has a relative uncertainty of 3%. This uncertainty is obtained using the LUCID-2 detector [18] for the primary luminosity measurements. This systematic uncertainty affects all processes modelled using MC simulations.

- **Pile-up reweighting:**

An uncertainty related to the SFs used for MC to account for differences in pile-up distributions between MC and data is applied. This uncertainty is obtained by re-scaling the  $\langle\mu\rangle$  value in data by 1.00 and 1/1.18 corrections are only applied to MC.

- **Jet vertex tagger:**

Uncertainties associated to the  $JVT$  are applied via the `JetJvtEfficiency` package [16] which account for the residual contamination from pile-up jets after pile-up suppression and the MC generator choice [10].

- **Heavy- and light-flavor tagging:**

The efficiency of the flavour-tagging algorithm is measured for each jet flavour using control samples in data and in simulation. From these measurements, correction factors are derived to correct the tagging rates in the simulation. In the case of  $b$ -tagged jets, the correction factors and their uncertainties are estimated from data using dileptonic  $t\bar{t}$  events [12, 7]. In the case of  $c$ -jets, they are derived from jets arising from  $W$  boson decays in  $t\bar{t}$  events [11]. In the case of light-flavour jets, the correction factors are derived using dijet events [8]. Sources of uncertainty affecting the  $b$ - and  $c$ -tagging efficiencies are evaluated as a function of jet  $p_T$ , including

bin-to-bin correlations. The uncertainties in the efficiency for tagging light-flavour jets depend on the jet  $p_T$  and on  $\eta$ . An additional uncertainty is assigned to account for the extrapolation of the  $b$ -tagging efficiency measurement from the  $p_T$  region used to determine the correction factors to regions with higher  $p_T$ .

- **Electron efficiency:**

Uncertainties associated with the electron efficiency SFs are provided by the egamma CP group [14] and arise from the reconstruction, ID, isolation and trigger efficiencies. They correct for the efficiency difference between data and MC [9] and are measured with a “tag-and-probe” method in  $Z \rightarrow e^+e^-$  and  $J/\psi \rightarrow e^+e^-$  events. The information on the correlation of the different components of the systematic uncertainties are provided for all efficiency measurements. The default correlation model for the uncertainties is used, which provides one up/down variation for each of the SF components separately [14, 15].

- **Muon efficiency:**

As for electrons, SFs obtained from  $Z \rightarrow \mu^+\mu^-$  and  $J/\psi \rightarrow \mu^+\mu^-$  events are applied to correct for the differences between data and MC in the muon ID, isolation and trigger efficiencies [13]. Uncertainties on these SFs are provided by the muon CP group [17] and applied as up/down variations of the nominal SFs for each component.

### 4.9.2 Theoretical uncertainties

In this section, the theoretical systematics are outlined.

- **$t\bar{t}Z$  background:**

An overall normalization uncertainty of 10% is considered for the  $t\bar{t}Z$  background. Two generic shape systematics are considered for the  $t\bar{t}Z$  background. They are constructed (see Section 4.9.3) by either applying a linear or triangular interpolation to up and down variations which are defined to be  $\pm 20\%$  from the nominal  $t\bar{t}Z$  background.

- **$ZZ$  background:**

An overall normalization uncertainty of 30% is considered for the  $ZZ$  background.

- **$t\bar{t}H$  background:**

An overall normalization uncertainty of 20% is considered for the  $t\bar{t}H$  background.

- **$tZq$  background:**

An overall normalization uncertainty of 14% is considered for the  $tZq$  background.

- **$t\bar{t}Z$  fake background:**

An overall normalization uncertainty of 50% is considered for the  $t\bar{t}Z$  fake background.

- **other background processes:**

The ‘other’ background consists of many processes which have minimal but non-negligible contribution in the signal regions (See Table 4.4). An overall normalization uncertainty of 30% is considered for the ‘other’ background processes.

- **$tWZ$ :** A modelling uncertainty on  $tWZ$  is considered by comparing the nominal sample (using the DR1 scheme) and a minimal DR2 sample.

Two generic shape systematics are considered for the  $tWZ$  background. They are constructed (see Section 4.9.3) by either applying a linear or triangular interpolation to up and down variations which are defined to be  $\pm 20\%$  from the nominal  $tWZ$  background.

### 4.9.3 Generic shape systematics

It is evident that the tetralepton channel is statistically limited. We therefore expect that the uncertainty on  $u_{tWZ}$  is dominated by statistical uncertainty and that the impact of shape systematics will be negligible in comparison.

In order to include shape uncertainties related to the modelling of our samples, we construct generic shape systematics for any given sample process. Given that we choose a sufficiently large set of values for which the systematics can take in the fit, the constructed systematics could represent many shape systematics which we have not yet considered to include in the fitting procedure.

We start by constructing an envelope (error bars) consisting of two MC templates. One with the nominal MC template increased by 20% on its normalisation and the other with the nominal MC template decreased by 20% on its normalisation. The templates are then modified from their original shape either by doing linear interpolation (from the leftmost-up variation to the rightmost-down variation) or triangular interpolation (shape is set to zero at the rightmost and leftmost parts and reaches the envelope in the middle). The linear and triangular interpolation is done using TRF’s `ForceShape` option [49], which alters the original templates (as described above). This envelope now represents the bounds which the systematic can vary in the fit.

In Figure 4.48 the envelope before and after the shape change, for both the linear and triangular interpolations, for the  $t\bar{t}Z$  background in the  $t\bar{t}Z$  CR is shown.

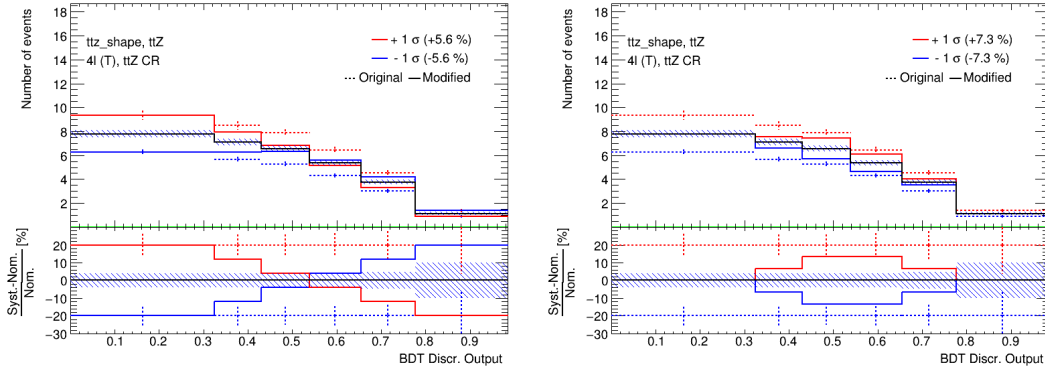


Figure 4.48:  $t\bar{t}Z$  generic shape systematic before (original) and after (modified) linear (left) and triangular (right) interpolation in the  $t\bar{t}Z$  CR is shown. The output from the event-level BDT shown on the x-axis. In the upper panel, the number of events is shown on the y-axis. In the lower panel, the difference between the systematic variation (the envelope’s templates) and the nominal template, divided by the nominal template, is shown on the y-axis. The nominal  $t\bar{t}Z$  template is shown by the solid black lined histogram, with the diagonal lined bands representing its total uncertainty. The templates of the upper and lower envelopes (before modification) is given by the dotted red and blue lined histograms respectively. The templates of the upper and lower envelopes (after modification) is given by the solid red and blue lined histograms respectively, with the vertical dotted lines representing its total uncertainty.

We consider two shape systematics (linear and triangular shapes) for  $tWZ$  and the most dominant background processes across both channels. In particular, we consider these shape systematics for  $t\bar{t}Z$  for both the tri- and tetralepton channels. Additionally, we consider these shape systematics for the  $WZ + b$  and  $WZ + c$  backgrounds in the trilepton channel.

## 4.10 Analysis Pipeline and TRexFitter

We make use of industry standard ROOT<sup>3</sup> wrappers in this analysis, namely, PyROOT and TRexFitter.

<sup>3</sup>CERN’s HEP data analysis framework (written in C++)

Python is used extensively in many fields of science (not limited to physics and data science) due to its simplicity and ongoing support by the communities which utilize it. PyROOT allows users to access the full ROOT functionality within Python. More specifically, PyROOT provides Python bindings for ROOT.

**TRExFitter** is a framework for binned template profile likelihood fits[54]. In this analysis, we used TRExFitter (tag: `TRExFitter-00-04-13`) to produce all pre-fit and post-fit plots (including fit statistics, e.g. limit, significance,  $\mu_{best-fit}$ ).

The analysis pipeline starts with sample derivations (derived dataset) being submitted to the grid for ntuple production. This applies cuts and selections to the already reduced derivations and produces ntuples with trees containing variables (e.g. scale factors, observables, MC truth flags) that will be used at future stages in the analysis. These ntuples are then read by PyROOT where the events are looped over, before being written to ROOT files as input to **TRExFitter**. The Python scripts are used to define the different regions and apply the final cuts and selections outlined in Table 4.3. In addition to this purpose, they are used to train the two BDTs and to produce the output from these trained BDTs. As each event is looped over, the cuts and selection criteria are checked for the given event and is either thrown away (if the event does not pass the selection criteria), or gets written to a ROOT file (if the event passes the selection criteria) corresponding to the MC sample and Run 2 data-set (`mc16a`, `mc16d`, `mc16e`) which it belongs to. These ROOT files contain all observables, weights and scale factors (corresponding to an event) which we wish to use in **TRExFitter**. **TRExFitter** then takes these files as input, runs a maximum likelihood fit and produces relevant plots (e.g. pre-fit, post-fit, pull plots) and statistical parameters (e.g. limit, significance,  $\mu_{best-fit}$ ).

#### 4.10.1 Fitting Procedure

Using the TRExFitter framework, binned profile-likelihood fits are performed to determine the signal strength  $\mu_{tWZ} = \sigma_{obs}(tWZ)/\sigma_{SM}(tWZ)$  of  $tWZ$  production. A fit across all regions in the tetralepton channel is performed to determine the sensitivity  $tWZ$  in this channel. In Section 4.11.2, a combined fit is performed across all regions in the trilepton and tetralepton channels to take advantage of the sensitivity of  $tWZ$  in both channels in order to further boost the sensitivity of  $tWZ$ .

In the separate and combined fits, the *mixed data and MC* fit setup [55] is used. This is done to obtain the most accurate prediction of the expected results while keeping the signal regions blinded. For this setup, first a background-only fit to the control regions using real data is done to determine estimates of the nuisance parameters. Then these estimates are used to construct a modified ASIMOV dataset in the signal regions. Finally, the fit is performed using real data in the control regions and the aforementioned modified ASIMOV data-set in the signal regions.

In these fits, the parameter of interest (POI) is  $\mu_{tWZ}$ . The POI is ultimately the quantity which we wish to measure and is set as a free parameter (unconstrained; can take any value in the fit). The nuisance parameters are assigned to the systematic uncertainties outlined in 4.9. Furthermore, a gamma ( $\gamma$ ) nuisance parameter for a bin is added to the likelihood function if the statistical uncertainty in the bin exceeds 0.1% of its nominal value.

Pruning is done per sample and per region on the shape and normalisation uncertainties for samples. A sample's shape and normalisation nuisance parameter is pruned (removed from the limit/fit) if the fraction of signal yield to the total yield (signal + background) is less than 0.01.

An auto-binning algorithm, **TransfoD** [21], was used to define the binning. This aims to maximise  $\frac{signal}{background}$  in each bin. Furthermore, it aims to avoid defining bins with a low number of events.

## 4.11 Results

In the section, an expected upper limit and an expected significance are set on the cross section of  $tWZ$ . This is performed for the current analysis in the tetralepton channel as well as for a combined analysis across the trilepton and tetralepton channels. The trilepton analysis was performed as an independent study by Benjamin Warren (UCT). Note that throughout this section, all signal regions remain blinded.

### 4.11.1 Tetralepton Channel

In Figure 4.49 pre-fit distributions for the variables used in the likelihood fit in each region are shown.

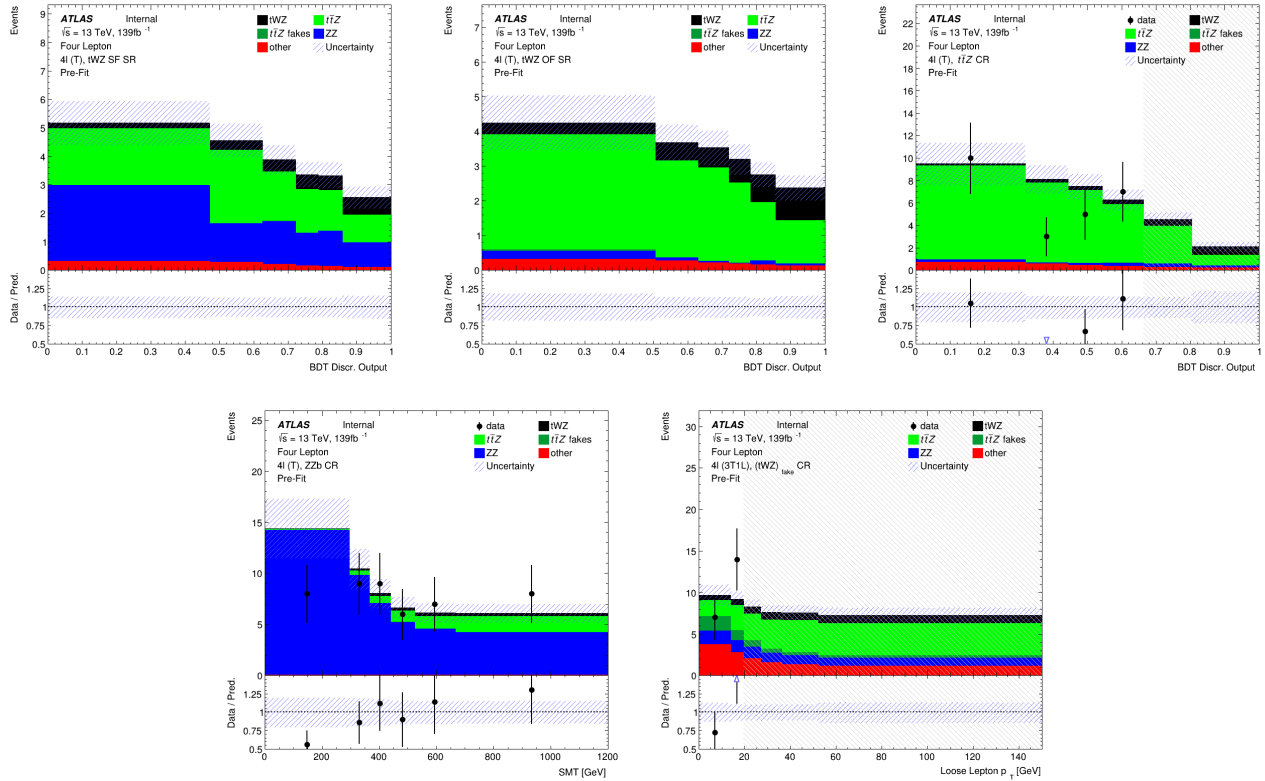


Figure 4.49: Pre-fit distributions (blinded) of variables used in the fit are shown. The data is given by the black points and the MC predictions for each process are given by the histograms. The vertical lines on the data points represent the total uncertainty in the data and the diagonal lined bands represent the total MC uncertainty. The lower panel in each plot shows the ratios of the data to the theoretical predictions. The plots in the  $tWZ$  OF SR and  $tWZ$  SF SR are kept blinded by omitting the data points. **Top left:** The event-level BDT Disc. Output in the  $tWZ$  SF (4T) SR region is shown. **Middle Top:** The event-level BDT Disc. Output in the  $tWZ$  SF (4T) SR region is shown. **Top right:** The event-level BDT Disc. Output in the  $tt\bar{Z}$  CR region is shown. **Bottom left:**  $SMT = \sum p_T(\ell) + \sum p_T(jet) + E_T^{\text{miss}}$  in the  $ZZb$  CR is shown. **Bottom right:**  $p_T$  (loose lepton) in the  $(tWZ)$  fake (3T1L) CR is shown.

In Figure 4.50 pre-fit distributions for the variables used in the likelihood fit in each region are shown.

In Table 4.10, the post-fit yields for each sample in each region is shown.

The expected upper limit of  $tWZ$  in the tetralepton channel is measured as,

$$\mu_{up}^{exp} = 1.61^{+2.35}_{-1.16} \quad (4.15)$$

The expected significance of  $tWZ$  in the tetralepton channel is measured as,

$$Z_\mu^{exp} = 1.44\sigma \quad (4.16)$$

The best-fit value of the signal strength,  $\mu(tWZ) = \frac{\sigma(tWZ)}{\sigma(tWZ)_{SM}}$ , from the likelihood fit is measured as,

$$\mu(tWZ) = 1.91^{+0.95}_{-0.82} \quad (4.17)$$

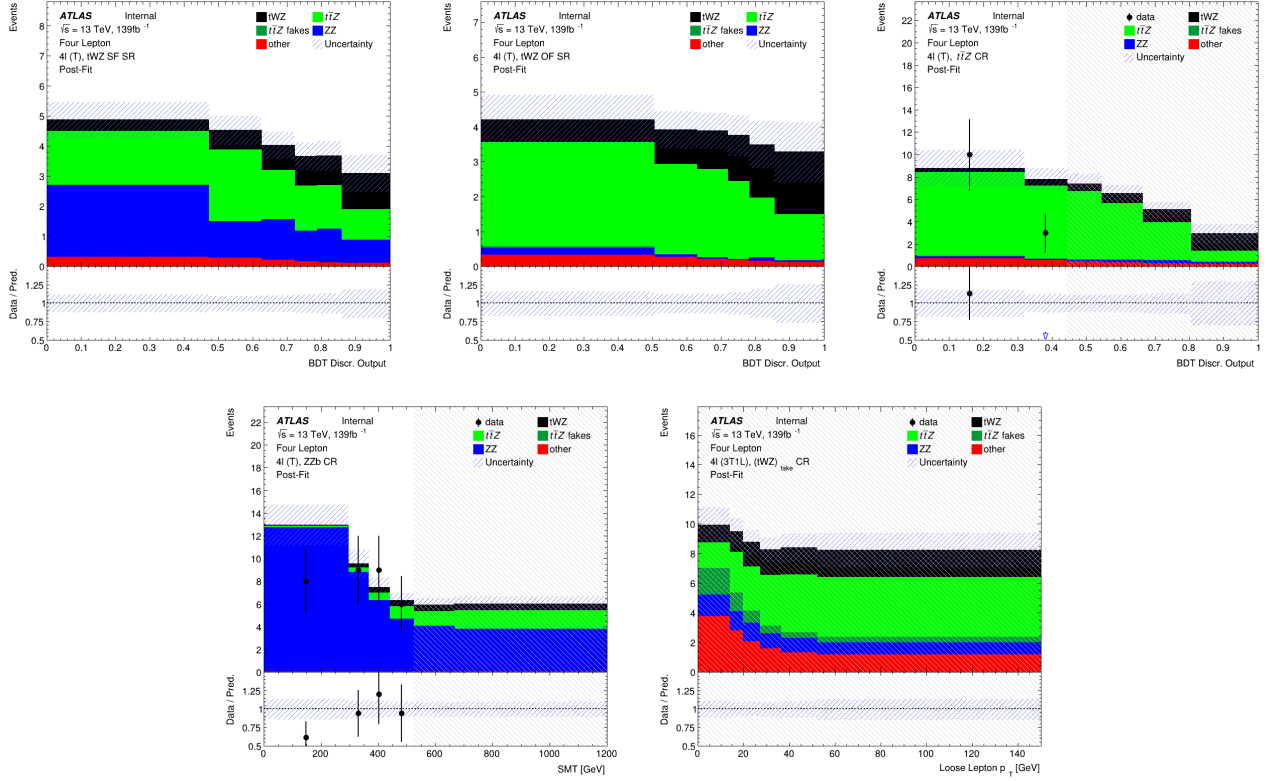


Figure 4.50: Post-fit distributions (blinded) of variables used in the fit are shown. The data is given by the black points and the MC predictions for each process are given by the histograms. The vertical lines on the data points represent the total uncertainty in the data and the diagonal lined bands represent the total MC uncertainty. The lower panel in each plot shows the ratios of the data to the theoretical predictions. The plots in the  $tWZ$  OF SR and  $tWZ$  SF SR are kept blinded by omitting the data points. **Top left:** The event-level BDT Disc. Output in the  $tWZ$  SF (4T) SR region is shown. **Middle Top:** The event-level BDT Disc. Output in the  $tWZ$  SF (4T) SR region is shown. **Top right:** The event-level BDT Disc. Output in the  $t\bar{t}Z$  CR region is shown. **Bottom left:**  $SMT = \sum p_T(\ell) + \sum p_T(jet) + E_T^{\text{miss}}$  in the  $ZZb$  CR is shown. **Bottom right:**  $p_T$ (loose lepton) in the  $(tWZ)_{\text{fake}}$  (3T1L) CR is shown.

	$tWZ$ OF SR	$tWZ$ SF SR	$t\bar{t}Z$ CR	$ZZb$ CR	$(tWZ)_{\text{fake}}$ CR	
$t\bar{t}Z$	$13.2379 \pm 1.52295$	$9.62061 \pm 1.12291$	$29.9054 \pm 3.60908$	$5.08899 \pm 0.620121$	$18.5393 \pm 2.23036$	
$t\bar{t}Z$ fakes	$0.0702522 \pm 0.0468691$	$0.0334067 \pm 0.0256903$	$0.0723509 \pm 0.0418526$	$0.0485273 \pm 0.029133$	$5.04378 \pm 2.34732$	
$tWZ$	$7.83414 \pm 3.31679$	$5.33547 \pm 2.24801$	$5.69373 \pm 2.58041$	$2.89889 \pm 1.23837$	$10.278 \pm 4.3345$	
$ZZ$	$0.481776 \pm 0.119774$	$7.72372 \pm 1.2351$	$1.07955 \pm 0.182461$	$40.6067 \pm 6.26078$	$6.86097 \pm 1.11443$	
other	$tt$ $tZq$ $t\bar{t}W$ $WZ$ $t\bar{t}t$ $t\bar{t}\bar{t}$ $t\bar{t}WW$ $VVV(V = W/Z)$ $t\bar{t}H$	$6.00553e-06 \pm 0.02819e-06$ $0.0827905 \pm 0.0398773$ $0.00668643 \pm 0.00792217$ $0.0442934 \pm 0.024156$ $0.000987164 \pm 0.000766266$ $0.00934035 \pm 0.0080554$ $0.0294618 \pm 0.0263174$ $0.280643 \pm 0.0853411$ $0.846054 \pm 0.175495$	$0.252557 \pm 0.442116$ $0.0756107 \pm 0.0354584$ $0.00279748 \pm 0.00287361$ $0.0396511 \pm 0.0154282$ $0.00247481 \pm 0.00136945$ $0.0107458 \pm 0.00849984$ $0.029771 \pm 0.0195582$ $0.191433 \pm 0.0586778$ $0.669375 \pm 0.140107$	$0.273507 \pm 0.223201$ $0.063585 \pm 0.0293325$ $6.00553e-06 \pm 0.02819e-06$ $0.0133471 \pm 0.0128199$ $0.0140869 \pm 0.00479496$ $0.0571373 \pm 0.0204011$ $0.264364 \pm 0.0926252$ $0.0697266 \pm 0.0225059$ $1.96662 \pm 0.401199$	$6.00553e-06 \pm 0.02819e-06$ $0.055884 \pm 0.0244084$ $0.002306 \pm 0.00564349$ $0.0472562 \pm 0.0330315$ $6.00553e-06 \pm 0.02819e-06$ $6.00553e-06 \pm 0.02819e-06$ $0.0129431 \pm 0.0323803$ $0.171142 \pm 0.0518102$ $0.150025 \pm 0.0353826$	$2.35427 \pm 0.917112$ $4.90963 \pm 0.745354$ $0.943182 \pm 0.292148$ $1.83567 \pm 0.392459$ $0.0100558 \pm 0.00363157$ $0.0216809 \pm 0.00992819$ $0.152448 \pm 0.058965$ $0.266502 \pm 0.0810194$ $2.21264 \pm 0.451623$
Total	$22.9243 \pm 2.96284$	$23.9876 \pm 2.11249$	$39.4734 \pm 3.44937$	$49.0856 \pm 6.04162$	$53.4282 \pm 4.31683$	
data	-	-	36	49	57	

Table 4.10: The post-fit yields for each sample in each region is shown.

The expected upper limit is in agreement with the extracted best-fit value on the signal strength, therefore no deviations from the SM cross section of  $tWZ$  is observed. Neither the  $3\sigma$  evidence nor the  $5\sigma$  discovery standards are reached for the expected significance. This is not surprising, given the low amount of events present in the tetralepton channel.

In Figure 4.51, a ranking plot showing the impact of the systematic uncertainties on the POI,  $\mu(tWZ)$  is shown.

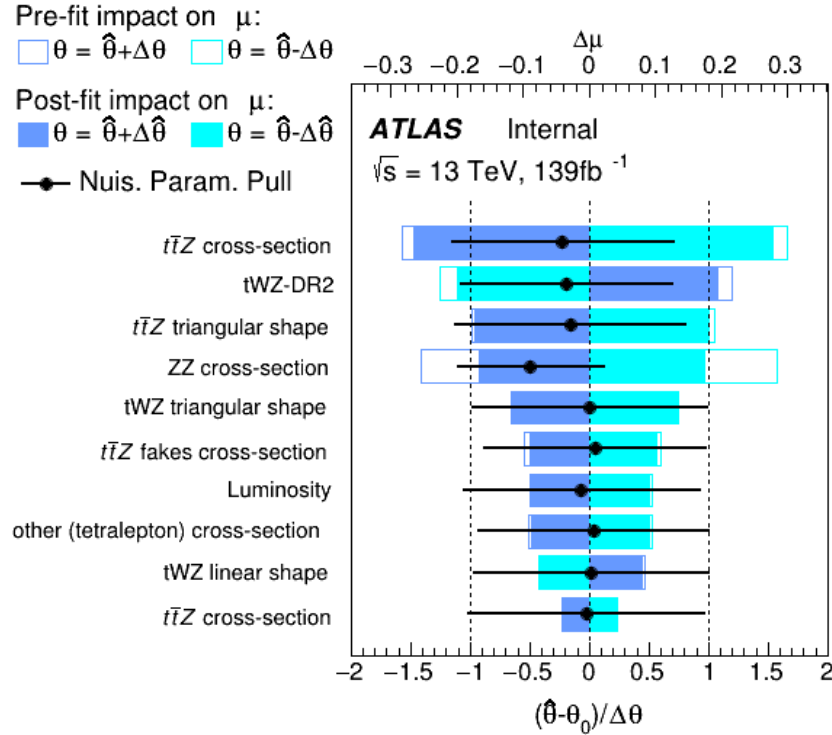


Figure 4.51: A ranking plot showing the impact (ordered from top to bottom via decreasing impact) of the systematic uncertainties (top 10) on the POI,  $\mu(tWZ)$ , in the tetralepton channel is shown.  $\hat{\theta}$  is the best-fit value of the nuisance parameter.  $\Delta\hat{\theta}$  and  $\Delta\theta$  are the post-fit and pre-fit uncertainties respectively. The post-fit and pre-fit impact of each nuisance parameter on  $\mu(tWZ)$  are shown with the solid and lined rectangles respectively. The empty and solid blue rectangles correspond to the pre-fit and post-fit impacts on  $\mu(tWZ)$  respectively. These impacts are shown on the upper axis ( $\Delta\mu$ ). On the lower axis, the nuisance parameter pull,  $\frac{\hat{\theta} - \theta_0}{\Delta\theta}$ , is shown ( $\theta_0$  is the nominal pre-fit value of the nuisance parameter). The nuisance parameter pull is indicated by the black points, with their relative post-fit errors ( $\frac{\Delta\hat{\theta}}{\Delta\theta}$ ) shown by the black horizontal error bars.

The most important systematics are the cross sections of  $t\bar{t}Z$  and  $ZZ$ , and shape modelling on  $t\bar{t}Z$  ( $t\bar{t}Z$  triangular

shape) and  $tWZ$  ( $tWZ$ -DR2 and  $tWZ$  triangular shape). The cross section of  $ZZ$  is significantly shifted down in the fit from its nominal value. The  $t\bar{t}Z$  cross section,  $tWZ$ -DR2 and  $t\bar{t}Z$  triangular shape nuisance parameters are similarly shifted down in the fit from their nominal values, but to a much lesser degree than the cross section of  $ZZ$ . These pulls are all within  $1\sigma$  uncertainty and are thus relatively small. It is expected that the modelling uncertainties (shape and normalisations) of the most dominant backgrounds (e.g.  $t\bar{t}Z$ ,  $ZZ$ ) have relatively large impacts on  $\mu(tWZ)$ , since the uncertainty of the analysis is dominated by statistical uncertainty.

#### 4.11.2 Trilepton and Tetralepton Channels

In the section, an expected upper limit and an expected significance are set on the cross section of  $tWZ$  from the combined fit across all regions of  $tWZ$  in the tetralepton and trilepton channels.

The trilepton analysis follows a similar analysis strategy to that of the tetralepton analysis. It includes an event-level BDT which aims to discriminate between the  $tWZ$  and all background as well as an object-level BDT which aims to identify hadronically decaying  $W$  bosons to discriminate between  $tWZ$  and the large  $WZ$  background. One  $tWZ$  SR is defined and five CRs are defined.  $WZ$  and  $t\bar{t}Z$  CRs are defined to constrain the dominant  $WZ$  and  $t\bar{t}Z$  backgrounds. Three CRs which require that one of the three selected leptons are loose, are defined for  $WZ$ ,  $t\bar{t}Z$  and  $tWZ$  in order to constraint the fake lepton component (using the MC template method - similar to the method used in Section 4.6 to estimate the fake lepton component).

The expected upper limit of  $tWZ$  in the trilepton channel is measured as,

$$\mu_{up}^{exp} = 2.65^{+3.67}_{-1.91} \quad (4.18)$$

The expected significance of  $tWZ$  in the trilepton channel is measured as,

$$Z_\mu^{exp} = 0.75\sigma \quad (4.19)$$

The best-fit value of the signal strength,  $\mu(tWZ) = \frac{\sigma(tWZ)}{\sigma(tWZ)_{SM}}$ , from the likelihood fit is measured as,

$$\mu(tWZ) = 1.16^{+1.33}_{-1.30} \quad (4.20)$$

The expected upper limit is in agreement with the extracted best-fit value on the signal strength, therefore no deviations from the SM cross section of  $tWZ$  is observed.

In Table 4.11, the nuisance parameters used in the fit, including which channel's regions are affected by each, are shown.

The expected upper limit of  $tWZ$  across both channels is measured as,

$$\mu_{up}^{exp} = 1.43^{+2.04}_{-1.03} \quad (4.21)$$

The expected significance of  $tWZ$  across both channels is measured as,

$$Z_\mu^{exp} = 1.61\sigma \quad (4.22)$$

The best-fit value of the signal strength,  $\mu(tWZ) = \frac{\sigma(tWZ)}{\sigma(tWZ)_{SM}}$ , from the likelihood fit is measured as,

$$\mu(tWZ) = 1.80^{+0.70}_{-0.65} \quad (4.23)$$

In Figure 4.52, the expected upper limits of the trilepton channel, tetralepton channel and both channels combined are shown.

It can be seen that the sensitivity of  $tWZ$  is mostly driven by the tetralepton analysis, with the trilepton analysis attributing a small decrease in the expected upper limit of the combined analysis, and its associated uncertainty.

In Figure 4.53, the best-fit values of  $\mu(tWZ)$  from the fit for the trilepton channel, tetralepton channel and both channels combined are shown.

Nuisance Parameter	Channel Affected	
	trilepton	tetralepton
$\sigma(t\bar{t}H)$	✓	✓
$\sigma(t\bar{t}Z)$	✓	✓
$\sigma(WZ)$	✓	✓
$\sigma(tZq)$	✓	✓
$\sigma(ZZ)$	✓	✓
$\sigma(\text{other(trilepton)})$	✓	✗
$\sigma(\text{other(tetralepton)})$	✗	✓
$\sigma(t\bar{t}Z)_{\text{fakes}}$	✗	✓
$\sigma(t\bar{t})_{\text{fakes}}$	✓	✗
$\sigma(Z + \text{jets})_{\text{fakes}}$	✓	✗
Luminosity	✓	✓
$jvt$	✓	✓
pileup	✓	✓
DL1r SF (b jets)	✓	✓
DL1r SF (light jets)	✓	✓
$\sigma(tWZ - DR2)$	✗	✓
lepton SF	✓	✓
$t\bar{t}Z$ triangular shape	✓	✓
$t\bar{t}Z$ linear shape	✓	✓
$WZ + b$ triangular shape	✓	✗
$WZ + b$ linear shape	✓	✗
$WZ + c$ triangular shape	✓	✗
$WZ + c$ linear shape	✓	✗

Table 4.11: A summary of the nuisance parameters used in the combined fit is shown. The channels which are affected by each nuisance parameter are indicated with a ✓ (is affected) or a ✗ (is not affected).

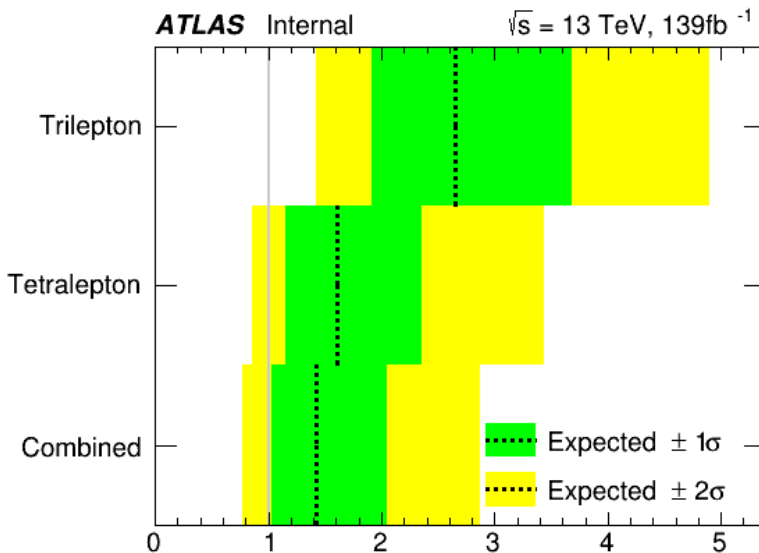


Figure 4.52: The expected upper limits of the trilepton channel, tetralepton channel and both channels combine are shown. The y-axis shows the channels in which the fitting procedure was performed. The expected limits are represented by the vertical dotted line. One- and two-  $\sigma$  uncertainty bands are shown in green and yellow respectively. The vertical grey line indicates when  $\mu(tWZ) = 1$ .

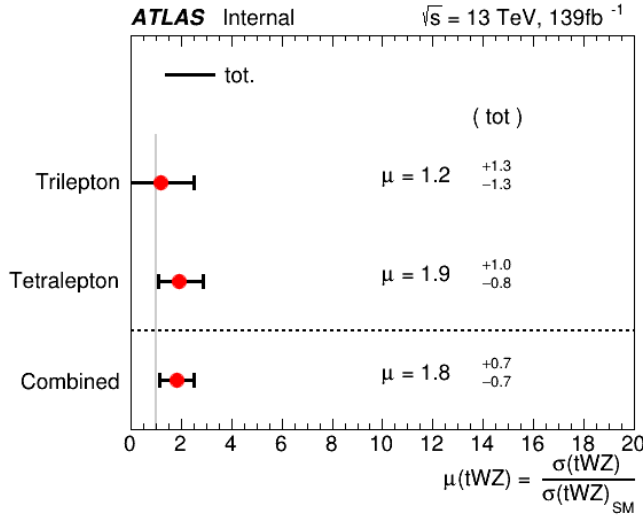


Figure 4.53: The best-fit values of  $\mu(tWZ)$  from the fit for the trilepton channel, tetralepton channel and both channels combined are shown. The y-axis shows the channels in which the fitting procedure was performed. The signal strength  $\mu(tWZ)$  is shown on the x-axis. The nominal signal strengths are represented by the red dots. The total uncertainty associated with the best-fit  $\mu(tWZ)$  value is shown by the black error bars.

It can be seen from Figures 4.52 and 4.53 that the best fit value for the signal strength on  $tWZ$ ,  $\mu(tWZ)$ , and the expected limits for the tri- and tetralepton channels are consistent with one-another (their uncertainties overlap). Therefore it is appropriate to combine these two analyses.

In Figure 4.54, a ranking plot showing the impact of the systematic uncertainties on the POI,  $\mu(tWZ)$ , in the combined fit across both the tri- and tetralepton channels is shown.

Some nuisance parameters are pulled down from their nominal pre-fit values, however these are all within  $1\sigma$  uncertainty and are thus relatively small. It is expected that the modelling uncertainties (shape and normalisations) of the most dominant backgrounds (e.g.  $t\bar{t}Z$ ,  $ZZ$ ,  $WZ$ ) have relatively large impacts on  $\mu(tWZ)$ , since the uncertainty of the analysis is dominated by statistical uncertainty.

The most important systematics are the cross sections of  $t\bar{t}Z$ ,  $ZZ$  and  $WZ + b$ , and shape modelling on  $t\bar{t}Z$  ( $t\bar{t}Z$  triangular shape). The aforementioned nuisance parameters are significantly shifted down in the fit from its nominal value. The less important systematics are pulled in the fit from their nominal values, but to a much lesser degree than the cross section of those mentioned above. It is expected that the modelling uncertainties (shape and normalisations) of the most dominant backgrounds (e.g.  $t\bar{t}Z$ ,  $ZZ$  and  $WZ + b$ ) have relatively large impacts on  $\mu(tWZ)$ , since the uncertainty of the analysis is dominated by statistical uncertainty.

#### 4.11.2.1 Projection to Higher Luminosity

In this section we apply a fully blinded fit to the ASIMOV dataset for integrated luminosities larger than the  $139\text{fb}^{-1}$  currently available from the ATLAS Full Run 2 dataset. This study gives us insight into the sensitivity of  $tWZ$  which we could expect if we were to replicate the current analysis, given more data. Given the upgrades planned for the LHC and the ATLAS detector, we will soon expect a large increase in available  $p - p$  collision data (reaching  $\mathcal{L} = 3000\text{fb}^{-1}$  [23]). This study therefore gives us an idea of the sensitivity of  $tWZ$  which we can expect in the future.

In Figure 4.55, the expected upper limit and significance for combined fully blinded fits to the ASIMOV dataset across both the tri- and tetralepton channels for a range integrated luminosities are shown.

As we increase the total integrated luminosity, the sensitivity of  $tWZ$  increases. The increase in sensitivity is shown

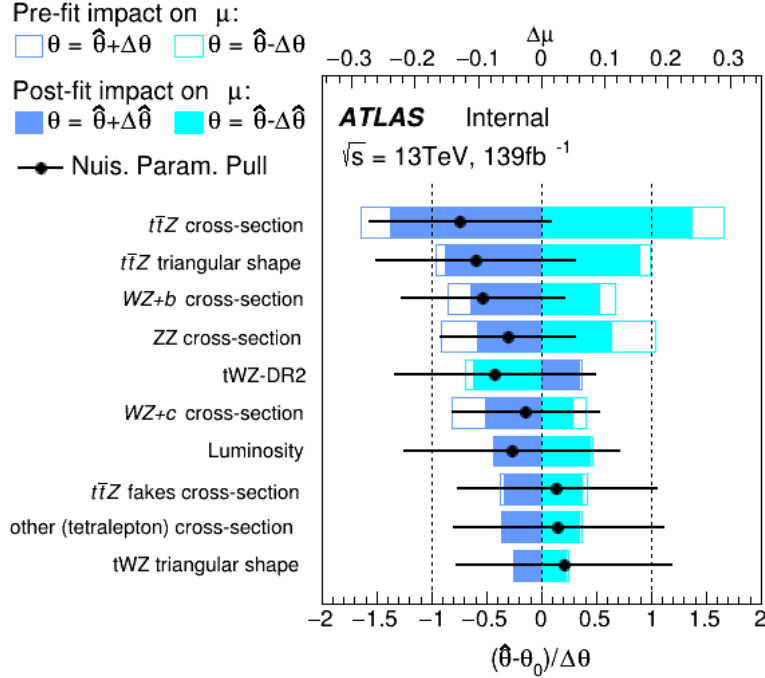


Figure 4.54: A ranking plot showing the impact of the systematic uncertainties (top 10) on the POI,  $\mu(tWZ)$ , in the combined fit across both the tri- and tetralepton channels is shown.  $\hat{\theta}$  is the best-fit value of the nuisance parameter.  $\Delta\hat{\theta}$  and  $\Delta\theta$  are the post-fit and pre-fit uncertainties respectively. The post-fit and pre-fit impact of each nuisance parameter on  $\mu(tWZ)$  are shown with the solid and lined rectangles respectively. The empty and solid blue rectangles correspond to the pre-fit and post-fit impacts on  $\mu(tWZ)$  respectively. These impacts are shown on the upper axis ( $\Delta\mu$ ). On the lower axis, the nuisance parameter pull,  $\frac{\hat{\theta} - \theta_0}{\Delta\theta}$ , is shown ( $\theta_0$  is the nominal pre-fit value of the nuisance parameter). The nuisance parameter pull is indicated by the black points, with their relative post-fit errors ( $\frac{\Delta\hat{\theta}}{\Delta\theta}$ ) shown by the black horizontal error bars.

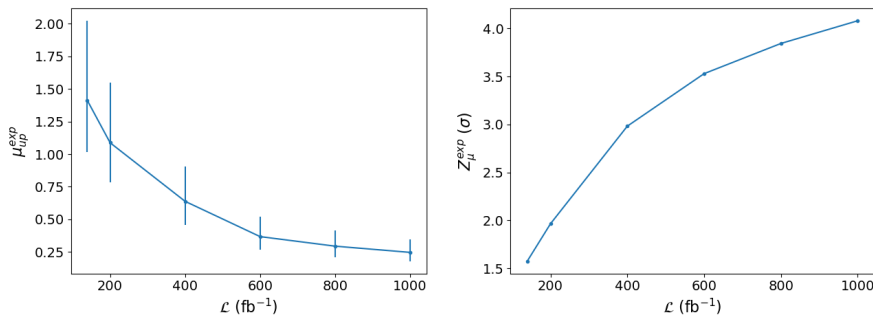


Figure 4.55: The expected upper limit (left) and significance (right) for combined fully blinded fits to the ASIMOV dataset across both the tri- and tetralepton channels for a range of integrated luminosities are shown. **Left:** The integrated luminosity,  $\mathcal{L}$ , is shown on the x-axis. The expected upper limit,  $\mu_{up}^{exp}$ , is shown on the y-axis. The vertical lines represent the total uncertainty ( $\pm 1\sigma$ ) on the expected upper limit. **Right:** The integrated luminosity,  $\mathcal{L}$ , is shown on the x-axis. The expected significance,  $Z_\mu^{exp}$ , is shown on the y-axis. The vertical lines represent the total uncertainty ( $\pm 1\sigma$ ) on the expected significance.

by the decrease of the expected upper limit and the increase of the expected significance with increasing integrated luminosity. It can be noted that a  $3\sigma$  expected significance is achieved at  $\mathcal{L} \sim 400 \text{ fb}^{-1}$ , indicating evidence for observation of  $tWZ$ . The  $5\sigma$  significance 'discovery' standard is above our  $1000 \text{ fb}^{-1}$  luminosity range of study. Furthermore, these plots show that the sensitivity of  $tWZ$  is hindered by the low amount of events we observe, rather than the systematic effects. This is evident since increasing the luminosity, therefore increasing the number of events we see in the detector, directly causes a steady increase in sensitivity.

# Chapter 5

## Conclusion and Outlook

The search for  $tWZ$  production using  $139 \text{ fb}^{-1}$  of  $pp$  collision data at  $\sqrt{s} = 13 \text{ TeV}$ , recorded by the ATLAS experiment at CERN, has been presented. This thesis targeted the tetralepton final state channel. To further increase the sensitivity of  $tWZ$ , a combined analysis was done across the tetralepton and trilepton (studied in an independent analysis by Benjamin Warren (UCT) [56]) channels.

Two SRs and Three CRs were defined. Two SRs, instead of one, were defined in order to suppress and constrain the  $ZZ$  background. The definition of the  $tWZ$  OF SR and the  $tWZ$  SF SR take advantage of the OSSF lepton pairs which originate from the decay of a  $Z$  boson, by requiring that non- $Z$  leptons in the event have the opposite and same flavours, for the  $tWZ$  OF SR and  $tWZ$  SF SR respectively. The resulting SRs successfully separate the  $ZZ$  background, with the  $tWZ$  OF SR containing around 6% of the total  $ZZ$  background yield across both regions (implying that the remaining  $\sim 94\%$  is contained in the  $tWZ$  SF SR). The dominant background processes,  $t\bar{t}Z$  and  $ZZ$  were constrained by the definition of  $t\bar{t}Z$  and  $ZZ$  CRs, respectively. The dominant source of fake leptons, originating from the  $t\bar{t}Z$  background, was constrained by the  $(tWZ)_{fake}$  CR, using the MC template method.

Two BDTs were implemented: an object-level BDT which aims to classify between  $\ell b$  systems coming from top quarks and an event-level BDT which aims to discriminate between  $tWZ$  and our major backgrounds,  $t\bar{t}Z$  and  $ZZ$ . The output from the object-level BDT was converted to an event-level variable to be used as input to the event-level BDT. A kinematic reconstruction algorithm,  $2\nu\text{SM}$ , was used to reconstruct top quarks in order to discriminate between  $tWZ$  and  $t\bar{t}Z$ . The output from this algorithm was used as an input variable to the event-level BDT. The trained BDT was shown to discriminate well between signal and background events, with a separation of \*\*\*\*\*.

Using a modified ASIMOV dataset in the SRs and real data in the CRs, a blinded maximum-likelihood fit was performed across all regions in the tetralepton channel. The best-fit value of the signal strength in the tetralepton channel was,

$$\mu(tWZ) = 1.91^{+0.95}_{-0.82} \quad (5.1)$$

and an expected significance of  $1.44\sigma$ . The expected upper limit on the signal strength of  $tWZ$  in the tetralepton channel was,

$$\mu_{up}^{exp} = 1.61^{+2.35}_{-1.16} \quad (5.2)$$

Furthermore, a blinded maximum-likelihood fit was performed across all regions across the trilepton and tetralepton channels. The best-fit value of the signal strength across both the trilepton and tetralepton channels were,

$$\mu(tWZ) = 1.80^{+0.70}_{-0.65} \quad (5.3)$$

and an expected significance of  $1.61\sigma$ . The expected upper limit on the signal strength of  $tWZ$  across both the trilepton and tetralepton channels were,

$$\mu_{up}^{exp} = 1.43^{+2.04}_{-1.03} \quad (5.4)$$

Although this result does not satisfy the  $3\sigma$  evidence nor the  $5\sigma$  discovery standards, this is the tightest ever constraint on the  $tWZ$  process. The results in this analysis are heavily statistically limited, we therefore expect

that future analyses of this process, using larger datasets (such as that from the HL-LHC), would significantly improve the results.

# Appendix A

## Appendix

### A.1 Pre-Fit Plots

#### A.1.1 $tWZ$ OF SR

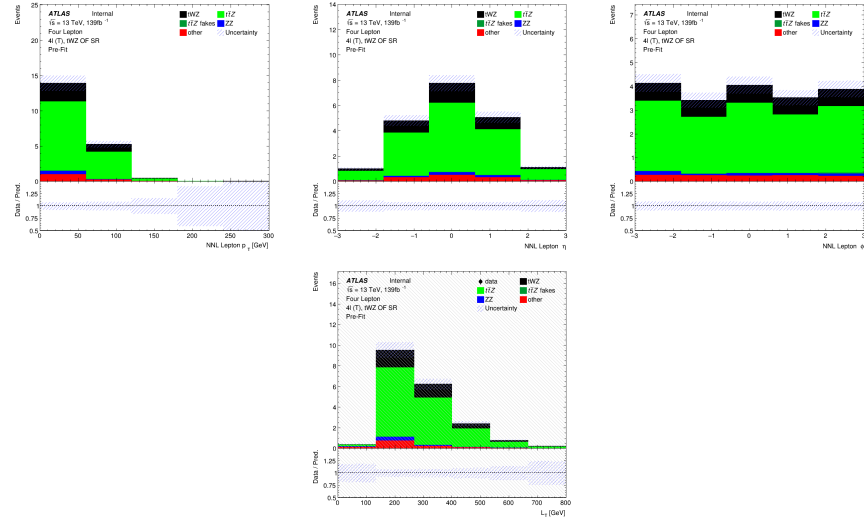


Figure A.1: Top row: MC predictions for  $p_T$ ,  $\eta$  and  $\phi$  for next-to-next-to-leading (NNL) leptons in the  $tWZ$  OF SR region (*blinded*). Bottom row: MC predictions for  $L_T$  (scalar sum of lepton  $p_T$ ) in the  $tWZ$  OF SR region (*blinded*)

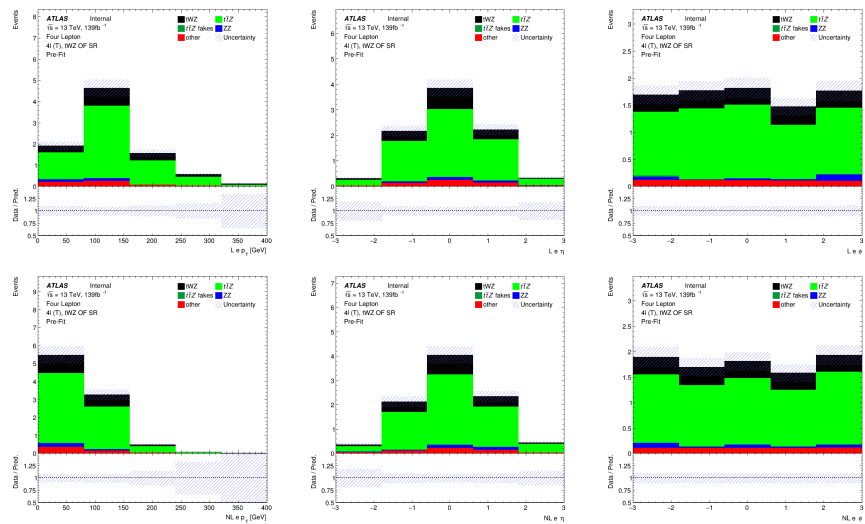


Figure A.2: MC predictions for  $p_T$ ,  $\eta$  and  $\phi$  for leading (L) electrons (top row) and next-to-leading (NL) electrons (bottom row) in the  $tWZ$  OF SR region (*blinded*)

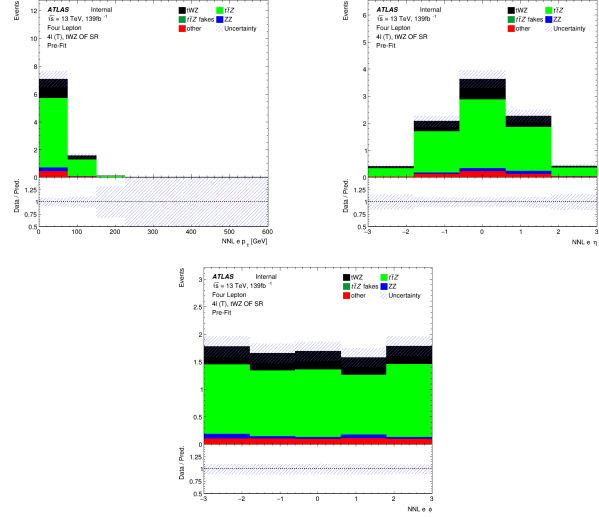


Figure A.3: MC predictions for  $p_T$ ,  $\eta$  (top row) and  $\phi$  (bottom row) for next-to-next-to-leading (NNL) electrons in the  $tWZ$  OF SR region

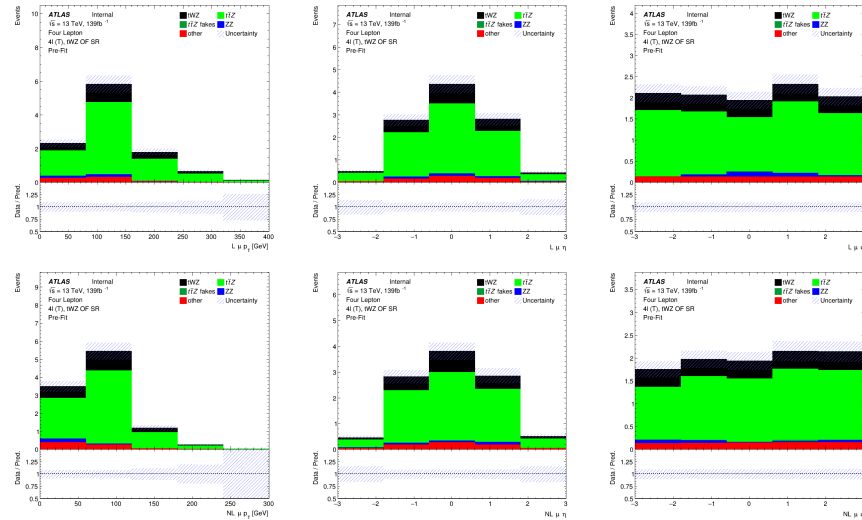


Figure A.4: MC predictions for  $p_T$ ,  $\eta$  and  $\phi$  for leading (L) muons (top row) and next-to-leading (NL) muons (bottom row) in the  $tWZ$  OF SR region (*blinded*)

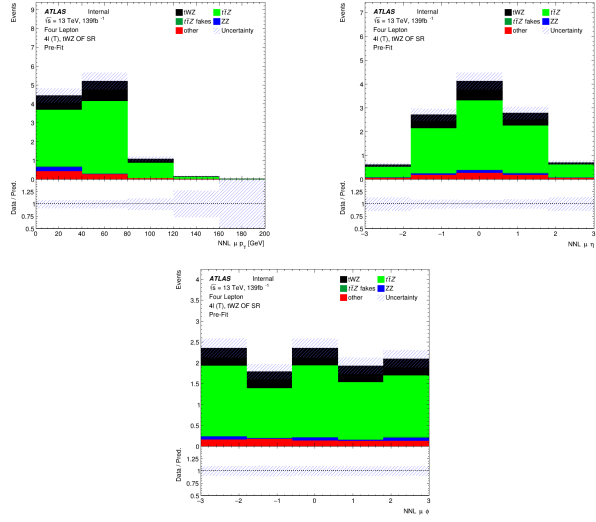


Figure A.5: MC predictions for  $p_T$ ,  $\eta$  (top row) and  $\phi$  (bottom row) for next-to-next-to-leading (NNL) muons in the  $tWZ$  OF SR region (*blinded*)

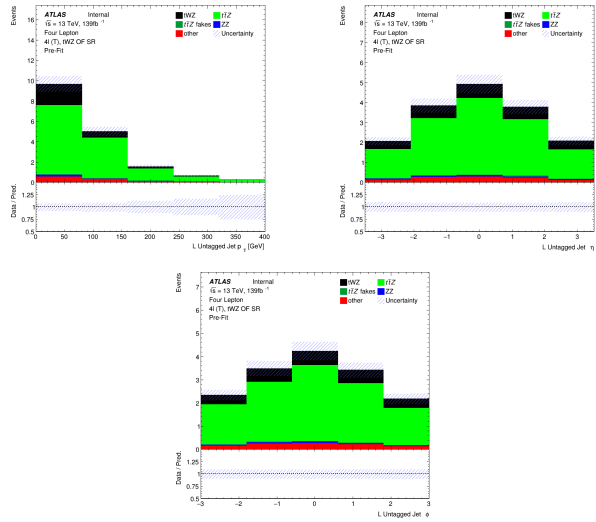


Figure A.6: MC predictions for  $p_T$ ,  $\eta$  (top row) and  $\phi$  (bottom row) for untagged jets in the  $tWZ$  OF SR region (*blinded*)

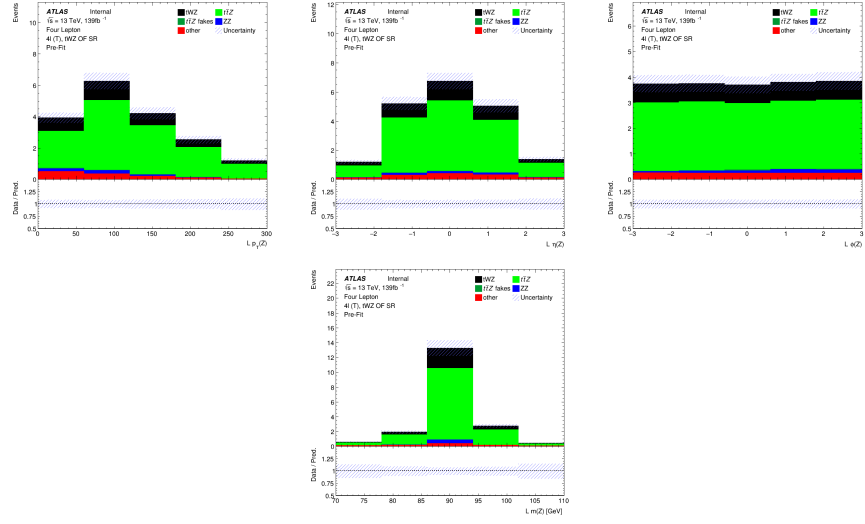


Figure A.7: MC predictions for  $p_T$ ,  $\eta$ ,  $\phi$  (top row) and mass ( $m_Z$ ) (bottom row) of the leading reconstructed  $Z$  candidate (OSSF lepton pair with  $|m_{\text{OSSF}} - m(Z)| < 30 \text{ GeV}$ ) in the  $tWZ$  OF SR region (*blinded*)

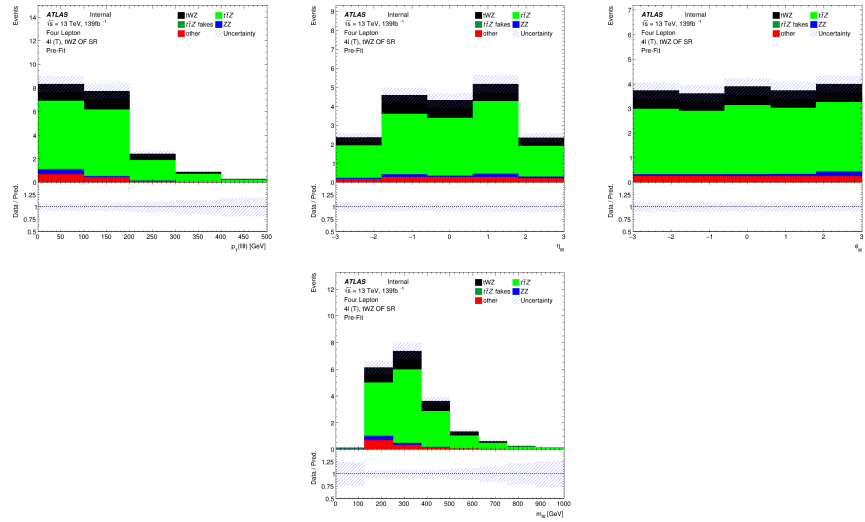


Figure A.8: MC predictions for  $p_T$ ,  $\eta$ ,  $\phi$  (top row) and mass (bottom row) of the lepton system ( $\ell\ell\ell\ell$ ) in the  $tWZ$  OF SR region (*blinded*)

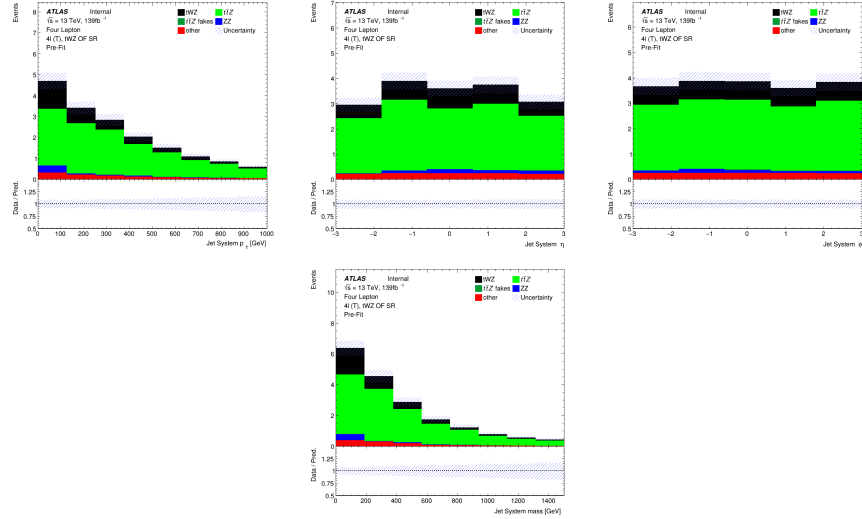


Figure A.9: MC predictions for  $p_T$ ,  $\eta$ ,  $\phi$  (top row) and mass (bottom row) of the jet systems in the  $tWZ$  OF SR region (*blinded*)

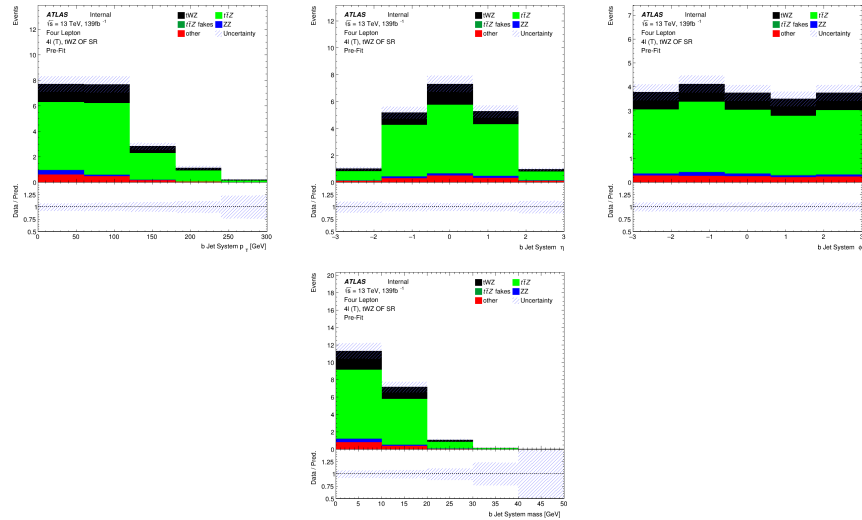


Figure A.10: MC predictions for  $p_T$ ,  $\eta$ ,  $\phi$  (top row) and mass (bottom row) of the b-tagged jet systems in the  $tWZ$  OF SR region (*blinded*)

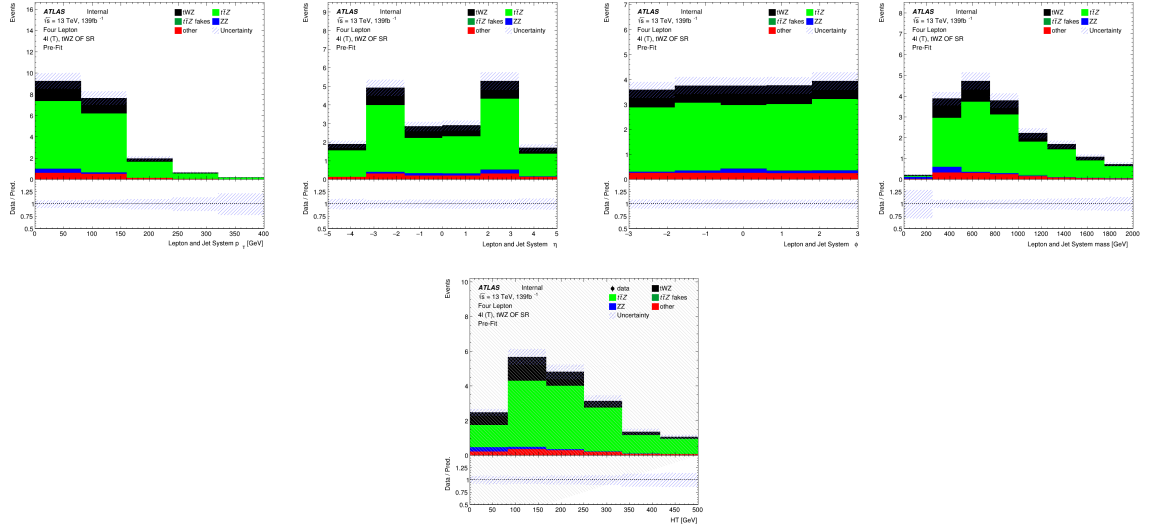


Figure A.11: MC predictions for  $p_T$ ,  $\eta$  and  $\phi$  (top row) and mass (bottom left) for the lepton + jet systems ( $\ell\ell\ell\ell$ + jets) in the  $tWZ$  OF SR region (*blinded*). Bottom right: MC predictions for  $H_T$  (scalar sum of jet  $p_T$  and lepton  $p_T$ ) in the  $tWZ$  OF SR region (*blinded*)

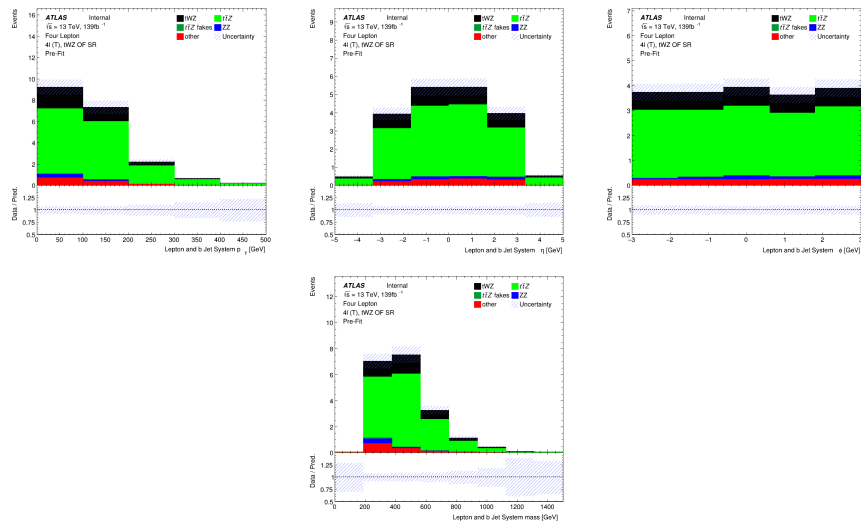


Figure A.12: MC predictions for  $p_T$ ,  $\eta$ ,  $\phi$  (top row) and mass (bottom row) of the lepton + b-tagged jet systems ( $\ell\ell\ell\ell$ + b-tagged jets) in the  $tWZ$  OF SR region (*blinded*)

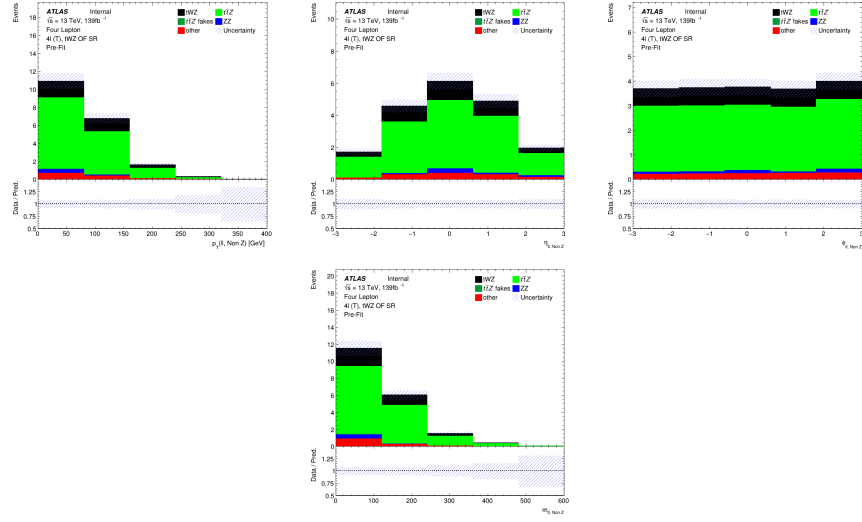


Figure A.13: MC predictions for  $p_T$ ,  $\eta$ ,  $\phi$  (top row) and mass (bottom row) of reconstructed Non  $Z$  leptons (lepton pairs which don't originate from a  $Z$  candidate) in the  $tWZ$  OF SR region (*blinded*)

### A.1.2 $tWZ$ SF SR

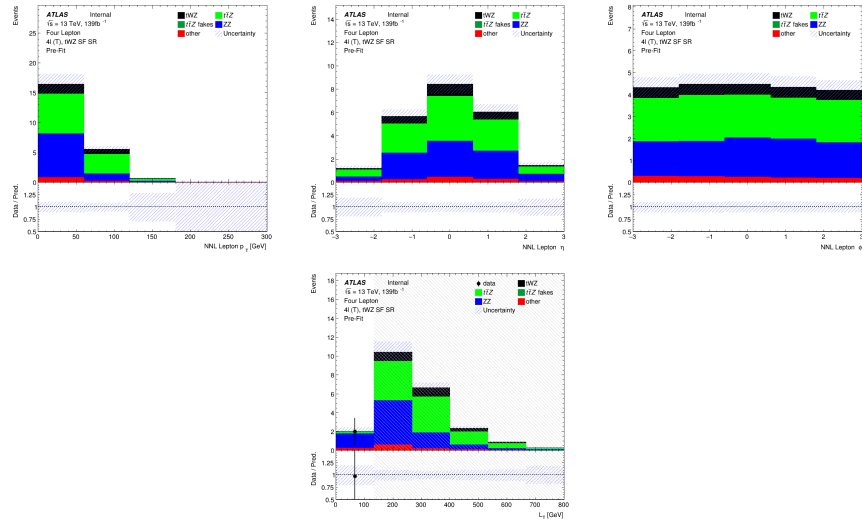


Figure A.14: Top row: MC predictions for  $p_T$ ,  $\eta$  and  $\phi$  for next-to-next-to-leading (NNL) leptons in the  $tWZ$  SF SR region (*blinded*). Bottom row: MC prediction for  $L_T$  (scalar sum of lepton  $p_T$ ) in the  $tWZ$  SF SR region (*blinded*)

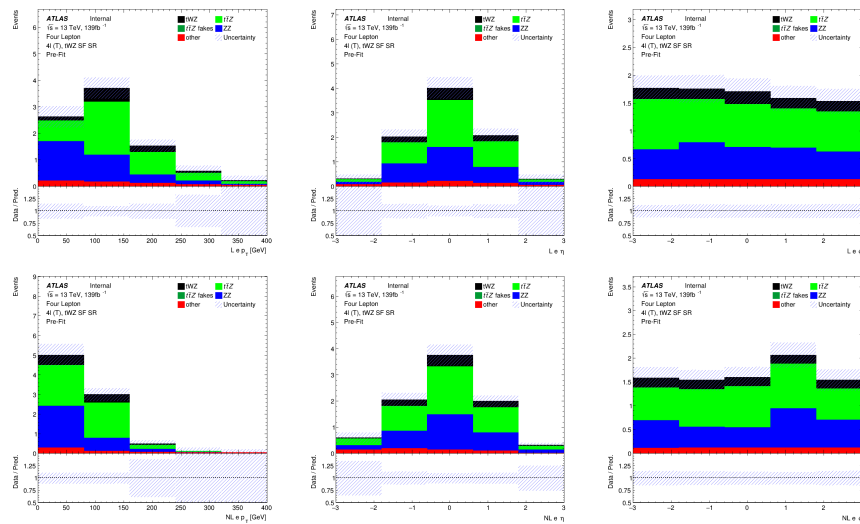


Figure A.15: MC predictions for  $p_T$ ,  $\eta$  and  $\phi$  for leading (L) electrons (top row) and next-to-leading (NL) electrons (bottom row) in the  $tWZ$  SF SR region (*blinded*)

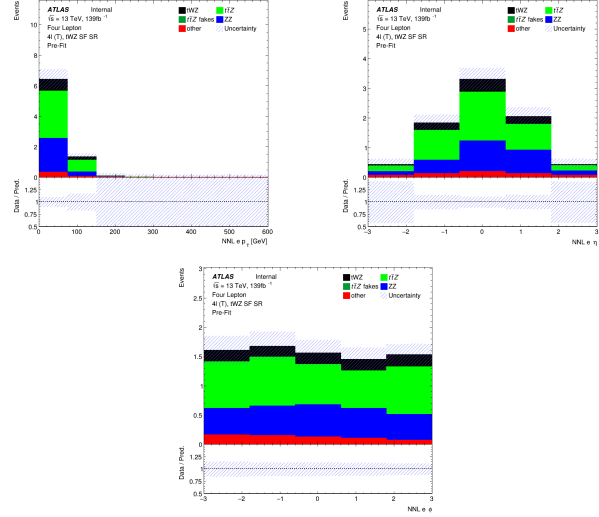


Figure A.16: MC predictions for  $p_T$ ,  $\eta$  (top row) and  $\phi$  (bottom row) for next-to-next-to-leading (NNL) electrons in the  $tWZ$  SF SR region

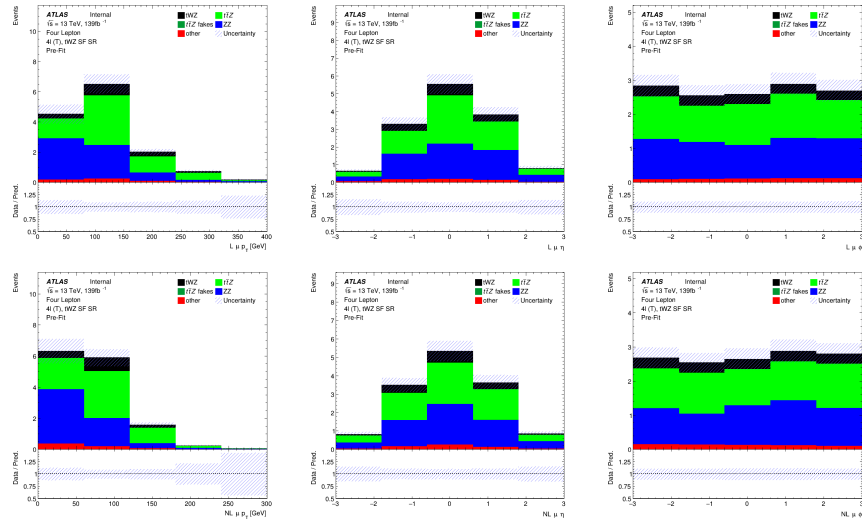


Figure A.17: MC predictions for  $p_T$ ,  $\eta$  and  $\phi$  for leading (L) muons (top row) and next-to-leading (NL) muons (bottom row) in the  $tWZ$  SF SR region (*blinded*)

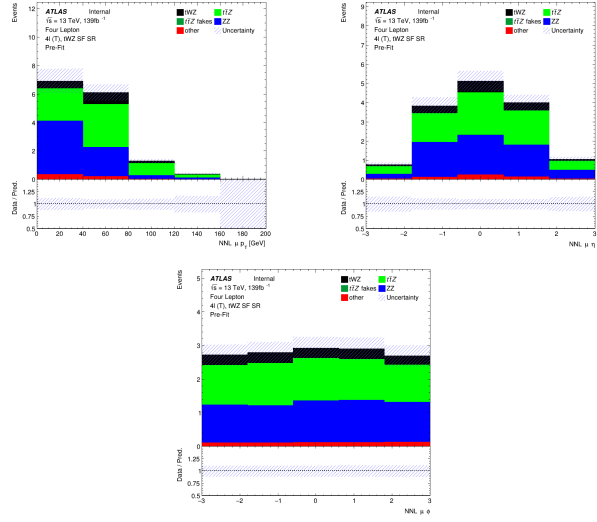


Figure A.18: MC predictions for  $p_T$ ,  $\eta$  (top row) and  $\phi$  (bottom row) for next-to-next-to-leading (NNL) muons in the  $tWZ$  SF SR region (*blinded*)

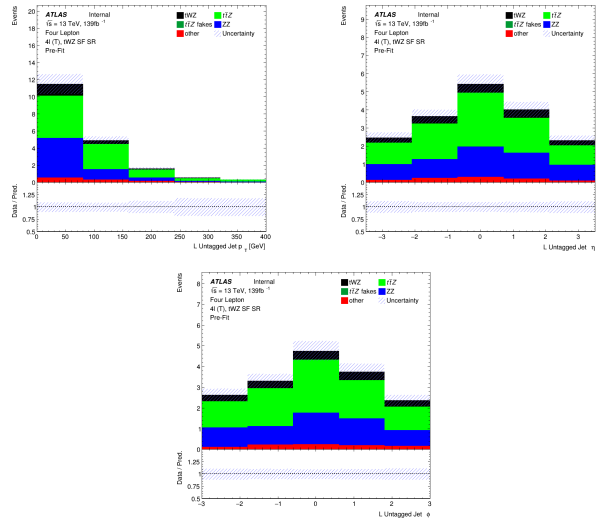


Figure A.19: MC predictions for  $p_T$ ,  $\eta$  (top row) and  $\phi$  (bottom row) for untagged jets in the  $tWZ$  SF SR region (*blinded*)

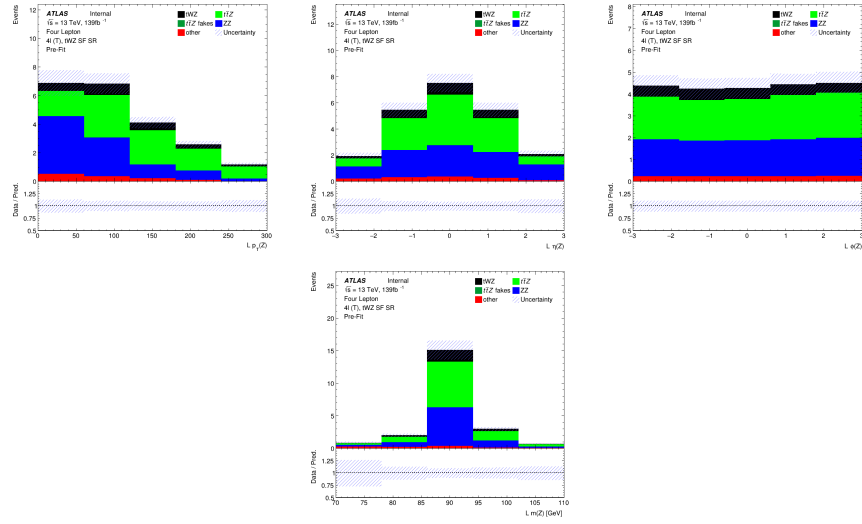


Figure A.20: MC predictions for  $p_T$ ,  $\eta$ ,  $\phi$  (top row) and mass ( $m_Z$ ) (bottom row) of the leading reconstructed  $Z$  candidate (OSSF lepton pair with  $|m_{\text{OSSF}} - m(Z)| < 30$  GeV) in the  $tWZ$  SF SR region (*blinded*)

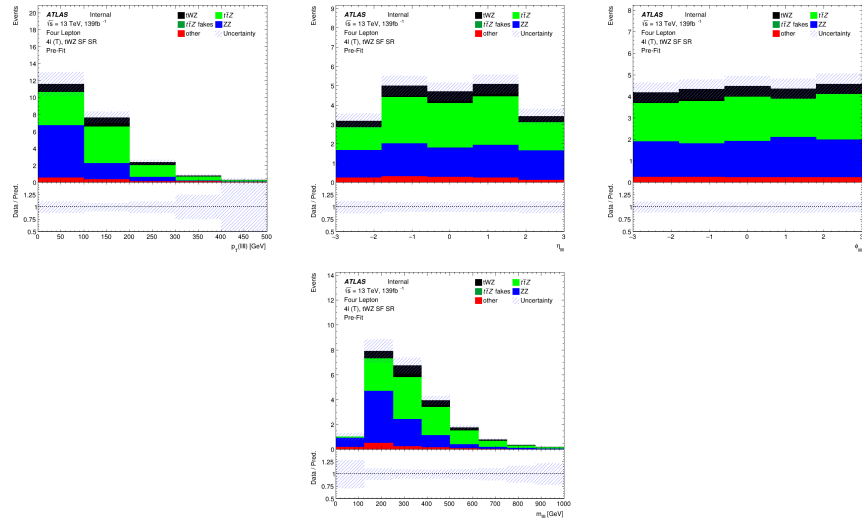


Figure A.21: MC predictions for  $p_T$ ,  $\eta$ ,  $\phi$  (top row) and mass (bottom row) of the lepton system ( $\ell\ell\ell\ell$ ) in the  $tWZ$  SF SR region (*blinded*)

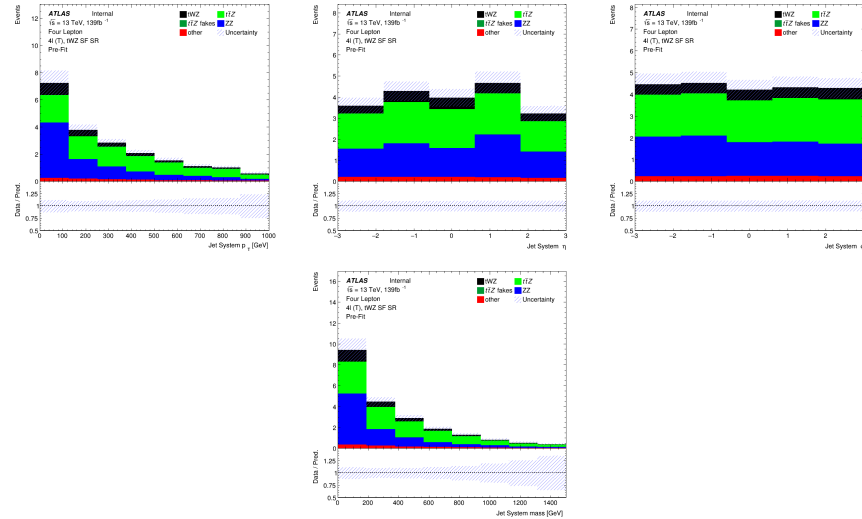


Figure A.22: MC predictions for  $p_T$ ,  $\eta$ ,  $\phi$  (top row) and mass (bottom row) of the jet systems in the  $tWZ$  SF SR region (*blinded*)

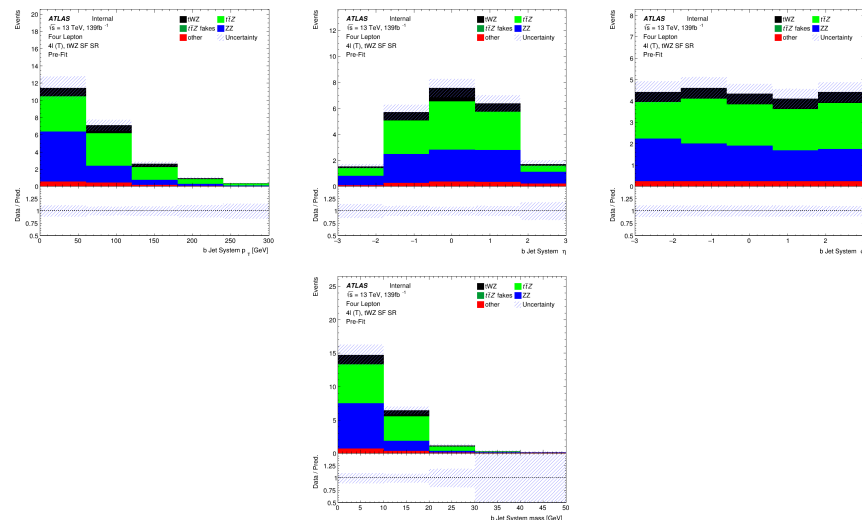


Figure A.23: MC predictions for  $p_T$ ,  $\eta$ ,  $\phi$  (top row) and mass (bottom row) of the b-tagged jet systems in the  $tWZ$  SF SR region (*blinded*)

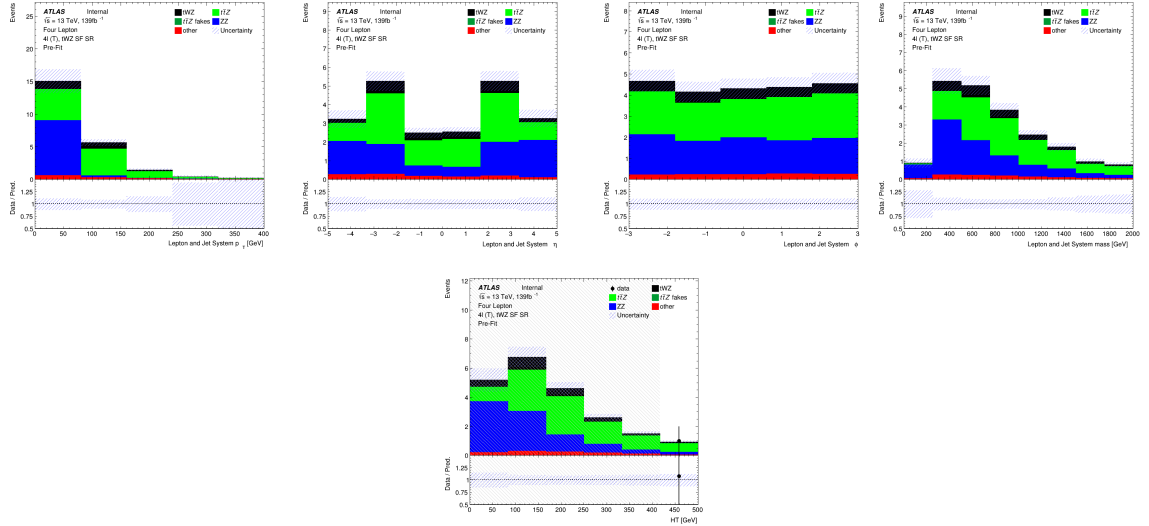


Figure A.24: MC predictions for  $p_T$ ,  $\eta$  and  $\phi$  (top row) and mass (bottom left) for the lepton + jet systems ( $\ell\ell\ell\ell + \text{jets}$ ) in the  $tWZ$  SF SR region (*blinded*). Bottom right: MC predictions for  $H_T$  (scalar sum of jet  $p_T$  and lepton  $p_T$ ) in the  $tWZ$  SF SR region (*blinded*)

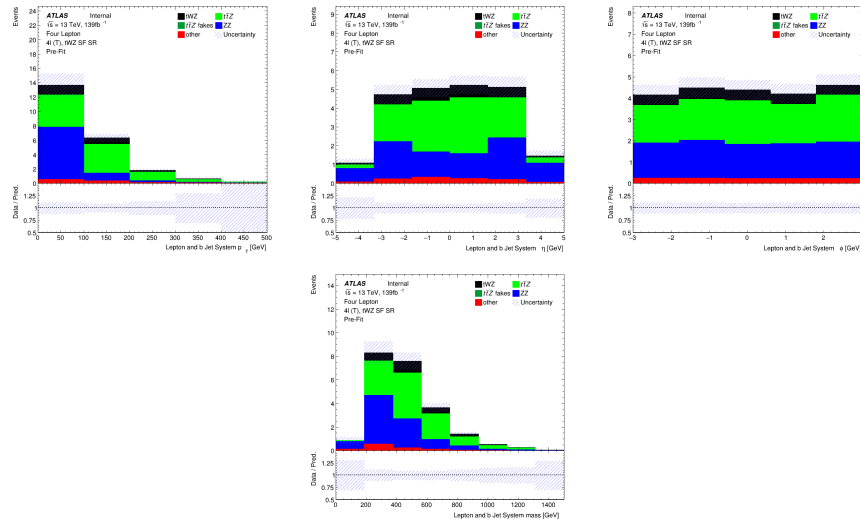


Figure A.25: MC predictions for  $p_T$ ,  $\eta$ ,  $\phi$  (top row) and mass (bottom row) of the lepton + b-tagged jet systems ( $\ell\ell\ell\ell + \text{b-tagged jets}$ ) in the  $tWZ$  SF SR region (*blinded*)

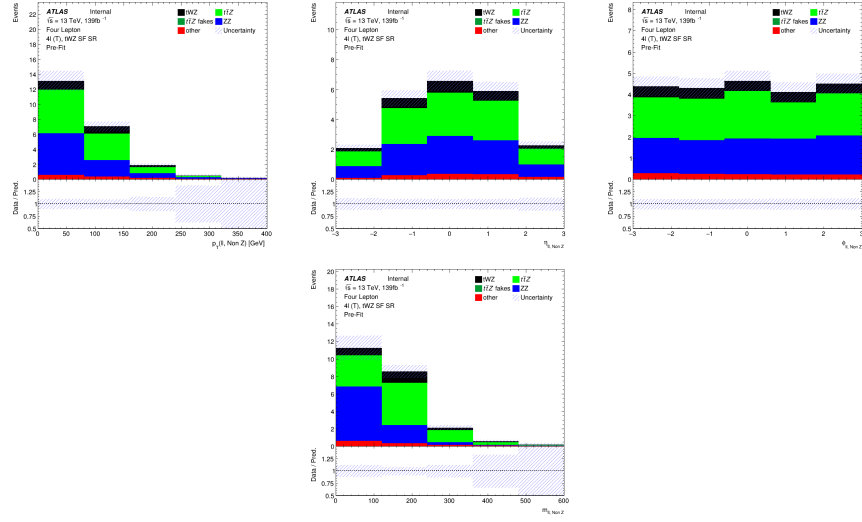


Figure A.26: MC predictions for  $p_T$ ,  $\eta$ ,  $\phi$  (top row) and mass (bottom row) of reconstructed Non  $Z$  leptons (lepton pairs which don't originate from a  $Z$  candidate) in the  $tWZ$  SF SR region (*blinded*)

### A.1.3 $t\bar{t}Z$ CR

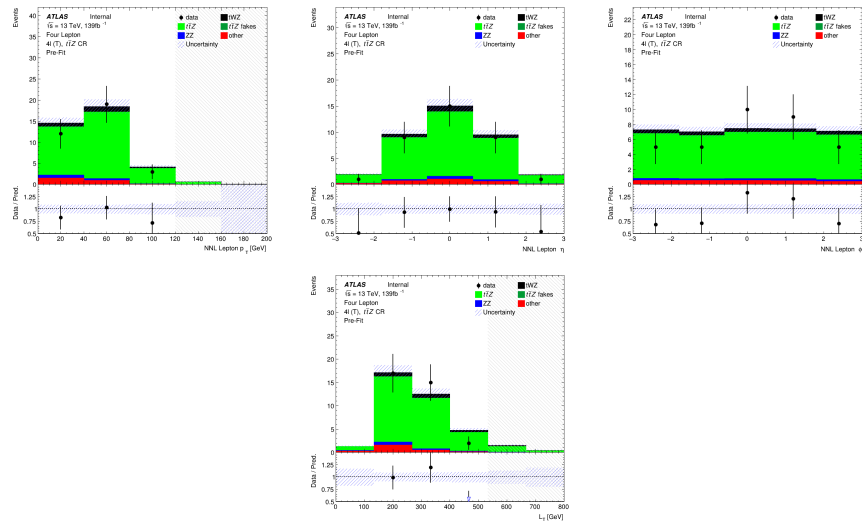


Figure A.27: Top row: MC predictions for  $p_T$ ,  $\eta$  and  $\phi$  for next-to-next-to-leading (NNL) leptons in the  $t\bar{t}Z$  CR region . Bottom row: MC predictions for  $L_T$  (scalar sum of lepton  $p_T$ ) in the  $t\bar{t}Z$  CR region

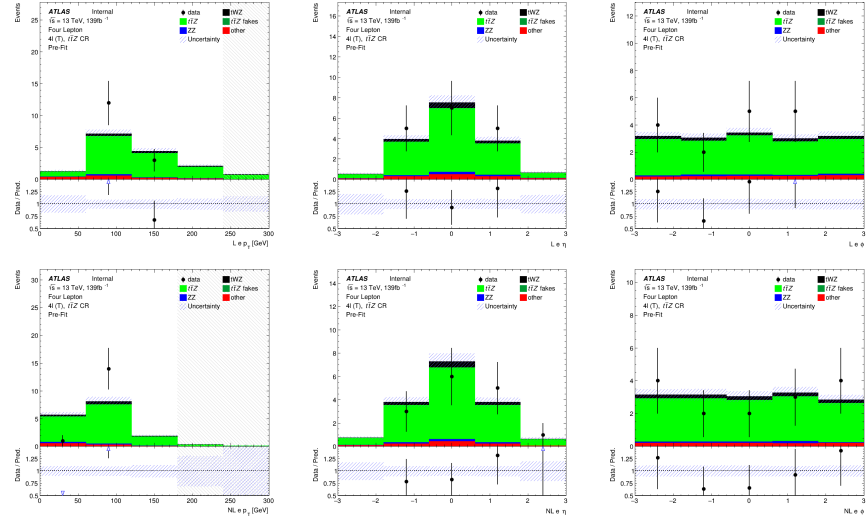


Figure A.28: MC predictions for  $p_T$ ,  $\eta$  and  $\phi$  for leading (L) electrons (top row) and next-to-leading (NL) electrons (bottom row) in the  $t\bar{t}Z$  CR region

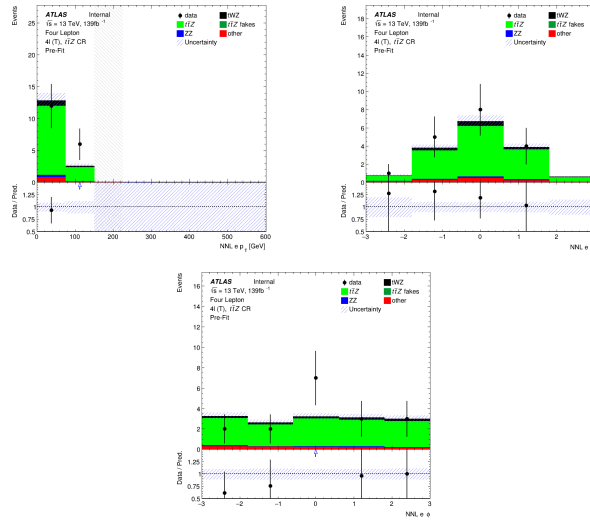


Figure A.29: MC predictions for  $p_T$ ,  $\eta$  (top row) and  $\phi$  (bottom row) for next-to-next-to-leading (NNL) electrons in the  $t\bar{t}Z$  CR region

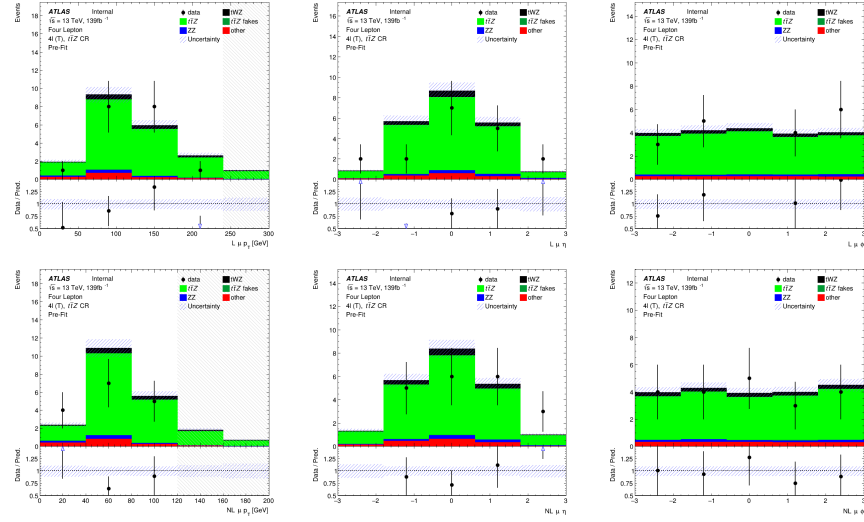


Figure A.30: MC predictions for  $p_T$ ,  $\eta$  and  $\phi$  for leading (L) muons (top row) and next-to-leading (NL) muons (bottom row) in the  $t\bar{t}Z$  CR region

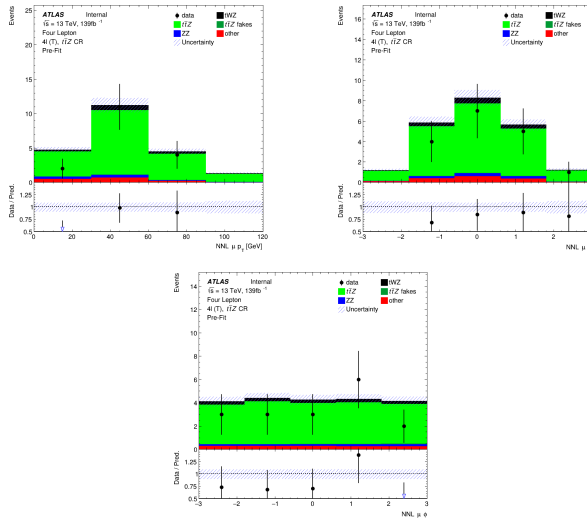


Figure A.31: MC predictions for  $p_T$ ,  $\eta$  (top row) and  $\phi$  (bottom row) for next-to-next-to-leading (NNL) muons in the  $t\bar{t}Z$  CR region

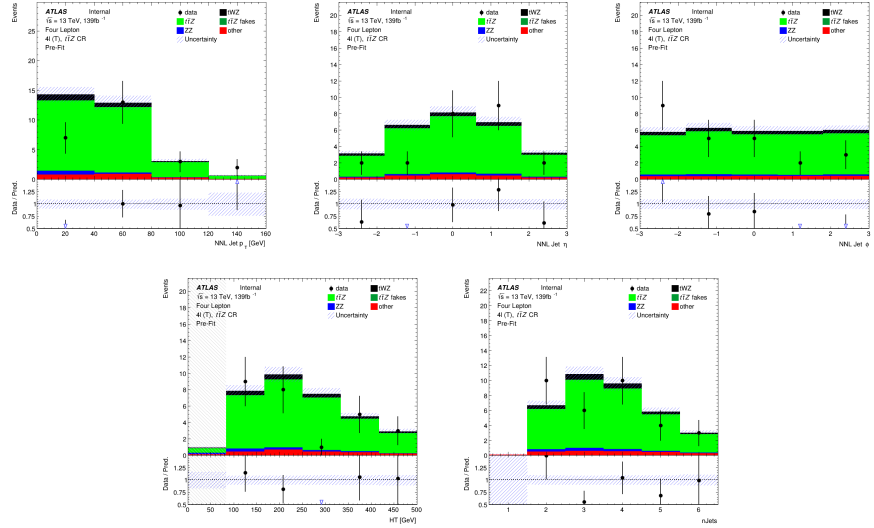


Figure A.32: Top row: MC predictions for  $p_T$ ,  $\eta$  and  $\phi$  for next-to-next-to-leading (NNL) jets in the  $t\bar{t}Z$  CR region. . Bottom row: MC predictions for  $H_T$  (scalar sum of Jet  $p_T$ ) (left) and the Number of jets (right) in the  $t\bar{t}Z$  CR region

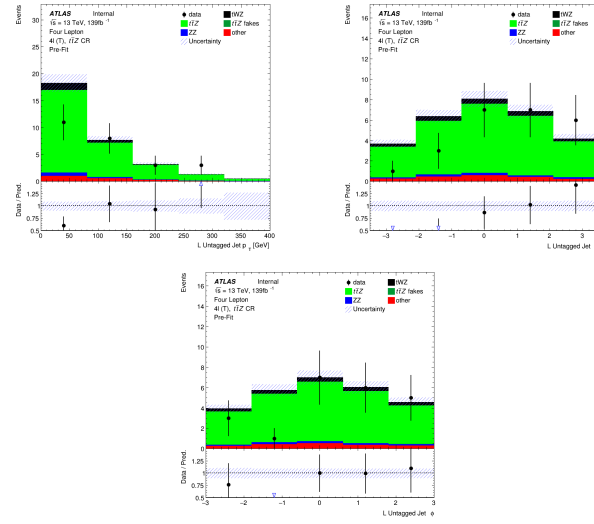


Figure A.33: MC predictions for  $p_T$ ,  $\eta$  (top row) and  $\phi$  (bottom row) for untagged jets in the  $t\bar{t}Z$  CR region

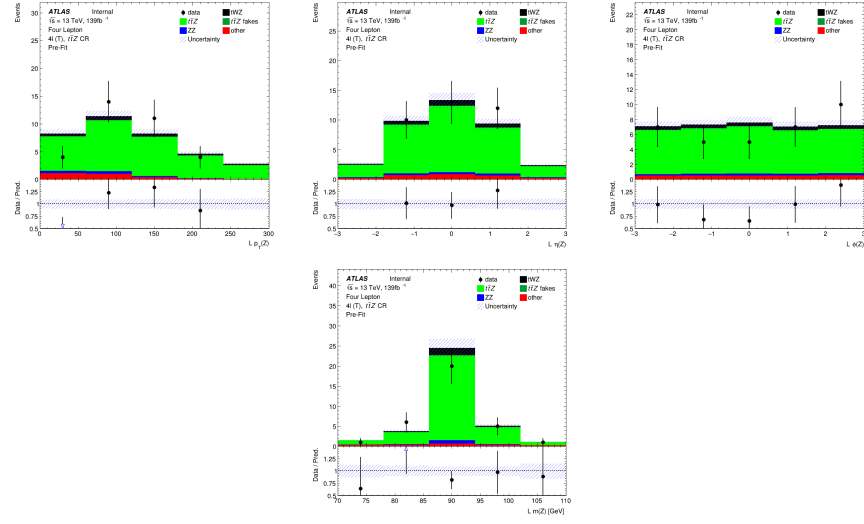


Figure A.34: MC predictions for  $p_T$ ,  $\eta$ ,  $\phi$  (top row) and mass ( $m_Z$ ) (bottom row) of reconstructed leading  $Z$  candidates (OSSF lepton pair with  $|m_{\text{OSSF}} - m(Z)| < 30 \text{ GeV}$ ) in the  $t\bar{t}Z$  CR region

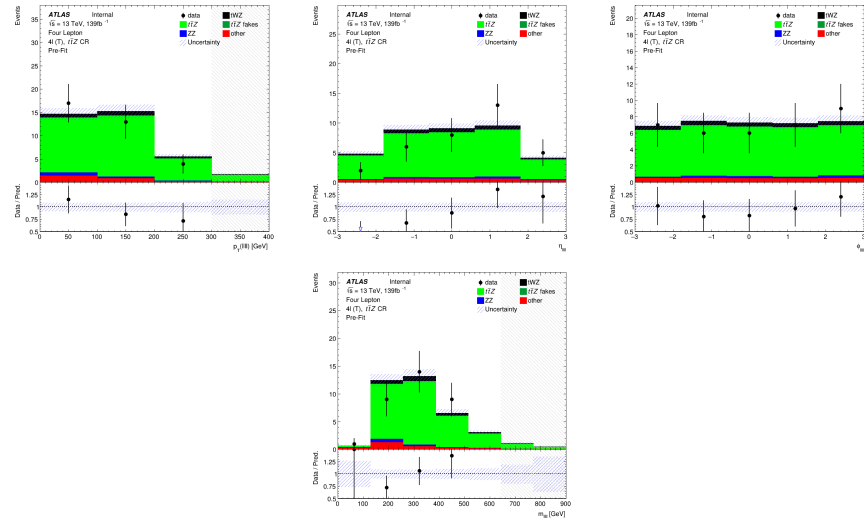


Figure A.35: MC predictions for  $p_T$ ,  $\eta$ ,  $\phi$  (top row) and mass (bottom row) of the lepton system ( $\ell\ell\ell\ell$ ) in the  $t\bar{t}Z$  CR region

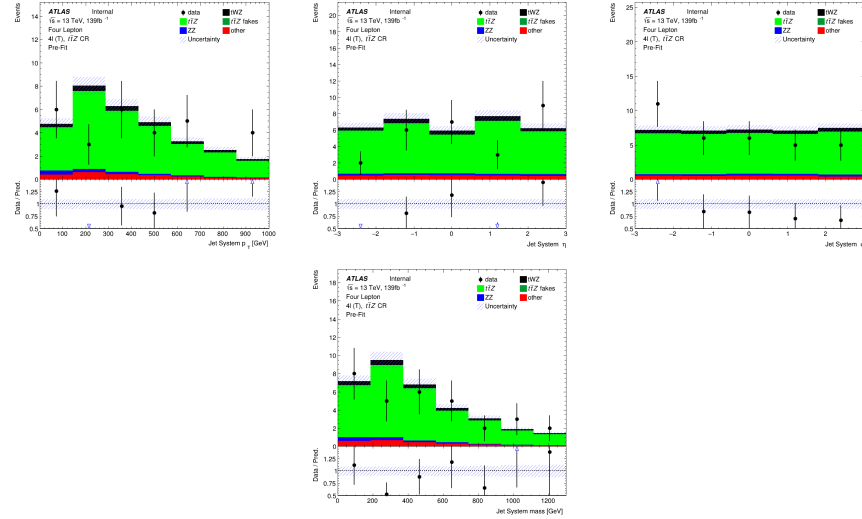


Figure A.36: MC predictions for  $p_T$ ,  $\eta$ ,  $\phi$  (top row) and mass (bottom row) of the jet systems in the  $t\bar{t}Z$  CR region

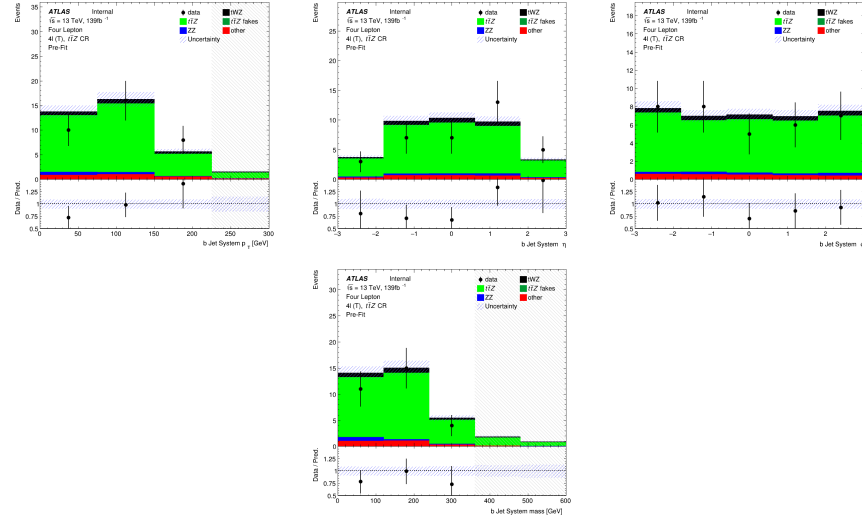


Figure A.37: MC predictions for  $p_T$ ,  $\eta$ ,  $\phi$  (top row) and mass (bottom row) of the b-tagged jet systems in the  $t\bar{t}Z$  CR region

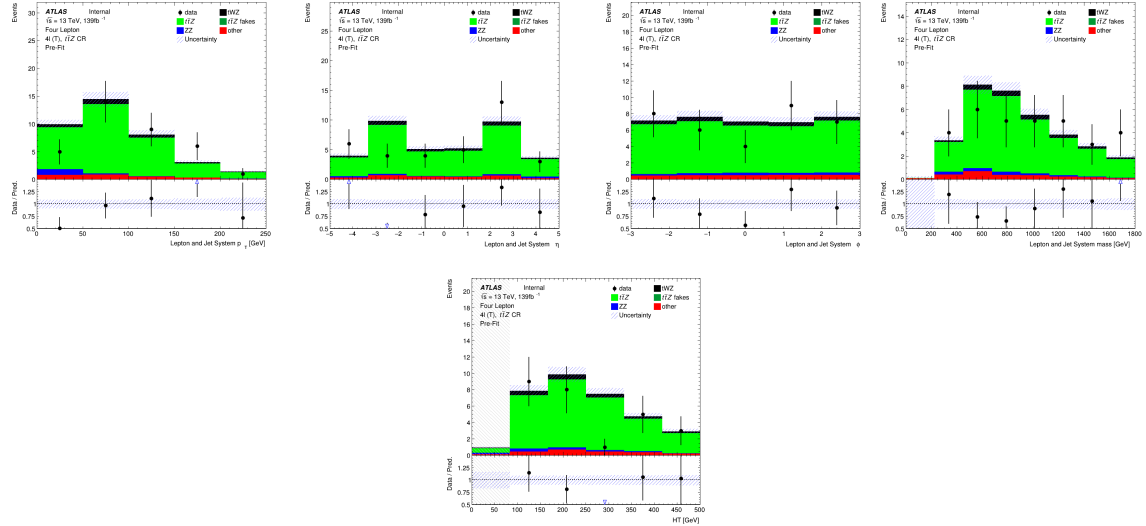


Figure A.38: MC predictions for  $p_T$ ,  $\eta$  and  $\phi$  (top row) and mass (bottom left) for the lepton + jet systems ( $\ell\ell\ell\ell$ + jets) in the  $t\bar{t}Z$  CR region . Bottom right: MC predictions for  $H_T$  (scalar sum of jet  $p_T$  and lepton  $p_T$ ) in the  $t\bar{t}Z$  CR region

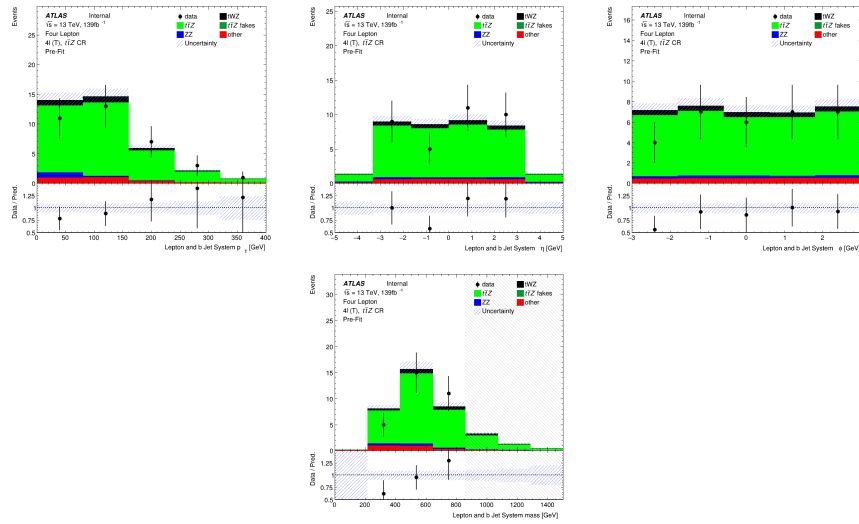


Figure A.39: MC predictions for  $p_T$ ,  $\eta$ ,  $\phi$  (top row) and mass (bottom row) of the lepton + b-tagged jet systems ( $\ell\ell\ell\ell$ + b-tagged jets) in the  $t\bar{t}Z$  CR region

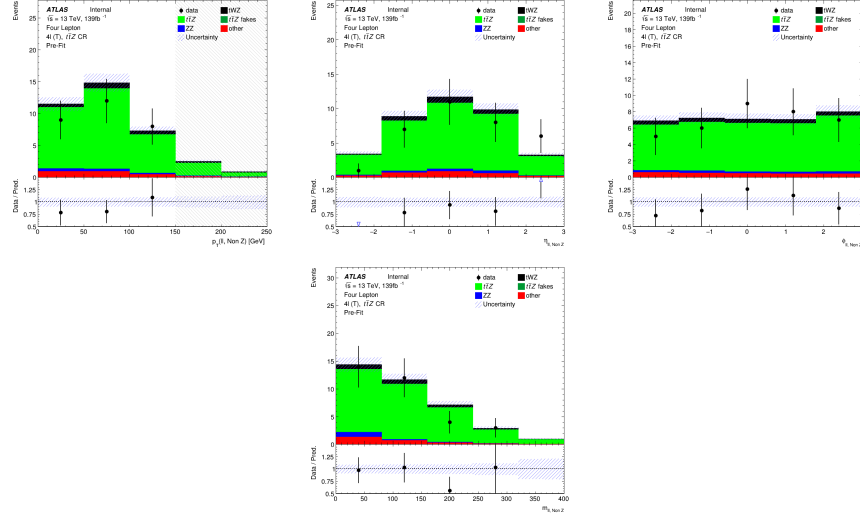


Figure A.40: MC predictions for  $p_T$ ,  $\eta$ ,  $\phi$  (top row) and mass (bottom row) of reconstructed Non  $Z$  leptons (lepton pairs which don't originate from a  $Z$  candidate) in the  $t\bar{t}Z$  CR region

#### A.1.4 $ZZb$ CR

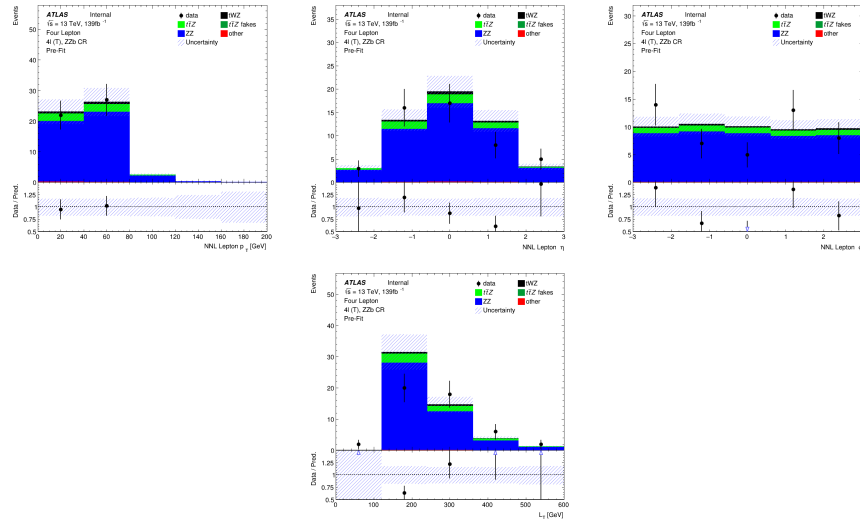


Figure A.41: Top row: MC predictions for  $p_T$ ,  $\eta$  and  $\phi$  for next-to-next-to-leading (NNL) leptons in the  $ZZb$  CR region . Bottom row: MC predictions for  $L_T$  (scalar sum of lepton  $p_T$ ) in the  $ZZb$  CR region

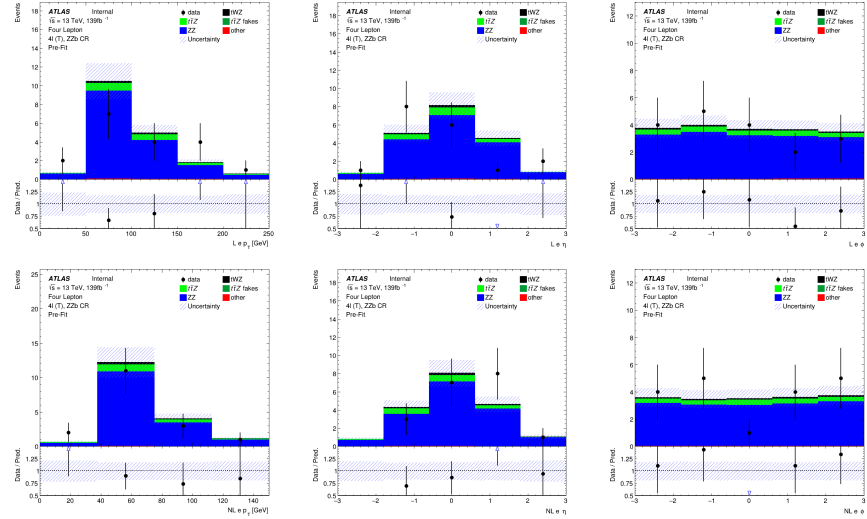


Figure A.42: MC predictions for  $p_T$ ,  $\eta$  and  $\phi$  for leading (L) electrons (top row) and next-to-leading (NL) electrons (bottom row) in the  $ZZb$  CR region

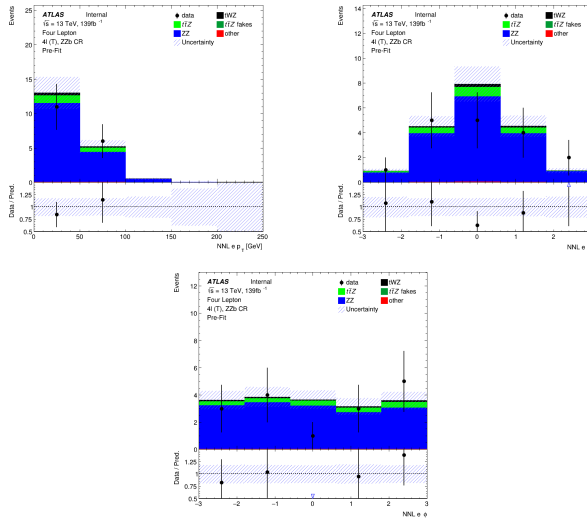


Figure A.43: MC predictions for  $p_T$ ,  $\eta$  (top row) and  $\phi$  (bottom row) for next-to-next-to-leading (NNL) electrons in the  $ZZb$  CR region

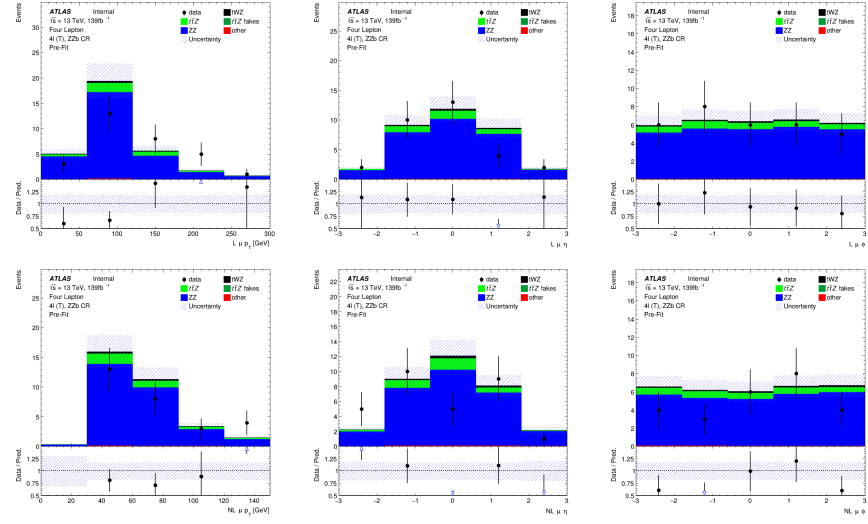


Figure A.44: MC predictions for  $p_T$ ,  $\eta$  and  $\phi$  for leading (L) muons (top row) and next-to-leading (NL) muons (bottom row) in the  $ZZb$  CR region

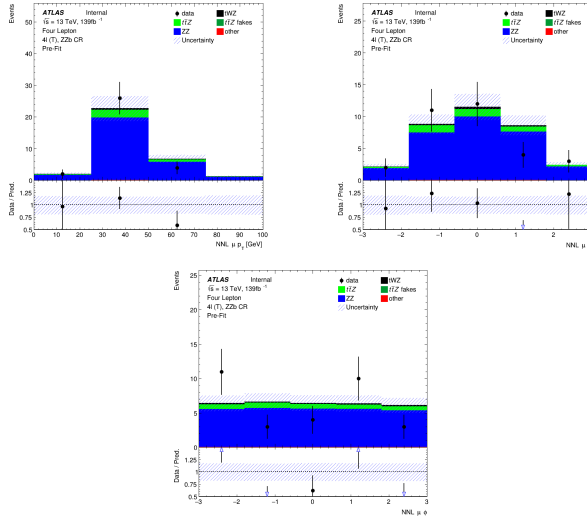


Figure A.45: MC predictions for  $p_T$ ,  $\eta$  (top row) and  $\phi$  (bottom row) for next-to-next-to-leading (NNL) muons in the  $ZZb$  CR region

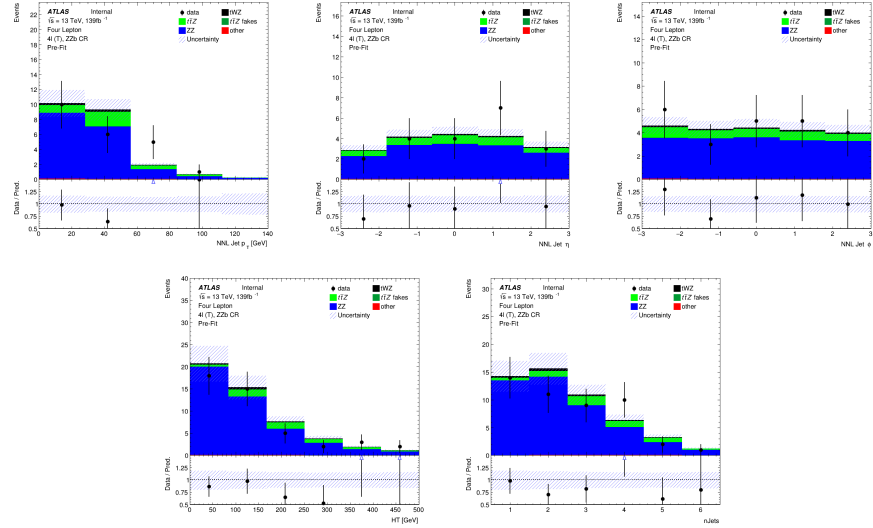


Figure A.46: Top row: MC predictions for  $p_T$ ,  $\eta$  and  $\phi$  for next-to-next-to-leading (NNL) jets in the  $ZZb$  CR region . . Bottom row: MC predictions for  $H_T$  (scalar sum of Jet  $p_T$ ) (left) and the Number of jets (right) in the  $ZZb$  CR region

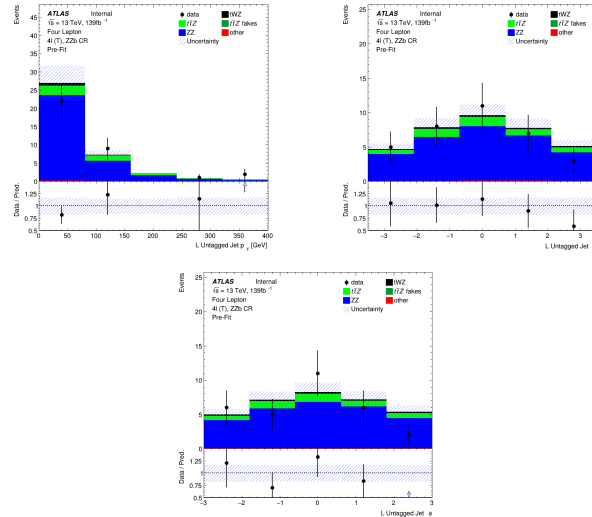


Figure A.47: MC predictions for  $p_T$ ,  $\eta$  (top row) and  $\phi$  (bottom row) for untagged jets in the  $ZZb$  CR region

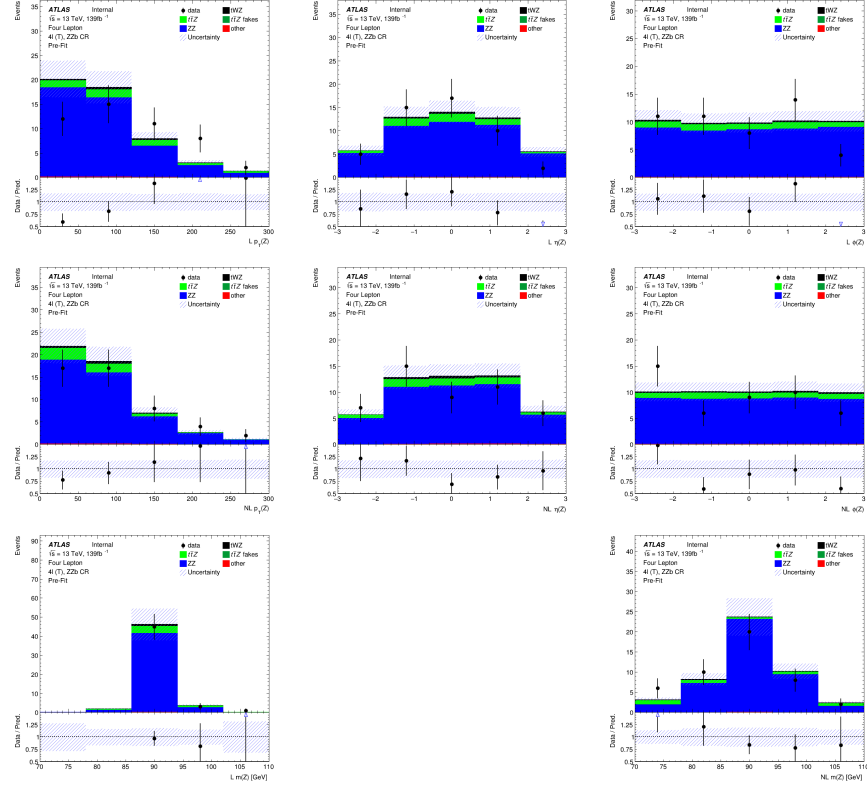


Figure A.48: MC predictions for  $p_T$ ,  $\eta$ ,  $\phi$  of the leading (top row), next-to-leading (middle row) and mass ( $m_Z$ ) (bottom row) of reconstructed  $Z$  candidates (OSSF lepton pair with  $|m_{\text{OSSF}} - m(Z)| < 30 \text{ GeV}$ ) in the  $ZZb$  CR region

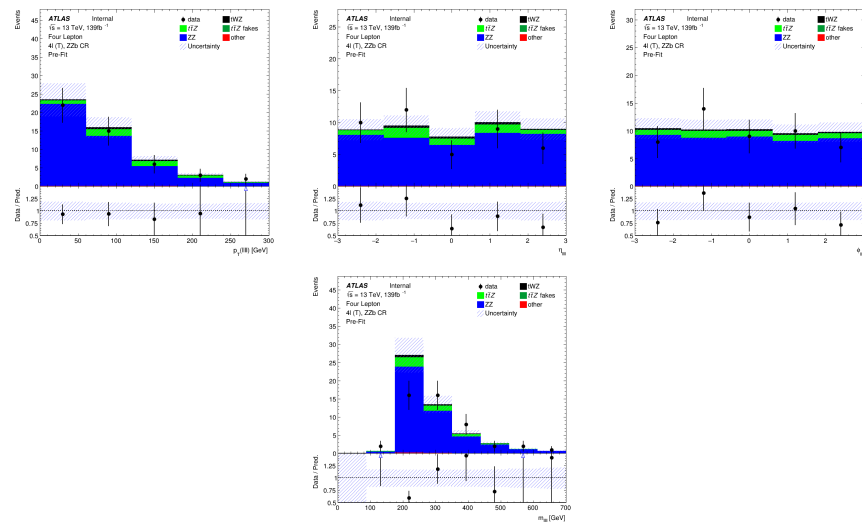


Figure A.49: MC predictions for  $p_T$ ,  $\eta$ ,  $\phi$  (top row) and mass (bottom row) of the lepton system ( $\ell\ell\ell\ell$ ) in the  $ZZ$  CR region

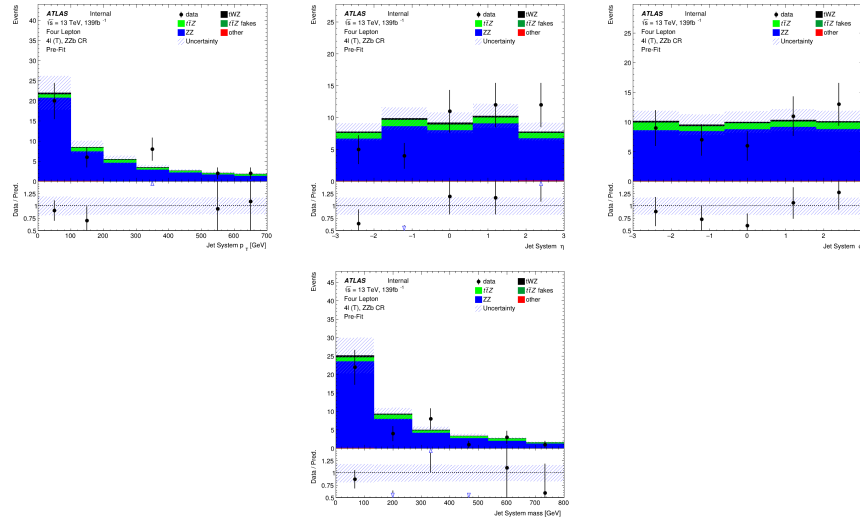


Figure A.50: MC predictions for  $p_T$ ,  $\eta$ ,  $\phi$  (top row) and mass (bottom row) of the jet systems in the  $ZZb$  CR region

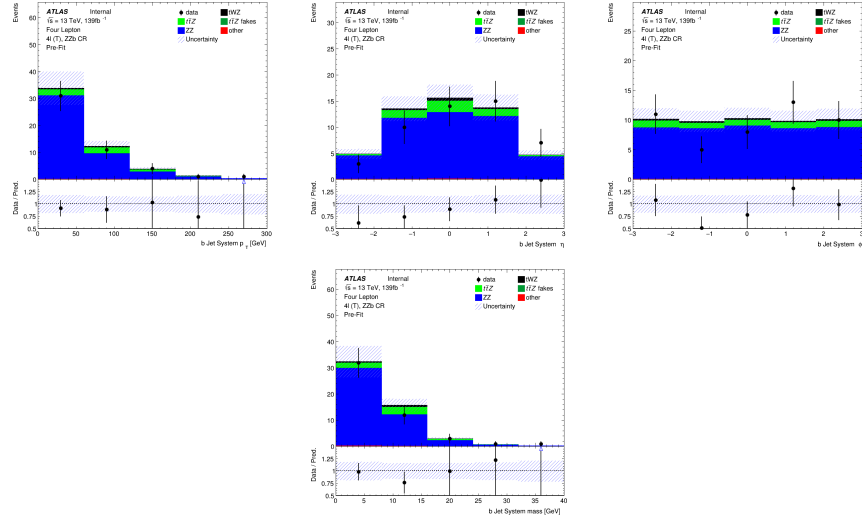


Figure A.51: MC predictions for  $p_T$ ,  $\eta$ ,  $\phi$  (top row) and mass (bottom row) of the b-tagged jet systems in the  $ZZb$  CR region

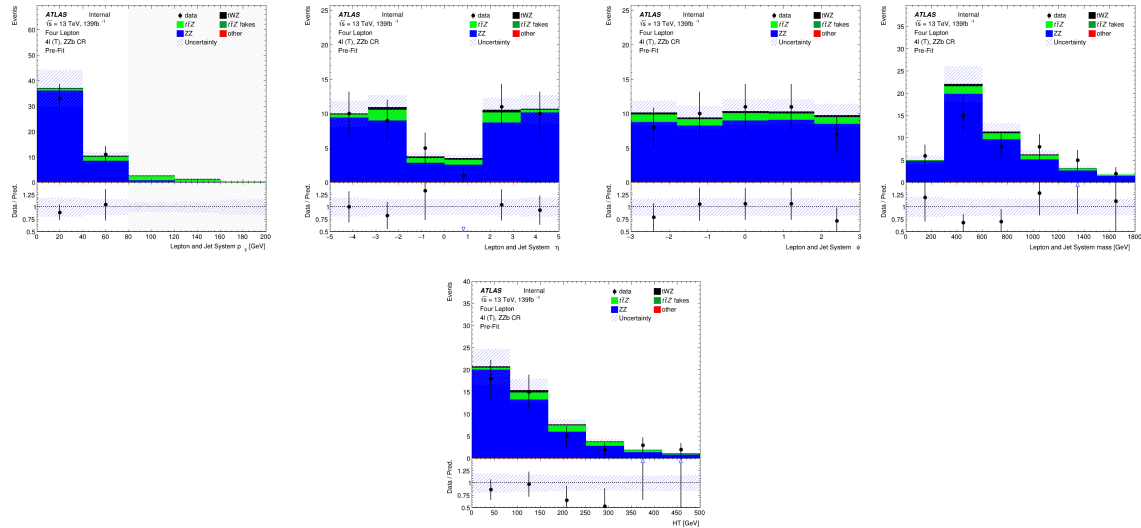


Figure A.52: MC predictions for  $p_T$ ,  $\eta$  and  $\phi$  (top row) and mass (bottom left) for the lepton + jet systems ( $\ell\ell\ell\ell +$  jets) in the  $ZZb$  CR region . Bottom right: MC predictions for  $H_T$  (scalar sum of jet  $p_T$  and lepton  $p_T$ ) in the  $ZZb$  CR region

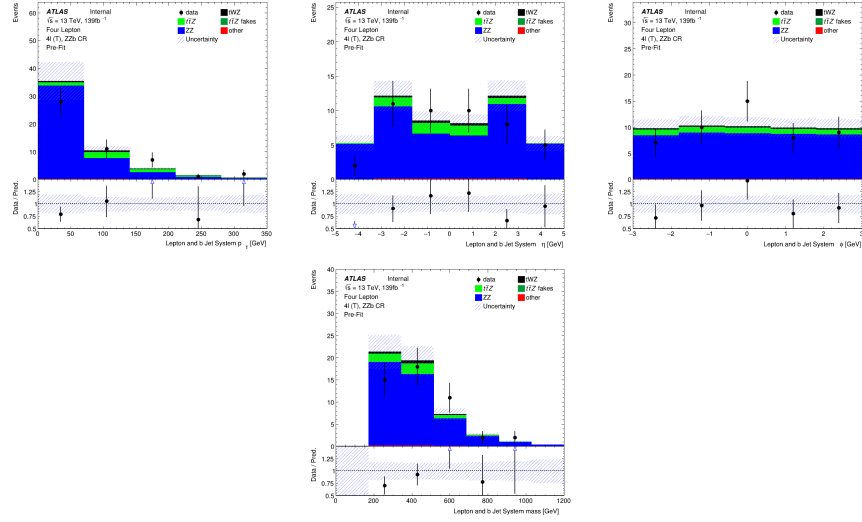


Figure A.53: MC predictions for  $p_T$ ,  $\eta$ ,  $\phi$  (top row) and mass (bottom row) of the lepton + b-tagged jet systems ( $\ell\ell\ell\ell +$  b-tagged jets) in the  $ZZb$  CR region

### A.1.5 $(tWZ)$ fake CR

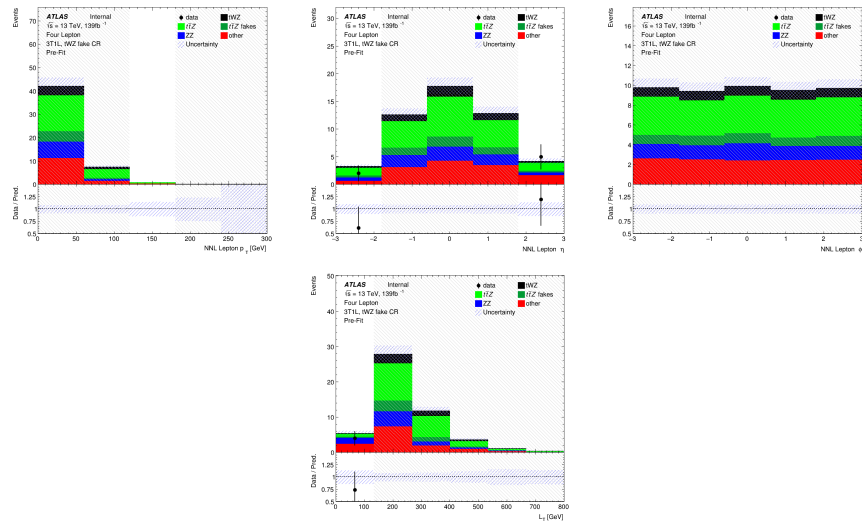


Figure A.54: Top row: MC predictions for  $p_T$ ,  $\eta$  and  $\phi$  for next-to-next-to-leading (NNL) leptons in the  $(tWZ)$ fake CR region . Bottom row: MC predictions for  $L_T$  (scalar sum of lepton  $p_T$ ) in the  $(tWZ)$ fake CR region

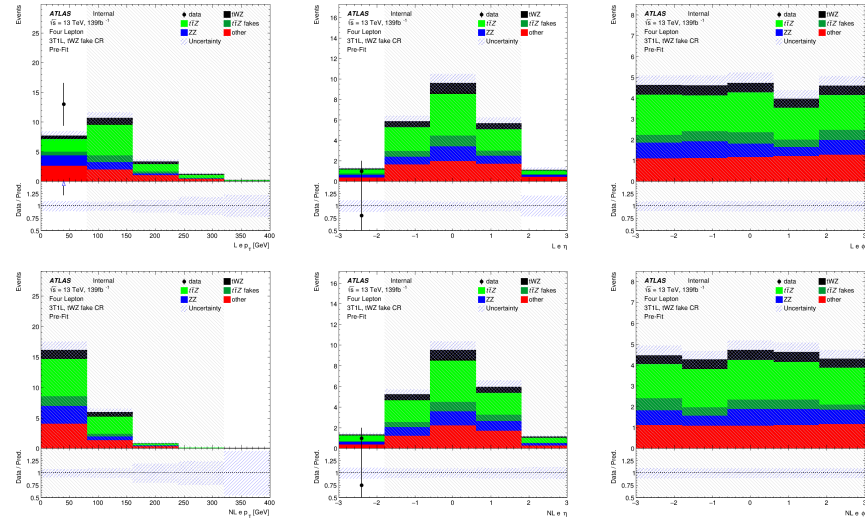


Figure A.55: MC predictions for  $p_T$ ,  $\eta$  and  $\phi$  for leading (L) electrons (top row) and next-to-leading (NL) electrons (bottom row) in the  $(tWZ)_{\text{fake}}$  CR region

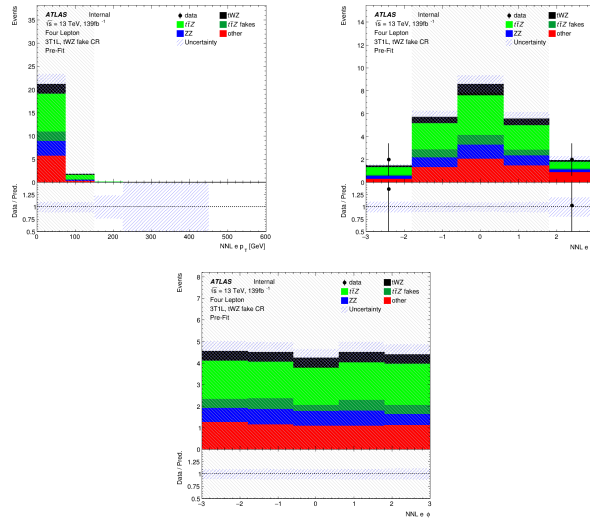


Figure A.56: MC predictions for  $p_T$ ,  $\eta$  (top row) and  $\phi$  (bottom row) for next-to-next-to-leading (NNL) electrons in the  $(tWZ)_{\text{fake}}$  CR region

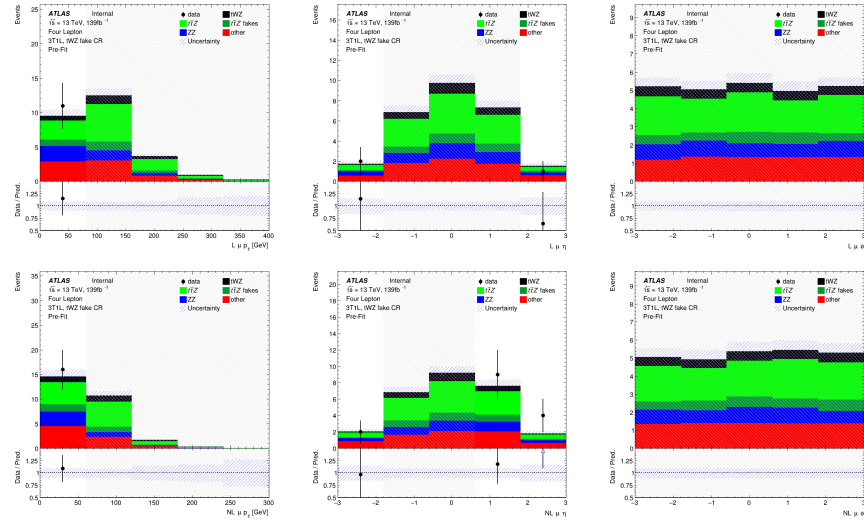


Figure A.57: MC predictions for  $p_T$ ,  $\eta$  and  $\phi$  for leading (L) muons (top row) and next-to-leading (NL) muons (bottom row) in the  $(tWZ)_{\text{fake}}$  CR region

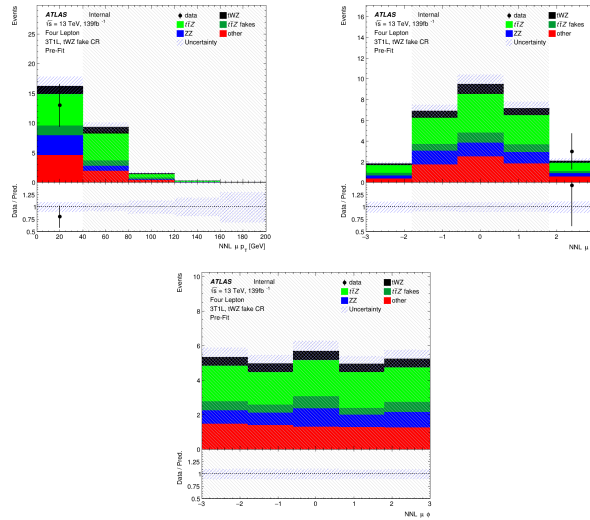


Figure A.58: MC predictions for  $p_T$ ,  $\eta$  (top row) and  $\phi$  (bottom row) for next-to-next-to-leading (NNL) muons in the  $(tWZ)_{\text{fake}}$  CR region

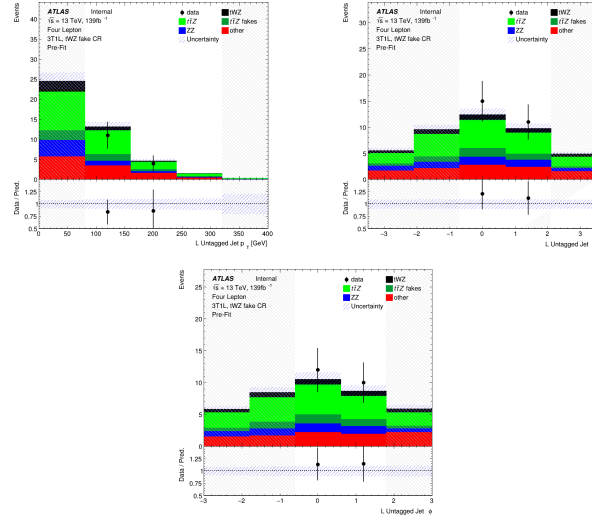


Figure A.59: MC predictions for  $p_T$ ,  $\eta$  (top row) and  $\phi$  (bottom row) for untagged jets in the  $(tWZ)_{\text{fake}}$  CR region

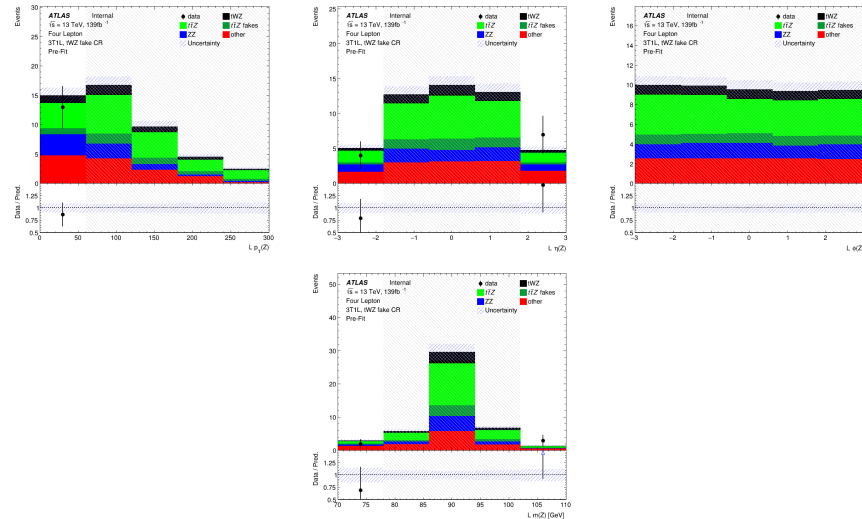


Figure A.60: MC predictions for  $p_T$ ,  $\eta$ ,  $\phi$  (top row) and mass ( $m_Z$ ) (bottom row) of the leading reconstructed  $Z$  candidate (OSSF lepton pair with  $|m_{\text{OSSF}} - m(Z)| < 30 \text{ GeV}$ ) in the  $(tWZ)_{\text{fake}}$  CR region

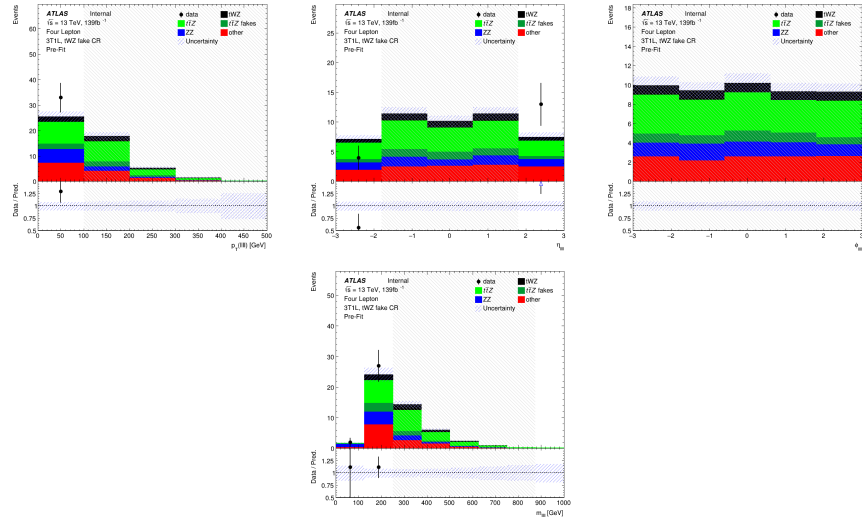


Figure A.61: MC predictions for  $p_T$ ,  $\eta$ ,  $\phi$  (top row) and mass (bottom row) of the lepton system ( $\ell\ell\ell\ell$ ) in the  $(tWZ)_{\text{fake}}$  CR region

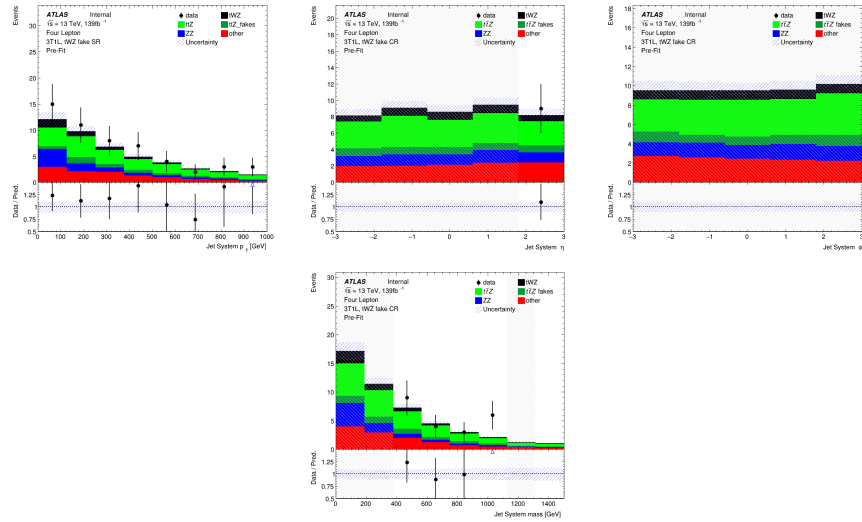


Figure A.62: MC predictions for  $p_T$ ,  $\eta$ ,  $\phi$  (top row) and mass (bottom row) of the jet systems in the  $(tWZ)_{\text{fake}}$  CR region

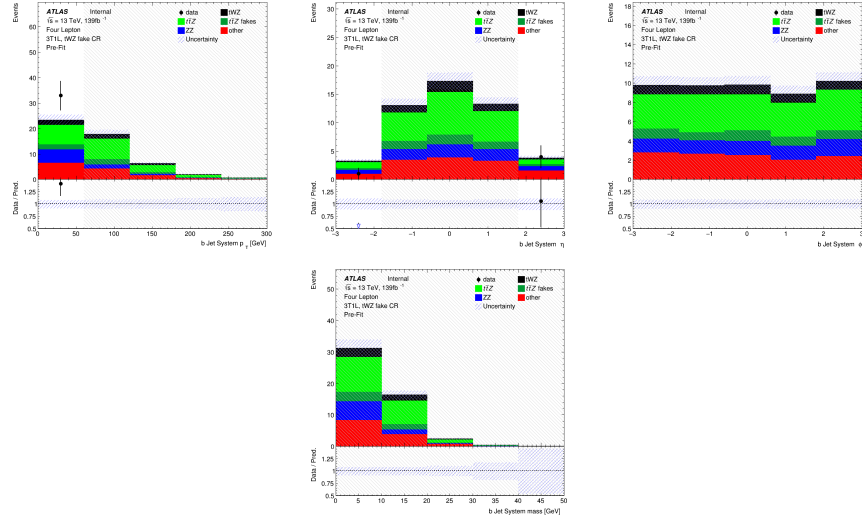


Figure A.63: MC predictions for  $p_T$ ,  $\eta$ ,  $\phi$  (top row) and mass (bottom row) of the b-tagged jet systems in the  $(tWZ)_{\text{fake}}$  CR region

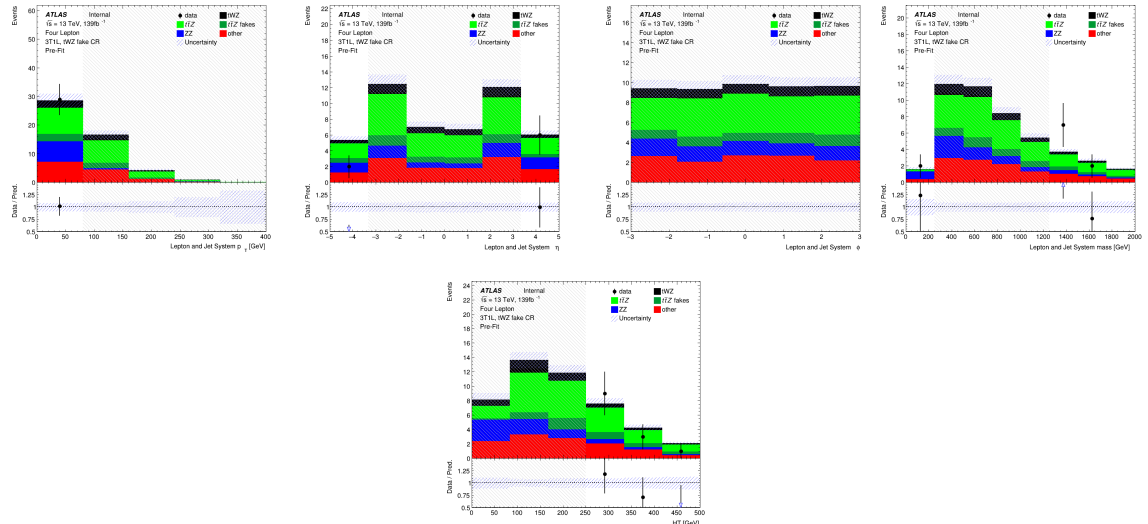


Figure A.64: MC predictions for  $p_T$ ,  $\eta$  and  $\phi$  (top row) and mass (bottom left) for the lepton + jet systems ( $\ell\ell\ell\ell + \text{jets}$ ) in the  $(tWZ)_{\text{fake}}$  CR region . Bottom right: MC predictions for  $H_T$  (scalar sum of jet  $p_T$  and lepton  $p_T$ ) in the  $(tWZ)_{\text{fake}}$  CR region

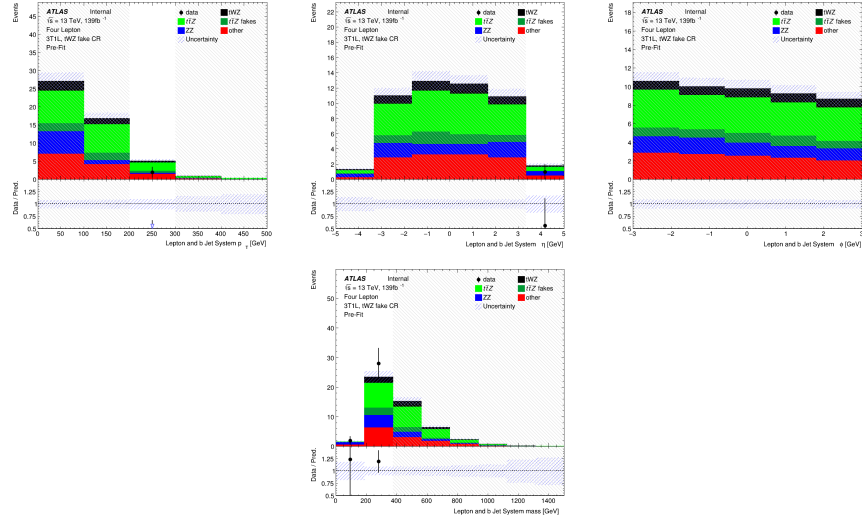


Figure A.65: MC predictions for  $p_T$ ,  $\eta$ ,  $\phi$  (top row) and mass (bottom row) of the lepton + b-tagged jet systems ( $\ell\ell\ell\ell +$  b-tagged jets) in the  $(tWZ)_{\text{fake}}$  CR region

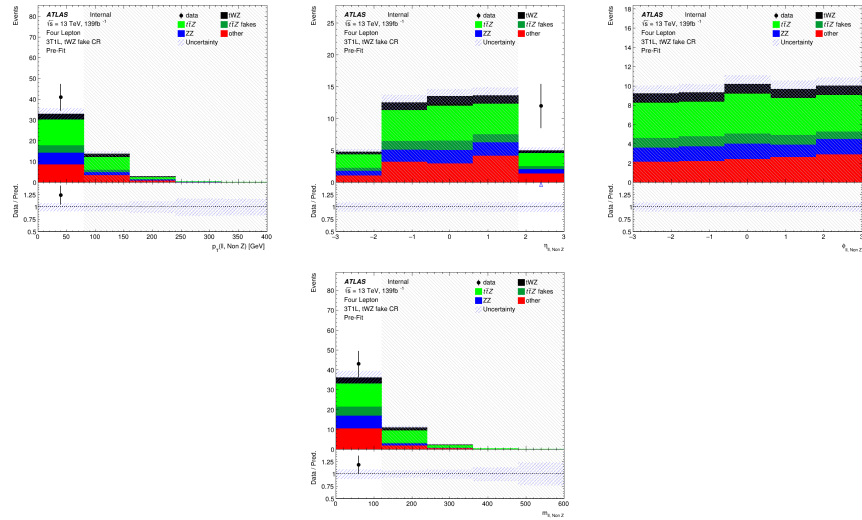


Figure A.66: MC predictions for  $p_T$ ,  $\eta$ ,  $\phi$  (top row) and mass (bottom row) of reconstructed Non  $Z$  leptons (lepton pairs which don't originate from a  $Z$  candidate) in the  $(tWZ)_{\text{fake}}$  CR region

# Bibliography

- [1] M. Aaboud et al. “Electron reconstruction and identification in the ATLAS experiment using the 2015 and 2016 LHC proton–proton collision data at  $\sqrt{s} = 13$  TeV”. In: *The European Physical Journal C* 79.8 (Aug. 2019). ISSN: 1434-6052. DOI: 10.1140/epjc/s10052-019-7140-6. URL: <http://dx.doi.org/10.1140/epjc/s10052-019-7140-6>.
- [2] M. Aaboud et al. “Measurement of the  $t\bar{t}Z$  and  $t\bar{t}W$  cross sections in proton-proton collisions at  $\sqrt{s} = 13$  TeV with the ATLAS detector”. In: *Phys. Rev. D* 99 (7 Apr. 2019), p. 072009. DOI: 10.1103/PhysRevD.99.072009. URL: <https://link.aps.org/doi/10.1103/PhysRevD.99.072009>.
- [3] Aaboud, M. and Aad, G. and Abbott, B. and Abbott, D. C. and Abdinov, O. and Abed Abud, A. and Abhayasinghe, D. K. and Abidi, S. H. and AbouZeid, O. S. and et al. “Measurement of ZZ production in the  $\ell\ell\nu\nu$  final state with the ATLAS detector in pp collisions at  $s \sqrt{s} = 13$  TeV”. In: *Journal of High Energy Physics* 2019.10 (Oct. 2019). ISSN: 1029-8479. DOI: {10.1007/jhep10(2019)127}. URL: %7B[http://dx.doi.org/10.1007/JHEP10\(2019\)127%7D](http://dx.doi.org/10.1007/JHEP10(2019)127%7D).
- [4] G. Aad et al. “Measurement of the  $t\bar{t}$  production cross-section in the lepton+jets channel at  $s=13$  TeV with the ATLAS experiment”. In: *Physics Letters B* 810 (2020), p. 135797. ISSN: 0370-2693. DOI: <https://doi.org/10.1016/j.physletb.2020.135797>. URL: <https://www.sciencedirect.com/science/article/pii/S0370269320306006>.
- [5] G. Aad et al. “Muon reconstruction performance of the ATLAS detector in proton–proton collision data at  $\sqrt{s} = 13$  TeV”. In: *The European Physical Journal C* 76.5 (May 2016). ISSN: 1434-6052. DOI: 10.1140/epjc/s10052-016-4120-y. URL: <http://dx.doi.org/10.1140/epjc/s10052-016-4120-y>.
- [6] Shunichi Akatsuka and Shion Chen. *Isolation WPs summary: PLV + LowPtPLV*. Oct. 2019. URL: [https://indico.cern.ch/event/854783/contributions/3595486/attachments/1929380/3195230/PLV\\_Summary.pdf](https://indico.cern.ch/event/854783/contributions/3595486/attachments/1929380/3195230/PLV_Summary.pdf).
- [7] ATLAS Collaboration. “ATLAS  $b$ -jet identification performance and efficiency measurement with  $t\bar{t}$  events in pp collisions at  $\text{sqrt}s = 13$  TeV”. In: *Eur. Phys. J. C* 79 (2019), p. 970. DOI: 10.1140/epjc/s10052-019-7450-8. arXiv: 1907.05120 [hep-ex].
- [8] ATLAS Collaboration. *Calibration of light-flavour  $b$ -jet mistagging rates using ATLAS proton–proton collision data at  $\text{sqrt}s = 13$  TeV*. ATLAS-CONF-2018-006. 2018. URL: <https://cds.cern.ch/record/2314418>.
- [9] ATLAS Collaboration. “Electron and photon performance measurements with the ATLAS detector using the 2015–2017 LHC proton–proton collision data”. In: *JINST* 14 (2019), P12006. DOI: 10.1088/1748-0221/14/12/P12006. arXiv: 1908.00005 [hep-ex].
- [10] ATLAS Collaboration. “Identification and rejection of pile-up jets at high pseudorapidity with the ATLAS detector”. In: *Eur. Phys. J. C* 77 (2017), p. 580. DOI: 10.1140/epjc/s10052-017-5081-5. arXiv: 1705.02211 [hep-ex].
- [11] ATLAS Collaboration. *Measurement of  $b$ -tagging efficiency of  $c$ -jets in  $t\bar{t}$  events using a likelihood approach with the ATLAS detector*. ATLAS-CONF-2018-001. 2018. URL: <https://cds.cern.ch/record/2306649>.
- [12] ATLAS Collaboration. “Measurements of  $b$ -jet tagging efficiency with the ATLAS detector using  $t\bar{t}$  events at  $\text{sqrt}s = 13$  TeV, TeV”. In: *JHEP* 08 (2018), p. 089. DOI: 10.1007/JHEP08(2018)089. arXiv: 1805.01845 [hep-ex].
- [13] ATLAS Collaboration. “Muon reconstruction and identification efficiency in ATLAS using the full Run 2 pp collision data set at  $\text{sqrt}s = 13$  TeV”. In: (2020). arXiv: 2012.00578 [hep-ex].
- [14] ATLAS Internal. *Electron Efficiencies for Analyses*. 2021. URL: <https://twiki.cern.ch/twiki/bin/viewauth/AtlasProtected/ElectronEfficienciesForAnalysis>.

- [15] ATLAS Internal. *Electron Efficiency Correlation Model*. 2021. URL: <https://twiki.cern.ch/twiki/bin/view/AtlasProtected/ElectronEfficiencyCorrelationModel>.
- [16] ATLAS Internal. *Jet Vertex Tagger for Run 2 in reco and analysis*. 2021. URL: <https://twiki.cern.ch/twiki/bin/view/AtlasProtected/JetVertexTaggerTool>.
- [17] ATLAS Internal. *Muon Efficiencies for Analyses*. 2021. URL: <https://twiki.cern.ch/twiki/bin/view/AtlasProtected/MuonEfficienciesForAnalysis>.
- [18] G. Avoni et al. “The new LUCID-2 detector for luminosity measurement and monitoring in ATLAS”. In: *JINST* 13.07 (2018), P07017. DOI: 10.1088/1748-0221/13/07/P07017.
- [19] Olga Bessidskaia Bylund. *Measurement of ttZ and ttW production at ATLAS in 13 TeV data, using trilepton and same charge dimuon final states*. Tech. rep. Geneva: CERN, Aug. 2016. DOI: 10.22323/1.276.0237. URL: <http://cds.cern.ch/record/2211022>.
- [20] Oliver Sim Brüning et al. *LHC Design Report*. CERN Yellow Reports: Monographs. Geneva: CERN, 2004. DOI: 10.5170/CERN-2004-003-V-1. URL: <https://cds.cern.ch/record/782076>.
- [21] Thomas Calvet. *Automatic binning implementation in TTHFitter - Htop(bb)*. URL: [https://indico.cern.ch/event/455289/contributions/1953694/attachments/1209081/1762963/Calvet\\_binning\\_Htop-160108.pdf](https://indico.cern.ch/event/455289/contributions/1953694/attachments/1209081/1762963/Calvet_binning_Htop-160108.pdf).
- [22] CERN Twiki - TOP WG Summary Plots. URL: <https://twiki.cern.ch/twiki/bin/view/LHCPhysics/LHCTopWGSummaryPlots>.
- [23] CERN Yellow Reports: Monographs. *CERN Yellow Reports: Monographs, Vol. 10 (2020): High-Luminosity Large Hadron Collider (HL-LHC): Technical design report*. en. 2020. DOI: 10.23731/CYRM-2020-0010. URL: <https://e-publishing.cern.ch/index.php/CYRM/issue/view/127>.
- [24] Shion Chen. *Track isolation variable for the PFlow WPs*. Oct. 2019. URL: [https://indico.cern.ch/event/854783/contributions/3595529/attachments/1926980/3190772/IFF\\_20191003\\_PflowWPs.pdf](https://indico.cern.ch/event/854783/contributions/3595529/attachments/1926980/3190772/IFF_20191003_PflowWPs.pdf).
- [25] CMS Collaboration. *Measurements of pp → ZZ production cross sections and constraints on anomalous triple gauge couplings at  $\sqrt{s} = 13$  TeV*. 2020. arXiv: {2009.01186} (hep-ex).
- [26] The ATLAS Collaboration et al. “The ATLAS Experiment at the CERN Large Hadron Collider”. In: *Journal of Instrumentation* 3.08 (Aug. 2008), S08003–S08003. DOI: 10.1088/1748-0221/3/08/s08003. URL: <https://doi.org/10.1088/1748-0221/3/08/s08003>.
- [27] Federico Demartin et al. “tWH associated production at the LHC”. In: *Eur. Phys. J. C* 77.1 (2017), p. 34. DOI: 10.1140/epjc/s10052-017-4601-7. arXiv: 1607.05862 [hep-ph].
- [28] *Electron identification efficiency in data for electrons with  $E_T > 30\text{GeV}$* . URL: [https://atlas.web.cern.ch/Atlas/GROUPS/PHYSICS/PAPERS/EGAM-2018-01/fig\\_16.png](https://atlas.web.cern.ch/Atlas/GROUPS/PHYSICS/PAPERS/EGAM-2018-01/fig_16.png).
- [29] F. Englert and R. Brout. “Broken Symmetry and the Mass of Gauge Vector Mesons”. In: *Phys. Rev. Lett.* 13 (9 Aug. 1964), pp. 321–323. DOI: 10.1103/PhysRevLett.13.321. URL: <https://link.aps.org/doi/10.1103/PhysRevLett.13.321>.
- [30] *Errors in weighted histograms*. URL: <https://www.zeuthen.desy.de/~wischnew/amanda/discussion/wgterror/working.html>.
- [31] Guido Fantini et al. *The formalism of neutrino oscillations: an introduction*. 2020. arXiv: 1802.05781 [hep-ph].
- [32] Steve Farrell. *Overlap Removal Tools, FTAG/Hbb Workshop*. URL: [https://indico.cern.ch/event/631313/contributions/2683959/attachments/1518878/2373377/Farrell\\_ORTools\\_ftaghbb.pdf](https://indico.cern.ch/event/631313/contributions/2683959/attachments/1518878/2373377/Farrell_ORTools_ftaghbb.pdf).
- [33] *GoodRunListsForAnalysisRun2*. URL: <https://twiki.cern.ch/twiki/bin/viewauth/AtlasProtected/GoodRunListsForAnalysisRun2>.
- [34] Particle Data Group et al. “Review of Particle Physics”. In: *Progress of Theoretical and Experimental Physics* 2020.8 (Aug. 2020). 083C01. ISSN: 2050-3911. DOI: 10.1093/ptep/ptaa104. eprint: <https://academic.oup.com/ptep/article-pdf/2020/8/083C01/33653179/ptaa104.pdf>. URL: <https://doi.org/10.1093/ptep/ptaa104>.
- [35] Peter W. Higgs. “Broken Symmetries and the Masses of Gauge Bosons”. In: *Phys. Rev. Lett.* 13 (1964). Ed. by J. C. Taylor, pp. 508–509. DOI: 10.1103/PhysRevLett.13.508.

- [36] Peter W. Higgs. “Spontaneous Symmetry Breakdown without Massless Bosons”. In: *Phys. Rev.* 145 (1966), pp. 1156–1163. DOI: 10.1103/PhysRev.145.1156.
- [37] *IFFTruthClassifier GitLab Repository*. URL: <https://gitlab.cern.ch/ATLAS-IFF/IFFTruthClassifier/-/tree/master>.
- [38] *IFFTruthClassifier Lepton Categories*. URL: <https://gitlab.cern.ch/ATLAS-IFF/IFFTruthClassifier/-/tree/master#3-details-about-the-lepton-categories>.
- [39] F. Jegerlehner. “The hierarchy problem of the electroweak Standard Model revisited”. In: (May 2013).
- [40] V. Khachatryan et al. “Measurement of the ZZ production cross section and  $Z \rightarrow \ell^+\ell^-\ell^+\ell^-$  branching fraction in pp collisions at  $\sqrt{s} = 13\text{TeV}$ ”. In: *Physics Letters B* 763 (2016), pp. 280–303. ISSN: 0370-2693. DOI: <https://doi.org/10.1016/j.physletb.2016.10.054>. URL: <https://www.sciencedirect.com/science/article/pii/S0370269316306256>.
- [41] Luigi Marchese. *Lepton and photon reconstruction and identification performance in ATLAS and CMS*. Tech. rep. Geneva: CERN, Sept. 2019. DOI: 10.22323/1.350.0237. URL: <https://cds.cern.ch/record/2688452>.
- [42] Thomas McCarthy. *Macro developed to compare t/W/Z reconstruction performance (2 $\ell$ , 3 $\ell$ , 4 $\ell$ )*. URL: [https://indico.cern.ch/event/986357/contributions/4172907/attachments/2169451/3666801/reco\\_performance\\_macro\\_20210112.pdf](https://indico.cern.ch/event/986357/contributions/4172907/attachments/2169451/3666801/reco_performance_macro_20210112.pdf).
- [43] Thomas McCarthy and Florian Fischer. *Exploiting full/partial  $t\bar{t}$  reconstruction for background suppression in 2 $\ell$* . URL: [https://indico.cern.ch/event/955360/contributions/4016465/attachments/2102418/3534816/top\\_reco\\_bkgd\\_suppression\\_2L\\_20200915.pdf](https://indico.cern.ch/event/955360/contributions/4016465/attachments/2102418/3534816/top_reco_bkgd_suppression_2L_20200915.pdf).
- [44] *MCTruthClassifier - ATLAS Twiki*. URL: <https://twiki.cern.ch/twiki/bin/view/AtlasProtected/MCTruthClassifier>.
- [45] Users MissMJ and Cush. *Standard model of elementary particles - Wikimedia Commons*. URL: [https://en.wikipedia.org/wiki/File:Standard\\_Model\\_of\\_Elementary\\_Particles.svg](https://en.wikipedia.org/wiki/File:Standard_Model_of_Elementary_Particles.svg).
- [46] Monte Carlo to Monte Carlo scale factors for flavour tagging efficiency calibration. Tech. rep. ATL-PHYS-PUB-2020-009. Geneva: CERN, May 2020. URL: <https://cds.cern.ch/record/2718610>.
- [47] *MuonSelectionTool, ATLAS TWiki*. URL: <https://twiki.cern.ch/twiki/bin/view/Atlas/MuonSelectionTool>.
- [48] O Oncel. *Search for Single Top Quark Production in Association with a W and a Z Boson in the 3 Lepton Final State with the ATLAS Experiment at 13 TeV*. URL: <https://cds.cern.ch/record/2625170>.
- [49] *Option to force a shape withing an error band by hand - TRF documentation*. URL: [https://trexfitter-docs.web.cern.ch/trexfitter-docs/model\\_building/shape/](https://trexfitter-docs.web.cern.ch/trexfitter-docs/model_building/shape/).
- [50] *Pileup jet recommendations*. URL: <https://twiki.cern.ch/twiki/bin/view/AtlasProtected/PileupJetRecommendations>.
- [51] *Recommended isolation working points*. URL: <https://twiki.cern.ch/twiki/bin/view/AtlasProtected/RecommendedIsolationWPs>.
- [52] *Scikit-Learn GradientBoostingClassifier Documentation*. URL: <https://scikit-learn.org/stable/modules/generated/sklearn.ensemble.GradientBoostingClassifier.html>.
- [53] *TopRecoObjTwikiModel*. URL: <https://twiki.cern.ch/twiki/bin/view/AtlasProtected/TopRecoObjTwikiModel>.
- [54] *TRExFitter*. URL: <https://twiki.cern.ch/twiki/bin/viewauth/AtlasProtected/TtHFitter>.
- [55] *TRExFitter: Mixed data and MC fit*. URL: <https://trexfitter-docs.web.cern.ch/trexfitter-docs/AdvancedTutorial2020/Mixed/>.
- [56] Benjamin Warren. “A search for tWZ production in the trilepton channel using Run 2 data from the ATLAS experiment.” In: (2021).
- [57] Kenneth G. Wilson. “Confinement of quarks”. In: *Phys. Rev. D* 10 (8 Oct. 1974), pp. 2445–2459. DOI: 10.1103/PhysRevD.10.2445. URL: <https://link.aps.org/doi/10.1103/PhysRevD.10.2445>.